# Robust Steering Vector Mismatch Techniques for Reduced Rank Adaptive Array Signal Processing

Hien N. Nguyen

Dissertation submitted to the Faculty of the
Virginia Polytechnic Institute and State University
in partial fulfillment of the requirements for the degree of

Doctor of Philosophy
in
Electrical and Computer Engineering

Timothy Pratt, Chair
Scott Goldstein
Joseph R. Guerci
Jeremy Allnutt
Daniel J. Schaefer
Luiz Da Silva
Terry Herdman

Oct 10, 2002
Fallschurch, Virginia

Keywords: STAP, reduced rank, steering vector mismatch, multistage Wiener filter, radar

# Robust Steering Vector Mismatch Techniques for Reduced Rank Adaptive Array Signal Processing

Hien N. Nguyen

(ABSTRACT)

The research presented in this dissertation is on the development of advanced reduced rank adaptive signal processing for airborne radar space-time adaptive processing (STAP) and steering vector mismatch robustness. This is an important area of research in the field of airborne radar signal processing since practical STAP algorithms should be robust against various kinds of mismatch errors. The clutter return in an airborne radar has widely spread Doppler frequencies; therefore STAP, a two-dimensional adaptive filtering algorithm is required for effective clutter and jamming cancellation. Real-world effects in nonhomogeneous environments increase the number of adaptive degrees of freedom required to adequately suppress interference. The increasing computational complexity and the need to estimate the interference from a limited sample support make full rank STAP impractical. The research presented here shows that the reduced rank multistage Wiener filter (MWF) provides significant subspace compression better than any previous techniques in a nonhomogeneous environment. In addition, the impact of steering vector mismatch will also be examined on the MWF. In an airborne radar environment, it is well known that calibration errors and steering vector mismatch can seriously degrade adaptive array performance and result in signal cancellation. These errors can be caused by many non-ideal factors such as beam steering angle errors, multipath propagation, and phase errors due to array imperfections. Since the MWF centrally features the steering vector on its formulation, it is important to assess the impact of steering vector mismatch. In this dissertation, several novel techniques for increasing robustness are examined and applied to the MWF. These include derivative constraints, quiescent pattern control

(QPC) techniques, and covariance matrix tapers (CMT). This research illustrates that a combination of CMT and QPC, denoted CMTQ, is very effective at mitigating the impact of steering vector mismatch. Use of CMTQ augmentation provides the steering vector mismatch robustness that we desire while improving the reduced-rank and reduced sample characteristics of the MWF. Results using Monte Carlo simulations and experimental Multichannel Airborne Radar Measurements (MCARM) data confirm that the use of CMTQ gives superior performance to steering vector errors at a much reduced rank and sample support as compared to conventional techniques.

# Acknowledgements

I would like to convey my heartfelt thanks to my primary advisors, with whom I was most priviledged to work. First, I express gratitude to Dr. Timothy Pratt, for providing much invaluable technical support and advice. I also deeply appreciate the time and effort he spent to help me improve my research and writing abilities to complete this research project. Next, I thank my co-advisor Dr. J. Scott Goldstein for allowing me to pursue my research and giving me technical guidence. Dr. Goldstein is also co-inventor of the multistage Wiener filter on which much of this research is based. I am also indebted to Dr. Joseph Guerci for providing valuable advice and explaining all intricate details about the concept of covariance matrix tapers. Dr. Guerci is also co-inventor of covariance matrix tapers for which this research is mostly focused. Next, I deeply appreciate Dr. Jeremy Allnutt of George Mason University for giving me technical insight and guidance during my research process. I also thank the other members of my dissertation committee, Dr. Daniel Schaefer, Dr. Luiz Da Silva, and Dr. Terry Herdman, for insightful comments and their effort in reviewing this dissertation.

I wish to thank my parents who have always guided me in my educational pursuits. I am also grateful to my wife, Loan Nguyen and my son, Justin Nguyen for their support, patience and encouragement.

# Table of Contents

# List of Tables

# List of Figures

# List of Acronyms and Abbreviations

| | |
|---|---|
| CMT | Covariance Matrix Tapers |
| CPI | Coherent Processing Interval |
| CFAR | Constant False Alarm Rate detection test |
| CSA | Correlation Substraction Architecture |
| CSP | Cross-Spectral Metric |
| DOF | Degrees of freedom |
| ESA | Electronically scanned arrays |
| Full-rank | Full rank MVDR |
| GSC | Generalized Sidelobe Canceller |
| ICM | Internal clutter motion |
| ICV | Internal clutter velocity |
| i.i.d | Independent and identical distributed |
| LCMV | Linear constrained minimum variance beamforming |
| LFM | Linear frequency modulation |
| QPC | Quiescent pattern control |
| JNR | Jammer-to-noise ratio |
| MCARM | Multichannel Airborne Radar Measurements Program |
| MOP | Measure of CFAR performance (target /RMS of noise samples) |
| MVDR | Minimum Variance Distortionless Response |

| | |
|---|---|
| MWF | Multistage Wiener Filter |
| MWF-sc (sc) | Multistage Wiener Filter with standard single constraint |
| MWF-cmtq (cmtq) | MWF with combination of CMT and QPC |
| MWF-der2 (der2) | MWF with 0-plus-1st-plus-2nd derivative constraints |
| MTI | Moving Target Indicator |
| $N_{dof}$ | Number of degrees of freedom |
| MMSE | Minimum mean square error |
| MSE deviation $\epsilon$ | QPC mean square error deviation |
| Penalty funct. order $p$ | QPC Penalty function 's charateristic order |
| PRI | Pulse Repetiton Interval |
| PRF | Pulse Repetiton Frequency |
| RCS | Radar cross section |
| RMS | Root mean square |
| ROC | Region of convergence for adaptivity |
| SINR | Output signal-to-interference plus noise ratio |
| $\text{SINR}_{loss}$ | Output SINR relative to the SNR in white noise |
| SMI | Sample Matrix Inversion |
| SNR | Output signal-to-noise ratio |
| STAP | Space-Time Adaptive Processing |
| ULA | Uniform linear array |
| UESA | UHF Electronically Scanned Array |
| WNC | White Noise Constraints |
| Widening Factor $\gamma$ | CMT fraction of beamspace widening |
| w.s.s | Wide sense stationary |
| 1-D | One-dimensional (spatial-only) adaptive processing |
| 2-D | Two-dimensional (space-time) adaptive processing |

# Chapter 1

# Introduction

Airborne early warning (AEW) radar is very useful for the detection of small radar cross-section (RCS) targets in severe clutter. Unlike a ground-based radar, in which nearly all the clutter return is received at zero-Doppler frequency, the clutter return in an airborne radar has widely spread Doppler frequencies due to the movement of the platform. The clutter energy exhibits a complex two-dimensional (2-D) spatial-temporal dependency in both Doppler frequency and angle as observed in Figure 1.1. The 2-D extent of the clutter means that the mainbeam target competes with mainlobe clutter in the angle domain and in the sidelobe clutter in the Doppler frequency domain. A conventional airborne moving target indication (MTI) radar is thus unable to cancel clutter without suppressing the desired targets because it uses temporal degrees of freedom only. The precise nature, the location of clutter interference and jamming in the AEW radar environment are not known a priori, and therefore space-time adaptive processing (STAP) is required for effective interference and clutter cancellation.

The availability of ever-improving phased-array antennas and advanced digital

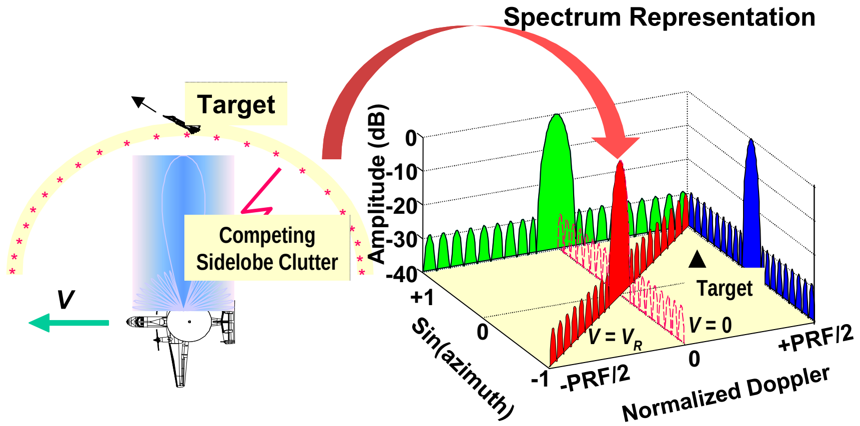

Figure 1.1: AEW Radar Interference Environment and Spectrum Representation; $\mathbf{v}$ is platform speed; PRF is radar pulse repetition frequency; Doppler frequency is normalized to PRF; The mainbeam points at the target located in clutter sidelobe; When platform is stationary ($\mathbf{v}$ =0), clutter depends on azimuth angle only; When platform is moving ($\mathbf{v} = \mathbf{v}_r$), clutter depends on both azimuth angle and Doppler frequency

signal processing technology has renewed interest in STAP since the late 1980's. An airborne radar employs phased array antennas to generate the spatial degrees of freedom as required by a STAP processor. Phased array antennas are also employed for better control of sidelobe and the ability to steer nulls in the jammer directions. A STAP processor is formed by placing a tapped delay line at the output of each antenna of the array, with the taps spaced by one pulse repetition interval (PRI). The total degrees of freedom of a STAP processor constitute the number of antenna elements times the number of PRI taps (i.e. pulses). As the target becomes smaller and the noise becomes more challenging, the resolution requirements to separate target from clutter result in a larger number of degrees of freedom and sample support.

The recently developed reduced-rank multistage Wiener filter (MWF) technique was shown more robust to rank and sample support requirements as compared to prior STAP techniques [23], [24], [25], [31], [49]. Full-rank STAP techniques are optimum when the data is stationary and the covariance matrix is either known or there is sufficient sample support to estimate it accordingly. [52]. Reduced-rank STAP techniques directly reduce the number of dominant statistical unknowns associated with the interference, and promise near-optimum clutter suppression while minimizing the sample support requirements and computational complexity that are required with full-rank methods. In general, the rank of the noise and clutter is the number of degrees of freedom that the noise and clutter occupy in the signal subspace. Reduced rank techniques provide enormous potential benefits since the rank also dictates the required sample support.

The MWF centrally features the steering vector in its formulation, therefore it is important to assess the impact of steering vector mismatch. The steering vector is the expected target response in a direction of interest. Steering vector mismatch errors can be caused by many non-ideal factors such as beam steering angle errors, multipath propagation, and phase errors due to array imperfections and array calibration errors. In practice, an array calibration procedure is mandatory because it is very difficult to determine the steering vector based on theoretical considerations. Typically, this involves placing an emitter at a known direction and measuring the array response to this signal. This calibration process produces a complex array manifold that is composed of steering vectors from all possible azimuth angles. Because the array response is dependent on many variables, and because of calibration errors, it is likely that there will be some error in the measured steering vector. Due to this mismatch, the presumed steering vector, used as a reference for the target in the adaptive weight computation, may not equal the *true* target response, and the desired signal can be inadvertently suppressed. As a result, practical STAP performance may suffer significant performance degradation when there exists mismatch errors.

The research reported in this dissertation examines novel constraint implementations in the MWF structure to robustly adapt to steering vector mismatch errors in nonhomogeneous environments. In practice, real-world effects such as internal clutter motion, aircraft crabbing due to wind drift, diffuse multipath and terrain nonhomogeneity can greatly induce nonhomogeneity in the underlying statistics of the data. These artifacts increase the rank and number of adaptive degrees of freedom (DOF) required to adequately suppress clutter and interference. In these environments, the steering vector mismatch problem may be pronounced and is another critical issue that needs to be examined in the MWF structure. Furthermore, since the MWF converges to the optimum STAP solution [7], steering vector errors are also expected to lead to signal cancellation. All these issues are associated with the MWF approach and have not been addressed or published in the current literature. A new implementation is proposed to provide the steering vector mismatch robustness that we desire while improving the reduced-rank and reduced sample characteristics of the MWF.

## 1.1 Adaptive Processing for Airborne Radar

Adaptive array processing [10], [47] techniques developed over the last 20 years have been successfully used to mitigate the effects of jamming on communication and radar systems. These adaptive techniques can provide nulling far below the sidelobe level limitation due to random errors.

An airborne radar employs a phased array with several output channels to provide a spatial processing dimension. The phased-array radar is used to detect or enhance the target echo, while simultaneously reducing and nulling unwanted interference such as jamming and clutter. Figure 1.2 displays a simple representation for a uniform linear phased array and Figure 1.3 represents an adaptive narrowband beamformer model that combines the output from the individual sensor elements. Conventional antennas produce a mainbeam in a certain direction by physically rotating the antenna. Modern phased arrays delay the outputs from the individual elements electrically and form a beam in a certain direction to search for targets. In a beamformer, a spatial filtering operation is performed by linearly summing and weighting the data observed at multiple sensors so that the desired signal combines coherently while the undesired noise and interference combines incoherently. The optimum weight is usually selected by either maximizing the array output SINR or minimizing the array output variance.

The availability of ever-improving phased-array antennas and advanced digital signal processing technology has renewed an interest in STAP since the late 1980's. In traditional phased-array beamforming, the signals gathered by the array are shifted in phase, summed in an analog device, down-converted to proper frequency bands, and successively transformed into digital words. The disadvantages of analog phased arrays are related to the difficult control of sidelobe levels, high loss, complex construction, and absence of individual beam control. A digital beamformer can eliminate these problems and is shown in Figure 1.4, which accepts the digital signals from an antenna array. As shown, signals at sensors are converted to complex digital

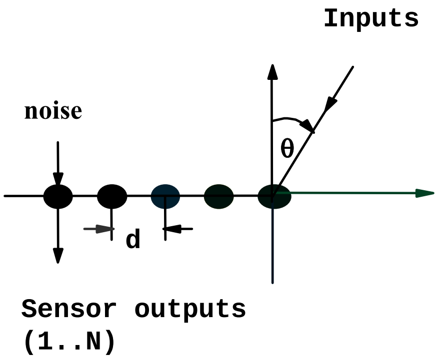

Figure 1.2: Uniform Linear Geometry of an Antenna Phased Array; $N$ is number of sensor elements; $\theta$ is signal arrival angle measured from the array boresight

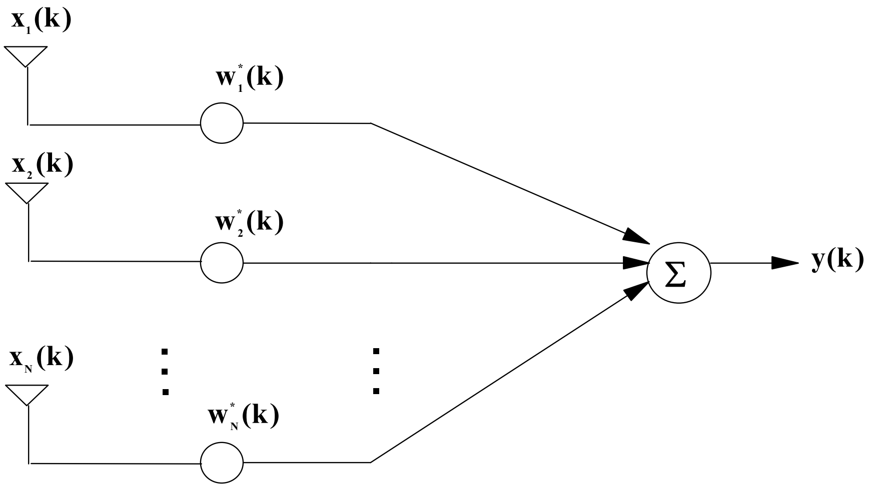

Figure 1.3: Adaptive Beamformer Structure; $\mathbf{x}$ denotes array input; $y$ is the beamformer output; and $\mathbf{w}$ is adaptive weight

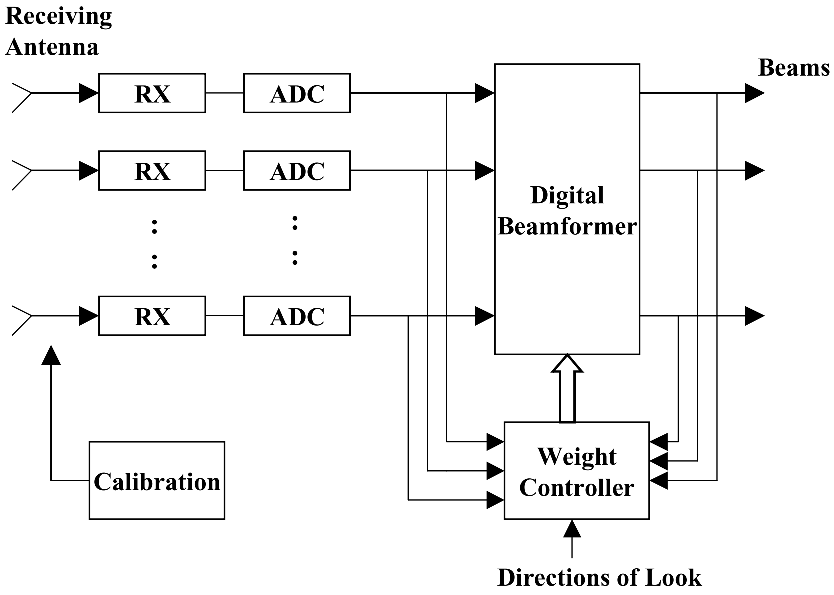

Figure 1.4: Basic Scheme of a Digital Beamformer; Rx = receiver; ADC = analog to digital converters; Signals at elements are converted to complex digital numbers at MegaHertz rate, then transfered to a high speed digital processor, and create a set of beams differently oriented in space

numbers at MegaHertz rate by the analog to digital converters, then transferred to a high speed digital processor. A calibration unit is also shown and is mandatory to guarantee the matching of the receiving channels. The element weights are generated by a separate controller and the output is a set of beams that can be scanned in space.

Using a phased array, a STAP processor can be formed by placing a tapped delay line at the output of each antenna of the array, with the taps spaced by one pulse repetition interval (PRI). A general STAP processor model is displayed in Figure 1.5. The data are assumed to be comprised of the down-converted and digitized I-Q samples as required for a narrowband model. The total degrees of freedom constitute the number of antenna elements times the number of PRI taps

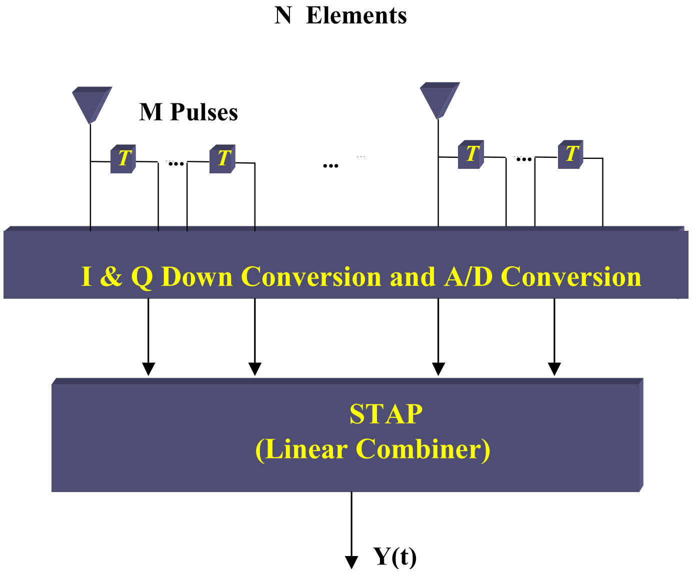

Figure 1.5: A General STAP Processor; $N$ is number of elements; $M$ is number of pulses; Each antenna element has its own down-converter, matched filter (not shown) and A/D converter

(i.e. pulses). The improvements in measured signal-to-interference plus noise (SINR) is proportional to this number. However, as the target becomes smaller and the noise becomes more challenging, this number grows, requiring larger sample support and more computational complexity.

The first published work on space-time adaptive processing (STAP) for radar was Brennan and Reed [7], from 1973, in which optimum space-time filtering was described. These full-rank STAP methods may be problematic if the data is non-stationary / non-homogeneous or when computational resources are limited. Future airborne surveillance drives the requirement for larger numbers of degrees of freedom, which also drives the need for larger numbers of homogeneous samples. In general, the number of required samples is at least on the order of twice the number of the radar's degrees of freedom [52] to fulfill the above assumptions. Therefore, it may be impossible to satisfy these underlying statistical assumptions. Reduced-rank STAP techniques promise near-optimum clutter suppression at reduced sample support and computation, and therefore are of great interest.

Reduced-rank STAP mappings can be non-adaptive or adaptive. Non-adaptive mappings of reduced-rank STAP algorithms consist of a deterministic transformation prior to adaptive processing [69], [43]. These algorithms are sub-optimum and generally ad-hoc techniques, which are designed depending on the specific anticipated operating environments [50]. Adaptive rank reduction techniques use statistical methods to reduce the degrees of freedom prior to adaptive processing. This offers the possibility of achieving or surpassing the same high performance as the full rank techniques while minimizing the sample support and computational burden. The most popular adaptive rank reduction approaches, such as the principal-components (PC) [35] and cross-spectral metric (CSP) [26], [27], utilize a linear eigenvalue analysis-based processor. These algorithms can generally provide excellent performance. However, an eigenvalue decomposition of the interference covariance matrix is required, which is computational intensive for real-world applications. The recently developed multistage Wiener filter (MWF) technique is more robust to rank and sample support requirements, especially in nonhomogeneous environments [23], [24], [25], [31], [49]. Unlike previous rank reduction techniques, the MWF approach does not require the eigenvalue decomposition and achieves a much higher degree of signal subspace compression through basis selection using pertinent information related to the signal of interest.

## 1.2 Overview of Steering Vector Mismatch Techniques

Adaptive algorithms are very effective in suppressing interference, however, they are very sensitive to steering vector mismatch errors. Numerous robust methods have been proposed for broadening the mainbeam of the steering vector while preserving the beamformer's ability to reject unwanted interference.

A simple technique is to impose point, derivative and quadratic constraints directly on the beamformer response. Multi-point linear constraints control the response only at specific points and may require many degrees of freedom [1]. This problem can be resolved by using derivative constraints [5], [15], [18] which controls the mainbeam response over a region and requires many fewer adaptive degrees of freedom. The use of derivative constraints may however cause the resulting array performance to degenerate from its optimum since the degrees of freedom available for searching the optimum vector are reduced under steering vector errors. Its performance is also sensitive to the array spatial reference and degrades seriously when the desired signal is present in the snapshot data. Nevertheless, the use of derivative constraints is the most well-known approach to the steering vector problem, and its implementation in the MWF structure is examined in this dissertation.

Additionally, quadratic constraints [17], [39], [64] have been proposed to minimize the total mean squared error between the desired and actual response over a region of frequencies and azimuths. The use of white noise constraints (WNC) is a variation of quadratic constraints in which a magnitude constraint is imposed on the weight vector norm [14]. WNC improves beamformer robustness to combat adverse effects, such as amplitude and phase errors, but a small norm bound can reduce the ability of the beamformer to suppress directional interference. Both quadratic and white noise constraints generally require an iterative calculation of the covariance matrix, resulting in additional computational burden. Recently, an eigenspace projection (ESP) method has been proposed to constrain the steering vector within the signal-plus-interference subspace for solving the problem of steering vector errors [21]. These approaches require an eigendecomposition of the covariance matrix, which may be suboptimum for a nonhomogeneous environment and the implementation is also generally computational intensive.

## 1.3 Overview of Radar STAP Systems

Several experimental and operational radar systems with multichannel antennas for space-time processing currently exist [43] and have been developed in the last decade. The Multichannel Airborne Radar Measurements Program (MCARM) by Rome Laboratories is the only program to date that distributes data collected by an airborne radar using a relative large number of antenna elements. The research in this dissertation will exploit the MCARM data to evaluate the robustness of the proposed approach. Some of the well-known radar systems are listed below:

1. The Multichannel Airborne Radar Measurements Program (MCARM) by Rome Laboratories used an Westinghouse L-band airborne phased-array testbed with 22 antenna elements. Part of this program was to examine real-time processing architectures and the capabilities of STAP in practical environments [3], [59].

2. Naval Research Laboratory (NRL) used an eight-element UHF linear array under an EP-3A aircraft [44], [50].

3. The MOUNTAINTOP Program used an 14 element array at UHF frequency and special hardware to simulate a flying radar when in fact it was stationary and on the ground [61].

## 1.4 Outline of Dissertation

This dissertation is organized as follows. Chapter 2 considers some fundamentals, including an introduction to adaptive array processing and formulation for optimum adaptive weights. These fundamentals are extended in chapter 3, in which a formulation for fully adaptive space-time processing (full-rank STAP) and issues associated with airborne radar signal environments are described. This chapter also discuss a number of performance measures and Monte Carlo (MC) method to be used in validating the results. Chapter 4 presents a critical need for reduced rank adaptive processing and reviews some popular reduced-rank versions of the Wiener filter, namely principal components (PC) and the cross-spectral (CSP) methods are described. The reduced-rank multistage Wiener filter (MWF) that has been shown to exceed the performance of the full-rank Wiener filter in many applications is introduced. This chapter also presents some numerical results validating its performance as compared to the principal components (PC) and the cross-spectral (CSP) approaches using ideal covariance matrices. Additionally, the region of convergence for adaptivity (ROC) of the MWF as a function of both rank and sample support is evaluated with the PC method in the presence of eigenvalue spreading. In chapter 5, the performance loss under steering vector mismatch errors is analyzed using ideal covariance matrices and a new MWF implementation using derivative constraints is presented. Chapter 6 introduces a novel constraint implementation on the MWF structure, CMTQ, which is based on a combination of covariance matrix taper (CMT) and quiescent pattern control (QPC) for robustness to steering vector mismatch. A new CMT data-domain implementation for use with the MWF structure and an efficient QPC design using a Taylor series approximation are also introduced. Use of CMTQ augmentation provides the steering vector mismatch robustness that we desire while improving the reduced-rank and reduced sample characteristics of the MWF in nonhomogeneous environments. In chapter 7 and chapter 8, extensive results are presented to assess the performance of the new approach, using Monte Carlo simulation and experimental MCARM data. CFAR test statistics will be examined for radar target detection in which the ratio of the beamformer output power over the noise power is estimated for each range sample. Furthermore, the region of convergence for adaptivity (ROC) is examined as a function of both the effective rank and the amount of training data under steering vector errors. The vast improvement of the new approach in both lower sample support and significantly lower rank will be demonstrated under steering vector errors. Next, the effects of mainbeam jamming and computational requirement are described in chapter 9. Finally, the conclusion provides a summary of the results reported in the dissertation and presents some areas for future works.

# Chapter 2

# Fully Adaptive Signal Processing

In this chapter, a background for fully adaptive spatial signal processing is described. Some basic concepts and optimum adaptive weight computation for one-dimensional (1-D) adaptive array signal processing will be presented. The three most popular criteria for determining optimality are maximization of array output signal-to-interference plus noise (SINR), minimum noise variance (MVDR) and minimization of mean-squared error (MSE). The last criteria is equivalent to the classical Wiener filter, which is described in detail.

## 2.1 Basic Model

Array signal processing exploits a distributed array of antenna sensors to perform spatial filtering (i.e. difference in angle of arrival) of the signals in order to extract a desired signal in the presence of noise and interference. An array captures the electromagnetic energy from a source with direction $\theta$. In most cases, the objective is to detect and preserve the desired signal inputs while simultaneously reducing unwanted interference. The major advantage of array signal processing is improvements in measured signal-to-noise ratio (SNR) as compared to that attainable with a single input sensor.

A simple representation for a uniform linear phased array is displayed in Figure 2.1, where $N$ is the number antenna elements and $\theta$ is the signal arrival angle measured from the array boresight. On receive, each element of the array has its own down-converter, matched filter receiver, and A/D converter. In this dissertation, we consider only narrowband arrays in which incident signals are assumed narrow band relative to their carrier frequency, and this is typical for airborne radar applications. The phaseshift at each sensor will then be approximately the same over the bandwidth of the signal, and the signal observed at each sensor can be simply a scaled phase-shifted version of the signal observed at any one sensor. The sensor-observed narrow-band data vector $\mathbf{x}(t)$ under the assumption of far-field plane wave signals in white Gaussian noise can be expressed as

$$\mathbf{x}(t) = \sum_{i=1}^{M} \mathbf{s}(\theta_i)\mathbf{z}_i(t) + \mathbf{n}(t), \tag{2.1}$$

where $M$ indicates the number of signal inputs arriving from angles $\theta_1..\theta_M$; $\theta_i$ is the azimuth angle measured from the array boresight; $\mathbf{z}_i(t)$ refers to the $i^{th}$ input signal waveform ; $\mathbf{s}(\theta_i)$ is a signal steering vector associated with angle $\theta_i$; and $\mathbf{n}(t)$ is a vector of white complex Gaussian noise at $N$ sensor elements.

For a uniform linear array, the relative delay between each pair of adjacent sensors is $\tau(\theta) = \frac{d \sin\theta}{c}$ where $d$ is the sensor separation distance, $c$ is the speed of light and $\theta$ is the desired direction of the mainbeam of the antenna. Assuming that the reference

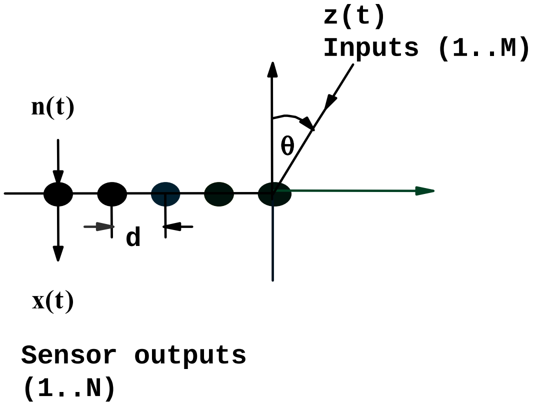

Figure 2.1: Uniform Linear Geometry of an Antenna Phased Array; $n(t)$ is white noise input at each sensor; $N$ is number of sensor elements; $d$ is distance between each element; $\theta$ is signal arrival angle measured from the array boresight

point is located at the first array element, the steering vector can be expressed

$$\begin{aligned} \mathbf{s} &= [1 \;\exp(jw_o\tau)... \;\exp(jw_o(N-1)\tau)]^T && (2.2)\\ &= \left[1 \;\exp(j\frac{2\pi d}{\lambda}\sin\theta)... \;\exp(j\frac{2\pi d}{\lambda}(N-1)\sin\theta)\right]^T, && (2.3)\end{aligned}$$

where $w_o = 2\pi f_{0,}$ and $f_{0,}$ $\lambda$ are the associated carrier frequency and wavelength respectively. Note that the notation "$T$" represents a transposed operation of a vector. Just as in the time domain, to avoid spatial aliasing it is necessary to sample in space at least twice per cycle. Thus to avoid aliasing and grating lobes (increased sidelobes), the sensor separation distance must be $d \leq \lambda/2$ [47]. The array is considered optimum when $d = \lambda/2$ because at that spacing the mainlobe is at its narrowest before the sidelobes start to grow.

A narrowband beamformer model is presented in Figure 2.2, which combines the output from the $N$ sensor elements

$$\mathbf{y}(t) = \mathbf{w}^H \mathbf{x}(t), \tag{2.4}$$

where $\mathbf{y}$ is the beamformer output and $\mathbf{w} = [w_1 ... w_N]^T$ denotes a $N \times 1$ sized vector of beamfoming weights. The notation "$H$" represents the Hermitian operation or conjugate transpose of a vector. The spatial filtering operation is performed by linearly summing and weighting the data observed at multiple sensors so that the desired signal combines coherently while the undesired noise and interference combines incoherently. As a result, the optimum output SNR is higher by a factor $N$ than the input SNR for a single incident signal in white noise, where $N$ is the number of antenna elements (or degrees of freedom) [10]. In conventional (non adaptive) beamforming, the beamforming weight is matched to the desired target steering vector

$$\mathbf{w} = \mathbf{s}. \tag{2.5}$$

The results are optimum in a white noise environment only. When the array is subjected to directional interferences such as jamming or when the measurement noise is correlated between sensors, adaptive beamforming is required.

The three most popular criteria for determining optimality for the adaptive weight are: maximization of array output signal-to-interference plus noise (SINR), minimum noise variance (MVDR) and minimization of mean-squared error (MSE). For typical input conditions, these criteria produce an optimal set of weights identical up to a scale factor.

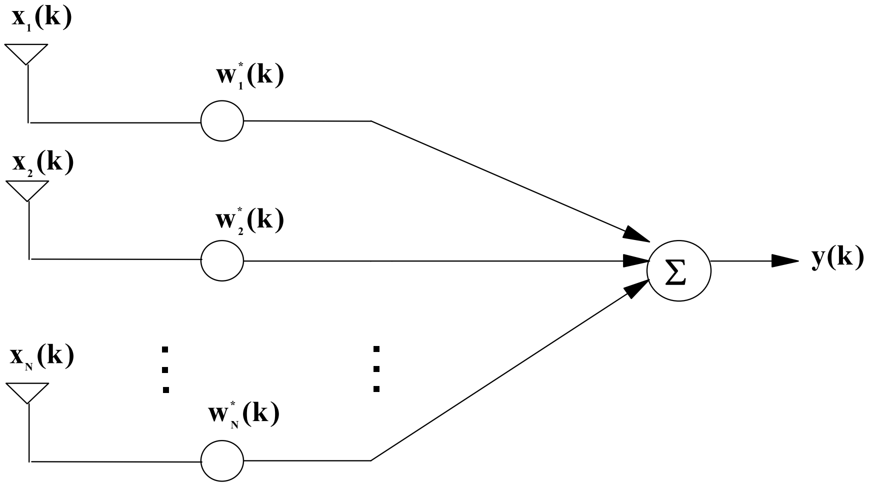

Figure 2.2: Narrow-band Adaptive Beamformer Structure; Signal frequency is narrow band relative to its carrier frequency; **x** denotes array input; $y$ is the beamformer output; **w** is adaptive weight

## 2.2 Optimum Weight

The adaptive weight vector based on maximizing the output SINR is derived by expressing the array output SINR as

$$SINR = \xi \frac{\left|\mathbf{w}^H \mathbf{s}\right|^2}{\mathbf{w}^H \mathbf{R}_i \mathbf{w}}, \tag{2.6}$$

where $\xi = \sigma_s^2/\sigma_o^2$ is the input signal-to-noise (SNR) at each element; $\sigma_s^2$ and $\sigma_o^2$ are the input signal power and noise power variance at each element. In this expression, **s** is the desired target steering vector, and $\mathbf{R}_i$ is a $N \times N$ sized interference-plus-noise covariance matrix that can be structured as

$$\mathbf{R}_i = \sigma_o^2 \mathbf{I} + \sum_{i=1}^{J} p_i \mathbf{s}_i \mathbf{s}_i^H, \tag{2.7}$$

where $\mathbf{I}$ is a $N \times N$ identity matrix, $J$ is the number of jammers, $p_i$ and $\mathbf{s}_i$ are the power and steering vector associated with the $i^{th}$ jammer.

The numerator of (2.6) denotes signal power at the array output and the denominator represents the power contributed to the interference and noise. If it is assumed that $\mathbf{R}_i$ and $\mathbf{s}$ are known, then the optimum weight can be found by maximizing (2.6) with respect to $\mathbf{w}$. Using the Cauchy-Schwartz inequality [47], [33], the optimum weight vector is given by

$$\mathbf{w}_{opt} = \alpha \mathbf{R}_i^{-1} \mathbf{s}, \tag{2.8}$$

where $\mathbf{R}_i$ is assumed known and $\alpha$ denotes a complex constant. The optimum output SINR is obtained when this weight vector is substituted into (2.6)

$$SINR_{opt} = \sigma_s^2 \mathbf{s}^H \mathbf{R}_i^{-1} \mathbf{s}. \tag{2.9}$$

The optimum weight vector (2.8) essentially involves a spatial pre-whitening operation on the interference data in addition to the matched filter operation. The pre-whitening process is performed by inverting the interference covariance matrix ($\mathbf{R}_i^{-1}$), which is used to suppress interference and place nulls in the jammer directions that are not matched to the desired target steering vector. A key parameter of an adaptive beamformer is the number of nulls that can be formed, i.e. the number of jammers that can be nulled. In theory, a beamformer with $N$ sensors can steer $N-1$ nulls. However, as the number of signals increases, it becomes more and more difficult to steer nulls of the depth needed to remove the interference. As a rule of thumb, removing more than $N/2$ interferers will be difficult unless the signals are well separated or the array has an unusually large aperture.

## 2.3 Minimum Noise Variance (MVDR)

The optimum weight vector (2.8) was derived by explicitly maximizing the output SINR, using the assumption that the steering vector and the covariance matrix of the noise and interference are known. In practice, the noise and interference covariance matrix can not be determined from the observed data because the desired signal is also present.

An alternative to explicitly maximizing the output SINR is to minimize the total output noise variance (power) subject to the constraint that the gain in the desired look direction is unity

$$\min_{\mathbf{w}} \mathbf{w}^H \mathbf{R} \mathbf{w} \quad \text{subject to } \mathbf{s}^H \mathbf{w} = 1.$$

This approach yields the minimum variance distortionless response (MVDR) weight vector [47] given by

$$\mathbf{w}_{mvdr} = \frac{\mathbf{R}^{-1}\mathbf{s}}{\mathbf{s}^H \mathbf{R}^{-1}\mathbf{s}} \tag{2.10}$$

where $\mathbf{R} = \mathbf{E}\left\{\mathbf{x}\mathbf{x}^H\right\}$ is the observed data covariance matrix. When $\mathbf{R}$ is known, the MVDR weight vector differs only by a scale factor from the weight derived by maximizing the output SINR, so that the MVDR weight vector is also optimal in the maximum SINR sense.

## 2.4 Minimum Mean Square Error (MMSE): The Wiener Filter

The optimum weight can also be estimated to minimize the array output mean square error (MSE) as shown in Figure 2.3, which describes a classical Wiener filter. The scalar process $d_0$ represents the "desired" signal that is usually the output of a conventional beamformer and the process $\mathbf{x}_0$ is the observed data vector consisting of data different from the desired signal that is received at a sensor array. The goal is to estimate $d_o$ from $\mathbf{x}_0$ and the Wiener filter weight $\mathbf{w}_r$ is optimized for a minimum mean square error (MMSE) between $d_o$ and its estimate $\widehat{d_o}$.

For radar applications, the Wiener filter can be used to remove clutter and jamming by canceling the correlated interference arriving though the sidelobes of the desired process $d_0$ . This process could be the desired target response from the main beam along with any noise and interference in the direction defined by the mainbeam steering vector $\mathbf{s}$. The corresponding "mainbeam" response is defined as $d_o = \mathbf{s}^H\mathbf{x}$, where $\mathbf{x}$ is the sensor-observed data matrix. Due to the presence of correlated interference (non "white") of clutter and jamming in the upper branch, additional whitening filtering is needed. This is accomplished with the lower branch which requires an observed data process $\mathbf{x}_0$ and generally consists of signals from all directions other than the mainbeam. The observed data matrix can be defined as $\mathbf{x}_o = \mathbf{B}\mathbf{x}$, where the standard blocking matrix $\mathbf{B}$ prevents any signal coming from the desired direction($\mathbf{s}$) and thus retains only the interference contribution. The lower branch provides an estimate of the correlated interference $\widehat{d_o}$ which is then subtracted from $d_o$.

The resulting output is the difference between the signal from the desired mainbeam and portion of the sidelobe interference that is correlated with the mainbeam signal. Ideally, the problem is then reduced to a standard case of detecting a target in uncorrelated noise. The output mean square error (MSE) is defined as

$$MSE = E\left\{\left|d_o - \mathbf{w}_r^H\mathbf{x}_o\right|^2\right\} = \sigma_d^2 - \mathbf{w}^H\mathbf{r}_{\mathbf{x}_o d_o} - \mathbf{r}_{\mathbf{x}_o d_o}^H\mathbf{w} + \mathbf{w}^H\mathbf{R}_{x_o x_o}\mathbf{w}, \tag{2.11}$$

where the desired signal power $\sigma_d^2 = E(|d_o|^2)$ and $\mathbf{R}_{x_o} = E\left[\mathbf{x}_o\mathbf{x}_o^H\right]$ is the covariance

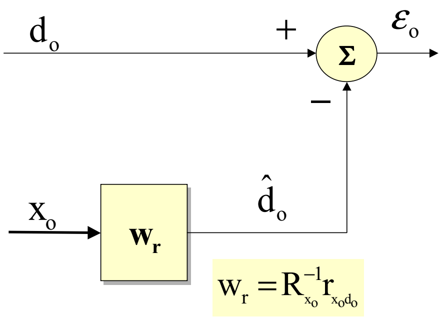

Figure 2.3: Classical Wiener Filter; $d_0$ = desired signal; $\mathbf{x}_0$ = observed data vector; $\mathbf{w}_r$ = Wiener filter weight vector; $\widehat{d}_0$ = estimate of desired signal; $\varepsilon_0$ = error signal

estimate of process $\mathbf{x}_o$. Note that $\mathbf{r}_{x_o d_o} = E\left[\mathbf{x}_o d_o^*\right]$ is the cross-correlation between the processes $d_o$ and $\mathbf{x}_o$, where $(.)^*$ is the complex conjugate operator. The well-known solution to (2.11) is the Wiener filter

$$\mathbf{w}_r = \mathbf{R}_{x_o}^{-1} \mathbf{r}_{x_o d_o}, \tag{2.12}$$

where the indicated matrix inversions are assumed to exist. The MMSE is computed by substituting (2.12) into the expression of the mean square value of error (2.11)

$$\xi_o = \sigma_d^2 - \mathbf{r}_{x_o d_o}^H \mathbf{R}_{x_o}^{-1} \mathbf{r}_{x_o d_o}. \tag{2.13}$$

In general, the overall weight vector for radar applications can be expressed in terms of the Wiener filter weight

$$\mathbf{w} = \mathbf{s} - \mathbf{B}^H \mathbf{w}_r, \tag{2.14}$$

where $\mathbf{s}$ is the steering vector and $\mathbf{B}$ is the blocking matrix defined previously as the null-space of the steering vector $\mathbf{s}$ such that $\mathbf{B}\mathbf{s} = 0$. The optimum output SINR can be computed as follows

$$SINR_{opt} = \frac{\left|\mathbf{w}^H \mathbf{s}\right|^2}{\mathbf{w}^H \mathbf{R}_i \mathbf{w}} = \frac{1}{\sigma_d^2 - \mathbf{r}_{x_o d_o}^H \mathbf{R}_{x_o}^{-1} \mathbf{r}_{x_o d_o}} = \frac{1}{\xi_o}, \tag{2.15}$$

where $\mathbf{R}_i$ is the interference data covariance matrix and $\xi_o$ is the MMSE (2.13).

The weight vector (2.14) was also shown equivalent to the MVDR weight (2.10), which minimizes the output variance subject to a unity signal constraint on the steering vector direction [47]. The reduced-rank multistage Wiener filter (MWF) [24] that will be examined in this dissertation is essentially a reduced-rank version of the MVDR or the Wiener filter. The MWF is therefore expected to converge to the MVDR solution as it utilizes more degrees of freedom. Unfortunately, the MVDR approach is known to be hypersensitive to steering vector errors since it is based on a minimization of output power subject to a unity constraint on the desired look direction. Similarly, the Wiener filter weight is based on the assumption that the observed data process does not contain the desired signal. If the signal is however present, then the power minimization process may result in signal cancellation. A small mismatch in the look direction can result in large degradation in performance. A main objective of this dissertation is to design a robust constraint implementation on the MWF to reduce sensitivity due to these steering vector errors.

# Chapter 3

# Fully Adaptive Space-Time Signal Processing (STAP)

The fundamentals of one-dimensional (1-D) adaptive signal processing from the last chapter can be extended to two-dimensional (2-D) space-time adaptive processing (STAP). A STAP processor is defined as a linear combiner that sums the spatial samples from the elements of an antenna array and the temporal samples from the multiple pulses of a coherent waveform. First, fully adaptive STAP is discussed, which refers to a brute force approach whereby the signals at each element and pulse are adaptively weighted. The results require computational complexity and are optimum only when the statistics of the interference are known. Fully adaptive STAP will however serve as a useful performance bound on any suboptimum approaches. Next, concepts of rank and the well-known Brennan's rule in STAP that helps determine the expected rank of an ideal clutter covariance matrix is described in detail. In general, rank can be interpreted as the number of dominant statistical unknowns associated with the clutter statistics and it dictates the required number of degrees of freedom and sample support. The eigenvalue distribution of an interference and noise covariance matrix usually exhibits how much vector space has been occupied by the interference and dominant statistical unknowns. In practice, the effective rank of the clutter covariance matrix is much larger than the expected rank predicted by Brennan's rule. In this chapter, these concepts provide an introduction to the effect of eigenvalue spreading which gives an indication of the increase in the number of interference eigenvalues and the required larger number of degrees of freedom for effective interference cancellation. Finally, a number of performance metrics and simulation results are presented to validate the performance of fully adaptive STAP techniques. The metrics presented here will prove useful in subsequent chapters as well.

## 3.1 Airborne Array Radar Signal Environment

Space-time adaptive-processing (STAP) for airborne radar is the application of adaptive array signal processing during a multiple pulse coherent waveform. The need for STAP arises in MTI radar because the precise structure, the location of clutter interference and jamming are not known a priori. A spectrum representation of an airborne interference environment was given in Figure 1.1, which can be obtained from a two-dimensional spectrum of the clutter statistics. Jamming is usually discrete in space and has a one-dimensional (1-D) spatial dependence while the clutter on the airborne platform exhibits a more complex two-dimensional (2-D) spatial-temporal dependency. The platform motion causes the clutter background to change with time, and any change of the platform velocity results in a change of the Doppler characteristics of the clutter returns. As displayed in the figure, the clutter observed from an airborne radar may arrive from a different azimuth angle than the target, but can be in the same Doppler cell as the target. A conventional airborne radar receiver is thus unable to cancel clutter in all cases without suppressing the desired target.

In this section, a model is presented for the signals received by an airborne pulse-Doppler radar with a multichannel receive antenna array. On receive, each element of the uniform linear array is assumed to have its own down-converter, matched filter receiver (on each pulse), and A/D converter as shown in the STAP processor displayed in Figure 3.1. The array consists of $N$ antenna elements. A tapped delay line is placed at the output of each element of the array, with the taps spaced by one pulse repetition interval ($PRI$). The radar transmits a coherent burst of $M$ pulses at constant pulse repetition frequency (PRF) $f_r = 1/T_r$, where $T_r$ is the PRI. The time interval over which the waveform returns are collected, is commonly referred to as the coherent-processing interval (CPI) and the CPI length is thus $MT_r$. The transmit waveform is again assumed narrowband with a pulse waveform of duration $T_p$ and the matched filter receiver bandwidth $B$ is assumed. The signal's propagation time across the array is small relative to $1/B$, and the signal observed at each sensor can be simply a scaled phase-shifted version of the signal observed. The received signals are assumed to contain a component due to receiver noise and may contain desired targets, jamming and clutter.

For each PRI, $L$ time samples (also called range bins or range cells) are collected to cover the range interval. The received data for one CPI comprises $LMN$ complex baseband samples with $M$ pulses and $N$ channels. This multidimensional data set can be realized by a pictorial representation, which is often referred as a STAP datacube as shown in Figure 3.2. For each $l^{th}$ range bin, the radar observes the environment in

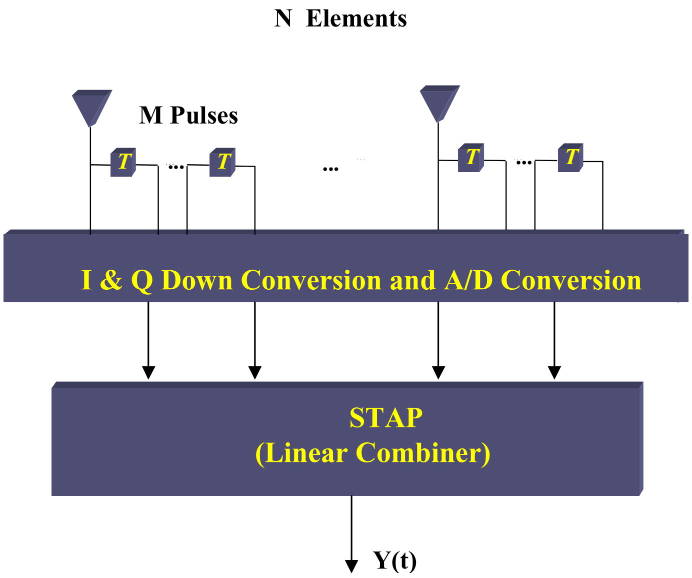

Figure 3.1: A General STAP Processor ($N$ is number of elements; $M$ is number of pulses; Each antenna element has its own down-converter, matched filter (not shown) and A/D converter)

two dimensions consisting of $N$ antenna elements and $M$ pulses. These space-time degrees of freedom provide corresponding "frequency" domains, Doppler frequency and spatial frequency (azimuth angle) respectively. In STAP processing, each of these snapshots is organized into an $(MN \times 1)$ column vector by stacking each $(N \times 1)$ array output data vector concatenated on each of the $M$ pulses.

For a range cell of interest, the received signals can be expressed as

$$\mathbf{x} = \alpha \mathbf{s} + \mathbf{x}_i, \tag{3.1}$$

where $\alpha$ represents a random amplitude, $\mathbf{s}$ denotes the target space-time steering vector and $\mathbf{x}_i$ is the interference. The interference may include clutter, jamming and thermal noise. All these three undesired components are assumed to be mutually uncorrelated.

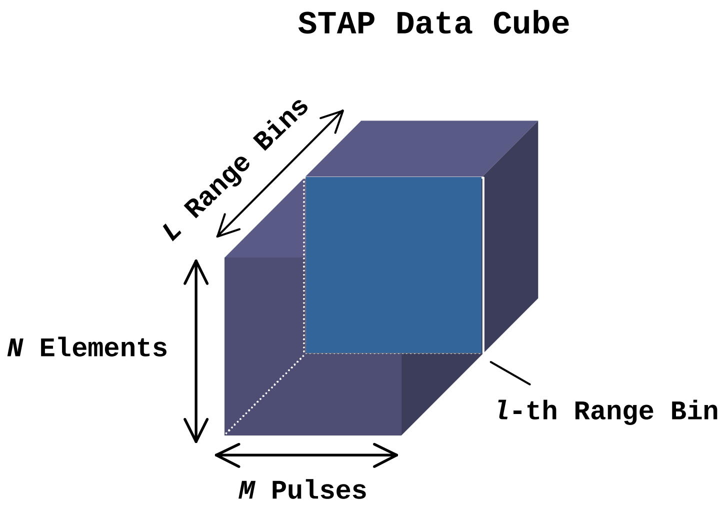

Figure 3.2: STAP Data Cube; Data received during a coherent processing interval (CPI) is represented as a datacube; Its dimensions consisted of $N$ antenna elements, $M$ pulses, and $L$ range bins

### 3.1.1 Target

The target is assumed to be a moving point scatterer that is to be detected. The radar transmits a coherent burst of $M$ pulses and the target echo is received by each of the $N$ elements. As described before, the target signal is modeled as a random amplitude times a space-time steering vector $\mathbf{s}$, that has the target's angle and Doppler.

Unlike the 1-D spatial-only steering vector (2.2), the target steering vector $\mathbf{s}$ depends on both the desired azimuth angle and Doppler frequency shift. The target Doppler frequency shift is due to its relative movement with respect to the radar and can be expressed as

$$f_d = \frac{2v_t}{\lambda_o} \tag{3.2}$$

where $v_t$ denotes its velocity with respect to the radar and $\lambda_o$ is the radar transmit wavelength. It will be convenient to use the normalized Doppler frequency ($\omega$) and azimuth frequency ($\vartheta$) defined respectively as

$$\omega = \frac{f_d}{f_r} \tag{3.3}$$

$$\vartheta = \frac{d}{\lambda_o} \sin\theta \tag{3.4}$$

where $d$ denotes the element spacing, $\theta$ is the azimuth angle from boresight of the array, and $f_r$ represents the radar PRF as described previously. The effect of elevation depression angle has been neglected and this assumption is valid for most target signals received at a far distance from the array.

The spatio-temporal target steering vector $\mathbf{s}$ is an $(MN \times 1)$ column vector given by

$$\mathbf{s} = \mathbf{b}(\omega) \otimes \mathbf{a}(\vartheta) \tag{3.5}$$

where $\mathbf{b}(\omega)$ is a $(M \times 1)$ temporal steering vector

$$\mathbf{b}(\omega) = [1;\ \exp(j2\pi\omega); ...;\ \exp(j2\pi\omega(M-1))] \tag{3.6}$$

and $\mathbf{a}(\vartheta)$ is a $(N \times 1)$ spatial steering vector

$$\mathbf{a}(\vartheta) = [1;\ \exp(j2\pi\vartheta); ...;\ \exp(j2\pi\vartheta(N-1))] \tag{3.7}$$

where "$\otimes$ " represents a Kronecker operation, which is the concatenated products between vector $\mathbf{b}$ and each element of vector $\mathbf{a}$. The space-time steering vector is thus defined to be the response of a target at a normalized azimuth angle $\vartheta$ and Doppler $\omega$.

### 3.1.2 Jamming and Noise

Only barrage noise jamming that originates from land-based or airborne platforms at long range from the radar will be considered. The jamming energy is assumed to extend over the radar's instantaneous bandwidth ($B$ ). This bandwidth is matched to the waveform duration and is usually very large compared to the radar PRF. Conversely, the channel delay time ($1/B$) is much smaller compared to the pulse repetition interval and the jamming is uncorrelated from pulse to pulse. In other words, jamming can be modeled like thermal noise temporally, but it can be represented as a point target in the spatial domain (2.7). The thermal noise is internally generated from the receiver on each channel and the noise processes are assumed uncorrelated on each element and pulse.

### 3.1.3 Clutter

For airborne surveillance radar, the clutter is distributed in both angle and range and the clutter energy is spread over Doppler frequency due to platform motion. A model is presented for the ground clutter component of the space-time snapshot for a given range. The effect of clutter ridges is also described.

#### Generic Clutter Model

An airborne radar receives ground clutter from all azimuth angles and a region in elevation angle bounded by the horizon elevation. The pulse repetition frequency (PRF) is assumed sufficiently low that there are no range ambiguities [58]. In addition, it is assumed that the clutter is stationary and the transmit and receive patterns have a negligible response on the side of the platform opposite to the side where the mainbeam is directed. The return from each discrete ground clutter source has the same form as the target echo defined previously.

For a fixed range, the location of each clutter patch can be described by its azimuth angle $\theta$ and elevation angle $\phi$. Since the ground is stationary, the relative velocity

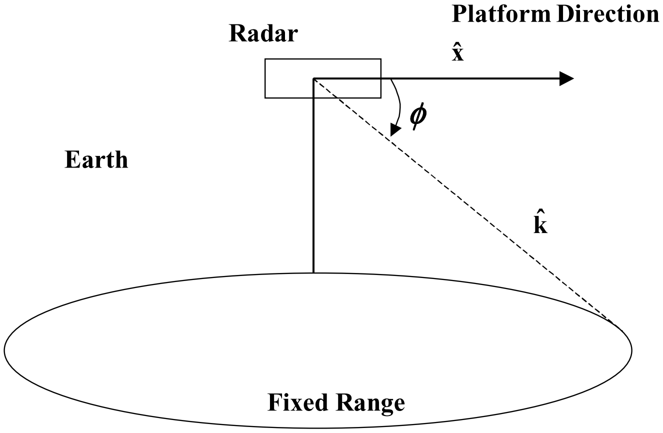

Figure 3.3: A Ring of Ground Clutter for a Fixed Range; $\phi$ is elevation angle for a clutter patch; $\widehat{\mathbf{k}}$ is unit vector pointing from platform to a clutter patch; platform velocity is in the $\widehat{\mathbf{x}}$ direction and aligned with array axis

of a ground clutter source depends only on the platform velocity and its direction with respect to the radar. The array is assumed horizontally oriented ($\widehat{\mathbf{x}}$ direction) and aligned with the the platform velocity vector. If a unit vector $\widehat{\mathbf{k}}$ points from the platform to a clutter patch as shown in Figure 3.3, then the following dot product is observed

$$\widehat{\mathbf{k}} \cdot \widehat{\mathbf{x}} = \cos\phi \sin\theta \tag{3.8}$$

where $\theta$ is the angle measured from the array boresight. The clutter Doppler frequency becomes

$$f_c = \frac{2v}{\lambda_0} \cos\phi \sin\theta$$

where $v$ represents the platform speed and $\lambda_0$ denotes the radar transmit wavelength. It is again convenient to express the normalized Doppler ($\omega_c$) and azimuth frequency

($\vartheta_c$) respectively as

$$\begin{aligned} \omega_c &= \frac{2v}{f_r \lambda_0} \cos\phi \sin\theta \qquad (3.9) \\ \vartheta_c &= \frac{d}{\lambda_o} \cos\phi \sin\theta \qquad (3.10) \end{aligned}$$

where $d$ denotes the element spacing and $f_r$ represents the radar PRF.

As an approximation to a continuous field of clutter, the clutter return from each given range can be modeled approximately as the superposition of a large number of $N_c$ independent and discrete clutter patches evenly distributed in azimuth angle about the radar [69].

$$\mathbf{x}_c = \sum_{i=1}^{N_c} \alpha_i \mathbf{v}_i(\vartheta_i, \omega_i), \qquad (3.11)$$

where $\alpha_i$ is the random amplitude and $\mathbf{v}_i$ is the steering vector for each $i^{th}$clutter patch. The clutter space-time steering vector $\mathbf{v}_i$ has a similar representation as shown in (3.5), which now depends on the normalized Doppler frequency ($\omega_i$) and azimuth angle ($\vartheta_i$) for each $i^{th}$ clutter patch. Assuming that the returns from different clutter patches are uncorrelated, the clutter space-time covariance matrix can be expressed as

$$\mathbf{R}_c = \sum_{i=1}^{Nc} \zeta_i \mathbf{v}_i \mathbf{v}_i^H, \qquad (3.12)$$

where $\zeta_i$ is the power due to the $i^{th}$ clutter patch. In general, the power of each clutter distribution depends on the azimuth angle, spatial distribution, and the range resolution of the radar, and the effective radar cross section (RCS) of the clutter patch. The effective RCS of each clutter patch is proportional to the clutter reflectivity, which varies with the terrain type, radar frequency, polarization, etc. [58]

### Clutter Spectrum

The power spectra of the covariance matrix can be generally found by applying a two-dimensional (2-D) Fourier transform on the clutter covariance matrix, since the array is assumed equispaced and the PRF is constant. The conventional Fourier power estimator may however provide a wrong impression of a two dimensional clutter spectrum since it exhibits sidelobes which have not been included in the clutter model.

A popular high-resolution power estimator such as the Minimum-variance (MV) technique [22] may be used

$$P_{mv} = \frac{1}{\mathbf{s}^H \mathbf{R}_c^{-1} \mathbf{s}} \tag{3.13}$$

where $\mathbf{s}$ is a 2-D clutter steering vector depending on both Doppler frequency and azimuth angle, as described previously, and $\mathbf{R}_c$ is the space-time clutter covariance matrix. This high resolution spectra provides a spectrum that comes closest to the true clutter model, since it eliminates all spurious sidelobes [43].

As an example, a clutter power spectrum for a typical airborne sidelooking radar is shown in Figure 3.4, employing an $N = 14$ element, half-wavelength spaced and $M = 14$ pulse coherent processing interval (CPI). The Minimum-variance (MV) spectrum estimator was applied after having obtained the clutter space-time covariance matrix (3.12). A uniform taper on the transmit pattern is assumed. The clutter was divided among $N_c = 360$ clutter patches equally distributed in azimuth angle about the platform. The elevation angle was assumed zero for simplicity. The array is horizontally oriented and aligned with the velocity vector of the aircraft platform and the clutter-to-noise ratio (CNR) is 60 dB per each element and pulse. The vertical axis denotes clutter Doppler frequency normalized to radar PRF (3.9) and the horizontal axis represents the azimuth angle normalized according to (3.10). The

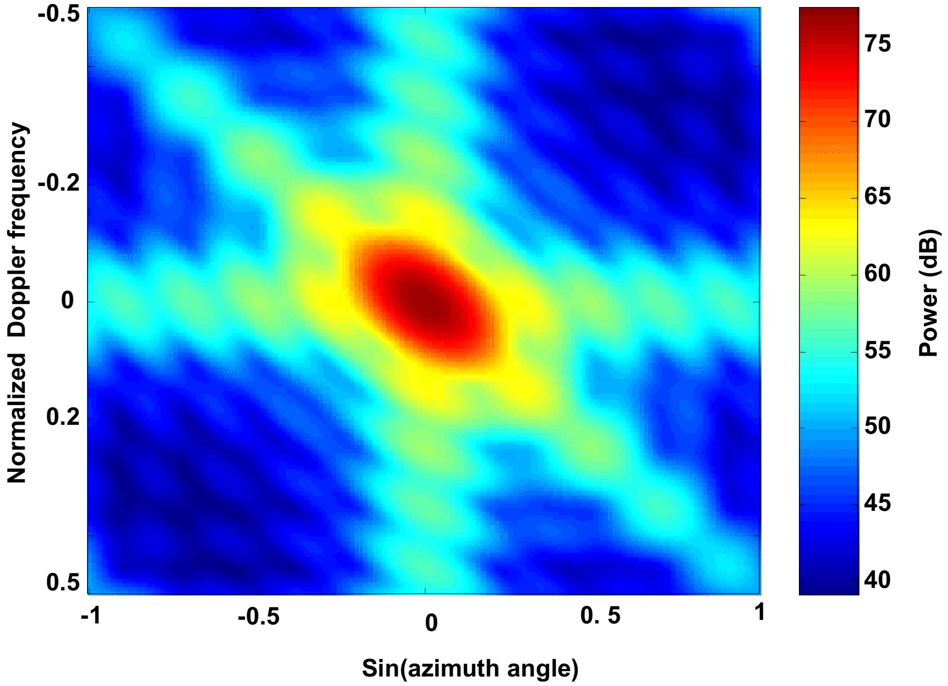

Figure 3.4: Power Spectrum of Clutter: Power vs. normalized Doppler frequency and sin (azimuth angle); Doppler frequency is normalized to PRF; Element spacing, $d = 0.5\lambda$; Number of elements, $N = 14$; Number of pulses, $M = 14$ pulses; Clutter-to-noise ratio, $CNR = 60$ dB; Clutter foldover factor, $\beta = 1$.

radar operates at UHF (450 MHz) with a PRF of 300 Hz, and the environment is assumed to contain clutter and white noise only. In addition, the platform ground speed ($v$), pulse repetition interval ($T_r$), and element spacing ($d$) were set accordingly so that the clutter foldover factor $\beta = 1$, where $\beta$ is defined as the distance traveled by the array during a single pulse repetition interval (PRI) measured in half element spacing units [69]

$$\beta = \frac{vT_r}{d/2}. \tag{3.14}$$

As observed in Figure 3.4, the clutter power energy depends on both azimuth angle and Doppler frequency. Since the delayed tap on each element is a PRI, which can be interpreted as the sampling interval in the time domain, the maximum Doppler frequency normalized to the PRF (in the frequency domain) is 1. The normalized Doppler frequency thus ranges from $-0.5$ to 0.5 after the zero-frequency component is shifted to the center of the spectrum. The maximum clutter energy appears in the transmit direction, which is 0° for a sidelooking radar. This is also referred to as the boresight direction, in which the array response is maximum. As the transmit direction is 90°, the clutter power decays as we expect. This is commonly referred as the endfire direction, in which the array response is minimum. In addition, a large diagonal distribution of energy is observed to extend from the lower right to upper left corner, which is commonly referred to as the "clutter ridge". As we described previously, this Doppler frequency-spread phenomenon is a direct result from platform motion and antenna sidelobes. It varies depending on the platform velocity, pulse repetition frequency, operating wavelength, antenna sidelobes, and backlobes [69].

The clutter ridge is also the locus in angle-Doppler space where the clutter is present. A linear relationship between the normalized Doppler frequency and azimuth frequency can be obtained from (3.9), (3.10), (3.14)

$$\omega_c = \beta \vartheta_c. \tag{3.15}$$

The slope of the clutter ridge is the clutter foldover factor $\beta$, which also describes the amount of clutter Doppler ambiguity or equivalently the number of times the clutter Doppler spectrum aliases into the unambiguous Doppler space [69]. The clutter ridge can span a portion of the Doppler space or the whole Doppler space. It is said to be unambiguous when $\beta \leq 1$, which is as seen in Figure 3.4 for the case of $\beta = 1$. In this case, there is at most one angle where the clutter has the same Doppler frequency as a target. On the other hand, it is ambiguous when $\beta > 1$, in which a series of clutter ridges will be present [69]. The clutter will be more difficult to suppress because a single patch of clutter may have multiple azimuth angles coinciding at a single Doppler frequency. For an airborne radar environment operating at UHF frequency (about 450 MHz), $\beta$ typically ranges from 1 to 2.5. A space-time adaptive processor (STAP) is required to construct a 2-dimensional (2-D) adaptive filter to effectively remove the clutter ridges and whiten the clutter interference.

## 3.2 Fully Adaptive STAP Weight

Fully adaptive space-time processing for airborne radar was first proposed in [7], which is an extension of one-dimensional (1-D) adaptive array processing [47], [10] to a two-dimensional (2-D) space-time problem. The fully adaptive STAP weight computes a separate adaptive weight for every element and pulse.

For a range cell of interest, the $MN \times 1$ space-time received snapshot can be expressed as

$$\mathbf{x} = \alpha \mathbf{s} + \mathbf{x}_i, \tag{3.16}$$

where $\alpha$ represents target amplitude, $\mathbf{s}$ denotes the target steering vector and $\mathbf{x}_i$ is the interference. The $MN \times 1$ space-time steering vector $\mathbf{s}$ forms a beam at angle-Doppler location where target presence or absence is going to be tested. The interference may include clutter, jamming and noise as described in Section 3.1. The STAP weight can be represented by a $MN$-dimensional weight vector $\mathbf{w}$ and the output is denoted

$$y = \mathbf{w}^H \mathbf{x}. \tag{3.17}$$

As similar to the optimum weight for 1-D adaptive signal processing (2.8), the optimum STAP weight that maximizes the array output signal-to-interference plus noise ratio (SINR) is denoted as

$$\mathbf{w}_{opt} = \alpha \mathbf{R}_i^{-1} \mathbf{s}, \tag{3.18}$$

where $\mathbf{R}_i$ is the interference-plus-noise covariance matrix which is assumed known. This weight computation is also commonly called a sample matrix inversion (SMI) [52], since it directly utilizes the inverse of the sample covariance matrix of the training data.

The optimum STAP weight can also be computed using the Wiener filter (2.14)

$$\mathbf{w}_a = \mathbf{s} - \mathbf{B}^H \mathbf{w}_r, \tag{3.19}$$

where the blocking matrix $\mathbf{B}$ is the null-space of vector of $\mathbf{s}$ such that $\mathbf{Bs}$ =0 and the Wiener weight $\mathbf{w}_r$ (2.12) is defined as

$$\mathbf{w}_r = \mathbf{R}_{x_o}^{-1} \mathbf{r}_{x_o d_o}, \tag{3.20}$$

where $\mathbf{R}_{x_o} = \mathbf{B}\mathbf{R}_i\mathbf{B}^H$ and $\mathbf{r}_{x_o d_o} = \mathbf{B}\mathbf{R}_i\mathbf{s}$.

The STAP weight vector provides the optimum solution only when the covariance matrix of the noise and interference is known. In practice, the noise and interference covariance matrix cannot be estimated directly from the data since the desired signal is also present. A training strategy must be implemented in STAP processing to obtain the best estimate for the interference $\mathbf{x}_i$ that exists for each range bin under test. Typically, the data adjacent to the range bin of interest are used and the covariance estimate must contain a sufficient number of samples required for effective clutter cancellation

$$\mathbf{R}_i \simeq E\left[\mathbf{x}_i \mathbf{x}_i^H\right]. \tag{3.21}$$

A conventional adaptive processing chain with target detection is shown in Figure 3.5. When performing target detection in a particular range bin, the range bin under test and several adjacent bins referred to as "guard" cells are excluded from the covariance estimation (3.21) to prevent target leakage and cancellation problems. The training set must be updated for each range bin under test in accordance with the nonstationary nature of the interference and a new weight must be computed for each change in the training set. A target-present or target-absent decision is made for each range Doppler-angle cell by comparing the processor output to a threshold incorporating a constant fall-alarm receiver (CFAR) technique. In general, background noise is adaptively provided to the detector so that it provides constant false alarm rate (CFAR).

A popular adaptive constant false alarm rate (CFAR) detection test, is referred to as the adaptive matched filter (AMF) [54], [12]. The test statistic $\eta(k)$ for each range bin $k$ is computed by normalizing the output power of the STAP filter with respect to the output noise power

$$\eta(k) = \frac{\left|\mathbf{w}_n^H \mathbf{x}_k\right|^2}{\mathbf{w}_n^H \mathbf{R}_k \mathbf{w}_n} \tag{3.22}$$

where $\mathbf{R}_k$ is the interference covariance matrix and $\mathbf{x}_k$ is the single snapshot associated with the hypothesized range bin $k$. The weight $\mathbf{w}_n$ is obtained by normalizing the SMI weight (3.18) as follows

$$\mathbf{w}_n = \frac{\mathbf{R}_k^{-1}\mathbf{s}}{\mathbf{s}^H \mathbf{R}_k^{-1}\mathbf{s}}. \tag{3.23}$$

This normalization provides the desired CFAR behavior which is implemented by a threshold independent of range and also an equivalence to cell averaging CFAR. A new AMF CFAR test statistic $\eta(k)$ for each range bin $k$ can be expressed based on

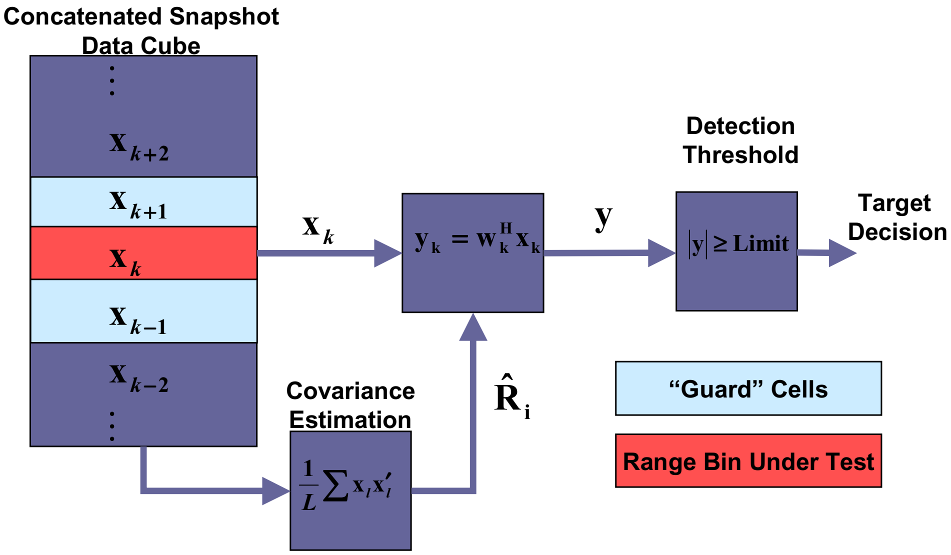

Figure 3.5: Basic STAP Adaptive Signal Processing and Detection Chain; For each range bin $\mathbf{X}_k$, adaptive weight is derived from adjacent bins after *excluding* $\mathbf{X}_k$ and some guard cells; STAP output $y_k$ is tested for target presence at a specified azimuth angle and Doppler frequency

(3.23) and (3.22)

$$\eta(k) = \frac{\left|\mathbf{s}^H \mathbf{R}_k^{-1} \mathbf{x}_k\right|^2}{\mathbf{s}^H \mathbf{R}_k^{-1} \mathbf{s}} \gtrless \alpha, \tag{3.24}$$

where $\alpha$ is a threshold computed for some acceptable false alarm probability. This test statistic is thus proportional to the squared magnitude of the colored noise linear matched filter. In addition, the normalized weight (3.23) is also observed equivalent to the MVDR weight (2.10) described before, and therefore the CFAR detection test (3.22) can be realized directly from the MVDR weight.

Full-rank STAP methods utilize all available degrees of freedom (DOF) for interference suppression, thus requiring large sample support and impractical implementation cost. In addition, these approaches were theoretically based on the underlying assumptions that the noise was Gaussian, as well as independent and identically distributed (i.i.d.) over range. Future airborne surveillance radar drives the requirement for larger numbers of degrees of freedom, which also drives the need for larger numbers of i.i.d. samples. In general, the number of required samples is at least on the order of twice the number of the radar's degrees of freedom [52] to fulfill the above assumptions. Specifically, in order for the expected output signal-to-interference plus noise (SINR) value to be within 3 dB of the optimum SINR requires at least $2 * M * N$ number of i.i.d. samples, which may not be available and realizable in the real world. The need for adequate covariance estimation is one major factor motivating reduced-rank STAP algorithms, which provide near-optimum clutter suppression at reduced sample support and computation, and therefore are of great interest. The concepts of rank reduction will be described in the next section.

## 3.3 Rank of the Covariance Matrix

In general, rank can be interpreted as the number of dominant statistical unknowns associated with the interference statistics and it dictates the required number of degrees of freedom and sample support. The number of dominant statistical unknowns is essentially the number of interference eigenvalues, which can be obtained from an eigenspectrum of the covariance matrix.

In essence, an eigenspectrum contains the rank-ordered eigenvalues of a covariance matrix. The covariance matrix can be decomposed into eigenvector and eigenvalues as follows [43]

$$\mathbf{R} = \mathbf{E}\boldsymbol{\Lambda}\mathbf{E}^H \tag{3.25}$$

where $\boldsymbol{\Lambda}$ is the diagonal matrix of eigenvalues and $\mathbf{E}$ is the unitary matrix of eigenvectors. Since $\mathbf{R}$ is Hermitian and positive definite, the eigenvalues are real and positive. The eigenvalue distribution of an interference and noise covariance matrix usually exhibits how much subspace space has been occupied by the interference and dominant statistical unknowns. This number also gives an indication of the number of degrees of freedom of the interference scenario.

As an example, the simulation environment for the results shown in Figure 3.4 is reconstructed and an eigenspectrum of the same clutter covariance matrix is examined in Figure 3.6. A clear distinction between clutter (on the left) and the floor of identical noise eigenvalues can be identified as a sharp transition at a value of the eigenvalue index of 27. This is denoted as the number of clutter eigenvalues, or equivalently the effective rank of the covariance matrix, and it is identical to $N + M - 1$. Note that noise level is 0 dB, the clutter-to-noise ratio (CNR) is 60 dB per element and pulse, and the maximum array gain is 23 dB (same as $10\times log(14\times 14)$), since 14 elements

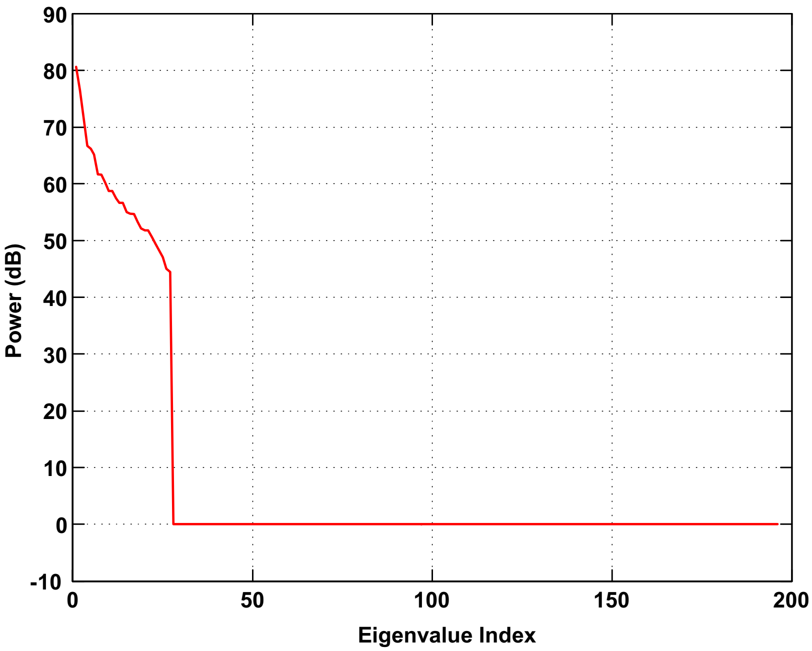

Figure 3.6: Eigenspetra of Clutter Covariance Matrix: Eigenvalue power (dB) vs. eigenvalue index; Number of elements, $N = 14$; Number of pulses, $M = 14$ pulses; Clutter-to-noise ratio, $CNR = 60$ dB; Clutter foldover factor, $\beta = 1$

and 14 pulses were employed. The maximum beamformer output power is 82 dB which is approximately equal to the sum of 60 dB and 23 dB, and is consistent with our simulation results.

Brennan and Staudaher [7] found the following rule for the number of effective rank of the space-time clutter covariance matrix of a sidelooking linear array

$$Rank = int\left\{N + \beta(M-1)\right\}, \tag{3.26}$$

where $int\left\{\right\}$ denotes the next integer number and $\beta$ is clutter foldover (3.14), which is the number of one-half element spacings traversed by the platform during one PRI.

A rigorous proof for this rule has been published by Ward [69]. Brennan's rule

(3.26) provides much insight into the characteristics of the clutter ridge, giving a predictor of the numerical significance of the rank. An intuitive explanation could be reasoned that, as the uniform linear array moves, identical clutter observations are in effect repeated by different elements from different pulses. The effective rank is generally defined as the number of distinct effective element positions during a coherent pulse interval (CPI) and only a small set of independent observations would effectively contribute to the clutter rank [69]. This provides a motivation for reduced-rank techniques. For airborne radar applications, as the number of degrees of freedom is larger, the underlying rank of the interference is usually much smaller than the total available degrees of freedom. Reduced-rank STAP techniques directly adapt only to the effective rank or number of dominant statistical unknowns associated with the interference. As a result, near-optimum clutter suppression can be achieved at reduced sample support and computation complexity.

## 3.4 Eigenvalue Spreading

Eigenvalue spreading refers to an increase in the number of interference eigenvalues of the covariance matrix due to a multitude of real-world effects. The analysis leading to Brennan' rule (3.26) assumed an ideal clutter covariance with a uniform linear array and no eigenvalue spreading. In practice, eigenvalue spreading is always present particularly in nonhomogeneous environments, causing a significant increase in the interference eigenvalues and thus the rank of the covariance matrix. It is due to many factors such as aircraft crabbing, non-linear array geometry, intrinsic clutter motion, and scattering from near-field obstacles, such as the wing on the airborne platform [4], [31], [69]. These factors spread the clutter ridge (in Figure 3.4) off the diagonal line and the net result is an increase in the number of degrees of freedom for effective interference cancellation. In practice, eigenvalue spreading is most often caused by intrinsic clutter motion (ICM), and a model for simulating the effects of ICM will be described in this subsection.

Eigenvalue spreading due to aircraft crabbing can be observed in a side-mounted array antenna when the platform velocity direction is not aligned with the antenna array axis. This will induce ambiguous clutter Doppler frequency from the antenna backlobes and require more adaptive degrees of freedom. Eigenvalue spreading can also result from using a nonlinear array, such as a circular array geometry. For uniform linear arrays (ULAs), the clutter rank is minimized due to the redundancy inherent in the configuration. The rank with the circular array is however much higher, since its element spacing is non-uniform when projected onto a linear aperture. Eigenvalue spreading is also caused by reflections from near-field obstacles, because scattering from ambiguous azimuth angles due to obstacles induces a higher clutter rank.

Eigenvalue spreading is most often observed from the effect of internal clutter motion which is due to fluctuations of the clutter return from pulse to pulse. Many factors, due to both the radar system design and the environment, may cause the echo from a single clutter patch to fluctuate from pulse to pulse. This may be due to the movement of a mechanically scanning antenna or any pulse-to-pulse instability in a nonstationary environment. The presence of ICM induces a broadening of the Doppler spectrum of a single clutter echo, which creates a higher clutter rank and in turn requires a wider clutter notch filter. This effect of pulse fluctuations can be modeled by observing the clutter echo (3.11) from an $i^{th}$ clutter patch

$$\mathbf{x}_c = \alpha_i \mathbf{v}_i = \alpha_i \mathbf{b}_i \otimes \mathbf{a}_i. \tag{3.27}$$

Temporal fluctuations can be represented by replacing the single amplitude $\alpha_i$ above with the $M \times 1$ vector

$$\boldsymbol{\alpha}_i = \left[\alpha_{i,0};\ \alpha_{i,1}; \dots ;\ \alpha_{i,M-1}\right], \tag{3.28}$$

where $\alpha_{i,m}$denotes the random amplitude for the $i^{th}$ scatterer from the $m^{th}$ pulse. The clutter can be modeled as a distribution of randomly located scatterers having a Gaussian distribution of radial velocity, with a variance $\sigma_c^2$.

A Gaussian correlation function is related to a Gaussian power spectrum by the equivalence [43]

$$\exp\left\{-\frac{\sigma_c^2}{2} T_r^2\right\} \Longleftrightarrow \sqrt{\frac{2\pi}{\sigma_c^2}} \exp\left\{-\frac{\omega^2}{2\sigma_c^2}\right\}, \tag{3.29}$$

where $\sigma_c$ is the spectral standard deviation, $T_r$ is the pulse repetition interval and $\omega$ is angular frequency. Thus, the temporal autocorrelation of the fluctuation at a time difference $m$ is defined by

$$\gamma(m) \approx E\left\{\boldsymbol{\alpha}_{l+m} \boldsymbol{\alpha}_l^*\right\} = \xi_k \exp\left\{-\frac{\sigma_c^2 T_r^2}{2} m\right\}, \tag{3.30}$$

where $\boldsymbol{\alpha}_l$ is the clutter scatterer's random amplitude and $\xi_k$ denotes the associated clutter-to-noise (CNR) ratio. The spectral standard deviation $\sigma_c$ is normally normalized to avoid the dependence on the operating wavelength. It can be expressed in terms of a velocity standard deviation $\sigma_v$ with a unit of meters per second $(m/s)$, given by

$$\sigma_v = \frac{\lambda_o \sigma_c}{4\pi}, \tag{3.31}$$

where $\lambda_o$ denotes the operating wavelength. Equation (3.30) can be used to generate an $M \times M$ matrix that represents temporal correlation due to the effect of ICM.

This effect is assumed unchanged over $N$ sensor elements and the space-time clutter covariance matrix with ICM can then be simulated for different values of $\sigma_v$. Measured values of $\sigma_v$ for various types of clutter and environments are common in most radar text books [58].

As an example, the effect of eigenvalue spreading can be observed as shown in Figure 3.7, which displays the eigenspectra of a clutter covariance when the velocity standard deviation $\sigma_v$ is varied from 0 to $2m/s$. The simulation is implemented with an airborne side-looking radar employing a horizontal linear array aligned with the platform direction. The array consists of $N = 18$ elements, half-wavelength spaced, and an $M = 10$ pulse coherent processing interval (CPI). The clutter-to-noise ratio (CNR) per element and pulse is 40 dB. In addition, it is assumed that the platform velocity and radar pulse repetition (PRF) are selected similar to the values chosen in Figure 3.4 so that the clutter foldover term $\beta = 1$. All remaining parameters are assumed standard and identical to the previous example.

The results follow Brennan's rule (3.26) when intrinsic clutter motion (ICM) is not present ($\sigma_v = 0m/s$). In this case, the expected rank is defined as, $r_c = [N + (M-1)\beta] = 27$. This value corresponds to highly correlated clutter and a sharp transition from the interference subspace to the noise subspace. Nonzero intrinsic clutter motion has little effect on the portion corresponding to the largest eigenvalues. The clutter velocity standard deviation $\sigma_v$ is proportional to the spectral standard deviation (3.31). As this value increases, the tails of the eigenspectrum become larger and the rank of the covariance increases (3.29). Note that for a typical airborne radar clutter environment, the average intrinsic clutter velocity is about $0.4m/s$ at which the clutter rank is close to 55. When $\sigma_v$ reaches $2m/s$, the clutter

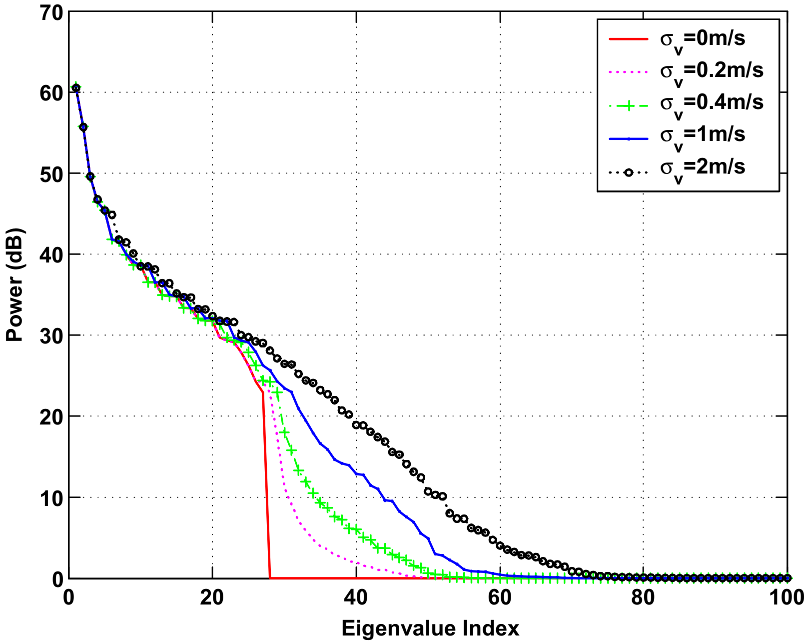

Figure 3.7: Eigenspectra of Clutter Covariance Matrix with Intrinsic Clutter Motion: Eigenvalue power (dB) vs. eigenvalue index; Intrinsic clutter velocity ($\sigma_v$) is varied from $0m/s$ to $2m/s$; As $\sigma_v$ is increased, the rank also increases; Number of elements, $N = 18$; Number of pulses, $M = 10$ pulses; Clutter-to-noise ratio, $CNR = 40$ dB; Clutter foldover factor, $\beta = 1$.

rank is close to 80. A higher rank is equivalent to a requirement for more degrees of freedom (DOF) and more sample support for effective clutter cancellation. As observed, the effective rank of the radar covariance matrix is much smaller compared with total DOF ($M * N = 180$). Rank-reduction STAP techniques, that will be presented later, exploit this low-rank property to minimize required sample support and simultaneously be robust to eigenvalue spreading.

| **Radar Parameters** | |
|---|---|
| Operating frequency | 450 MHz |
| PRF | 600 Hz |
| Platform velocity | 100 $m/s$ |
| Velocity misalignment angle | $0^0$ |
| Number of clutter foldovers | $\beta = 1$ |
| Clutter is assumed unambiguous in Doppler | |
| Number of clutter patches | 360 |
| Clutter Intrinsic velocity ($\sigma_v$) | 0 $m/s$ |
| Antenna element spacing ($d$) | $\lambda_0/2$ |
| Transmit Taper | Uniform |

Table 3.1: Radar System Parameters for STAP Examples

## 3.5 Fully Adaptive Performance

The performance of full-adaptive STAP approaches will be demonstrated and analyzed for an airborne sidelooking radar. As alluded to previously, fully adaptive STAP approaches utilize all degrees of freedom and are considered optimum when sufficient samples are available. Standard assumptions on the target and interference were discussed in Section 3.1. The platform parameter and interference scenarios given in Table 3.1 and a number of performance metrics described later will be used to evaluate STAP performance in this subsection and in subsequent chapters as well. Ideal clutter covariance matrices (3.12) will be implemented in the simulation to obtain optimum results, which will be examined under a variety of performance metrics and environment parameters.

### 3.5.1 Performance Metrics

The adapted beampattern (weight response) power $P_w(\upsilon, \omega)$ as a function of azimuth angle and Doppler frequency indicates STAP processor performance, which is a common performance metric and defined by

$$P_w(\upsilon, \omega) = \left|\mathbf{w}^H \mathbf{v}(\upsilon, \omega)\right|^2, \tag{3.32}$$

where $\mathbf{w}$ is the adapted weight, and $\mathbf{v}$ is the space-time steering vector which depends on the normalized azimuth angle and Doppler frequency, denoted as $\upsilon$ and $\omega$ respectively. The adapted pattern power is obtained by varying $\upsilon$ and $\omega$, and the result is a two-dimensional angle-Doppler frequency response. For a uniform linear array and fixed pulse repetition interval (PRF), the pattern is a two-dimensional Fourier transform of the adaptive weight vector $\mathbf{w}$. Ideally, the response should have nulls in the direction of interference sources, such as clutter ridges and jamming, and exhibit high gain at the presumed target angle and Doppler frequency.

Another important metric is to express STAP performance in term of signal-to-interference-and-noise ratio loss (SINR loss), relative to what could be obtained in an environment with no interference. In a noise-only environment without clutter and jamming, the optimum matched-filtering output signal-to-noise ratio ($SNR_0$) is defined

$$SNR_0 = MN\xi_t, \tag{3.33}$$

where $\xi_t$ is the input signal-to-noise (SNR) ratio per element and pulse, and the gain of $M * N$ represents coherent spatial and temporal array integration over $N$ antenna elements and $M$ pulses. The SINR loss is defined as the output SINR (2.6) relative to the matched filter output SNR in an interference-free environment, given by

$$SINR_{loss} = \frac{SINR}{SNR_0}. \tag{3.34}$$

### 3.5.2 Numerical Results

The first example examines a weight response of fully adaptive STAP techniques as a function of normalized azimuth angle and Doppler frequency. The platform parameter and interference scenarios were given in Table 3.1. The linear array used in this study has $N = 18$ elements and $M = 10$ pulse coherent processing interval (CPI). The clutter-to-noise ratio (CNR) is 40 dB per element and pulse. It is assumed that there is no velocity misalignment (i.e. no platform crabbing) and no intrinsic clutter motion present. The target is located at the boresight (0°) with a normalized Doppler frequency of 0.25 and the associated signal-to-noise (SNR) ratio is 0 dB. In addition, there are two jamming sources present at $(-30°, 60°)$, and each exhibits a jammer-to-noise ratio (JNR) of 30 dB per element.

The resulting adaptive weight response is shown in Figure 3.8, in which the adaptive beampattern power is displayed as a function of normalized azimuth angle and Doppler frequency. Note that the beampattern power was defined in 3.32. The pattern mainlobe is observed at the presumed target location with azimuth angle at 0° and normalized Doppler frequency at 0.25. The two jammers are suppressed by deep nulls at the jammers' azimuth angles $(-30°, 60°)$. These vertical nulls extend over all Doppler frequencies because jamming is known to be uncorrelated from pulse to pulse. Note that the clutter ridge is successfully cancelled, and clearly shows as a two-dimensional slant null that is distributed from the top left corner to the bottom right corner of the display, and occupies both mainlobe and sidelobe clutter. This

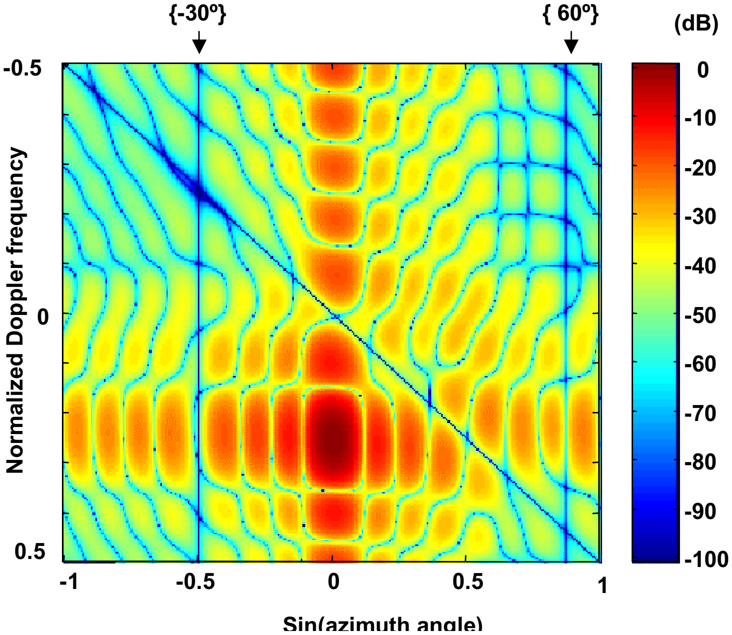

Figure 3.8: Fully Adaptive STAP Weight Response: Receiver output power(dB) vs. normalized Doppler frequency and sin(azimuth angle); Doppler frequency is normalized to PRF; Element spacing, $d = 0.5\lambda_o$; Number of elements, $N = 18$; Number of pulses, $M = 10$ pulses; Clutter-to-noise ratio, $CNR = 40$ dB; Clutter foldover factor, $\beta = 1$; Jammers are at -30 and 60 degrees; Jammer-to-noise (JNR), $JNR = 30$ dB each; Target location $= 0°$ with normalized Doppler frequency $= 0.25$; Signal-to-noise ratio (SNR), $SNR = 0$ dB

also illustrates a direct linear variation between Doppler frequency and azimuth angle as discussed previously (3.15) when the clutter foldover factor $\beta$ is equal to 1.

The SINR loss performance for full-adaptive STAP techniques implemented with number of pulses $(M)$ and sensor elements$(N)$ between 4 and 32 is shown in Figure 3.9. Note that the SINR loss performance metric was defined in 3.34, which is the reduction of array output SINR relative to the optimum matched filter output SNR in a white noise environment. A uniform linear array with half-wavelength spacing is again assumed. There is a desired target at the boresight, with its normalized

Doppler frequency varied from $-0.5$ to $0.5$. The target signal-to-noise (SNR) is 0 dB and the clutter-to-noise ratio (CNR) is 40 dB per element and pulse.

As expected, full-adaptive STAP approaches produce a minimum SINR loss for most of the Doppler space. When more degrees of freedom are available and when $M$ and $N$ are larger, the optimum signal-to-noise (SNR) is improved, and the SINR loss is reduced further. As the Doppler frequency is near 0 Hz, the SINR loss is significantly degraded, because it is close to the mainlobe clutter at both azimuth angle and Doppler frequency. Thus, the target will be undetectable when it has low speed and falls into the response null at the mainlobe clutter. Responses with higher values of $M$ and $N$ result in more desirable narrower null width, and targets have lower minimum detectable velocity (MDV).

Full-adaptive STAP approaches utilize all available degrees of freedom $(M * N)$ and require the inversion of the covariance matrix. This is unreasonable to implement in practice, due to high computation cost and large sample support requirement. In addition, since the covariance matrix is generally not known and must be estimated from the underlying statistics, it may suffer weak convergence in adaptation. As alluded to previously, for an airborne radar environment, the effective rank of the clutter covariance matrix is significantly smaller than the total rank $(M * N)$, especially when $M$ and $N$ are large numbers. Reduced-rank techniques may be exploited to achieve significant reduction in the sample support and computation complexity with little or no sacrifice in performance relative to the fully adaptive case.

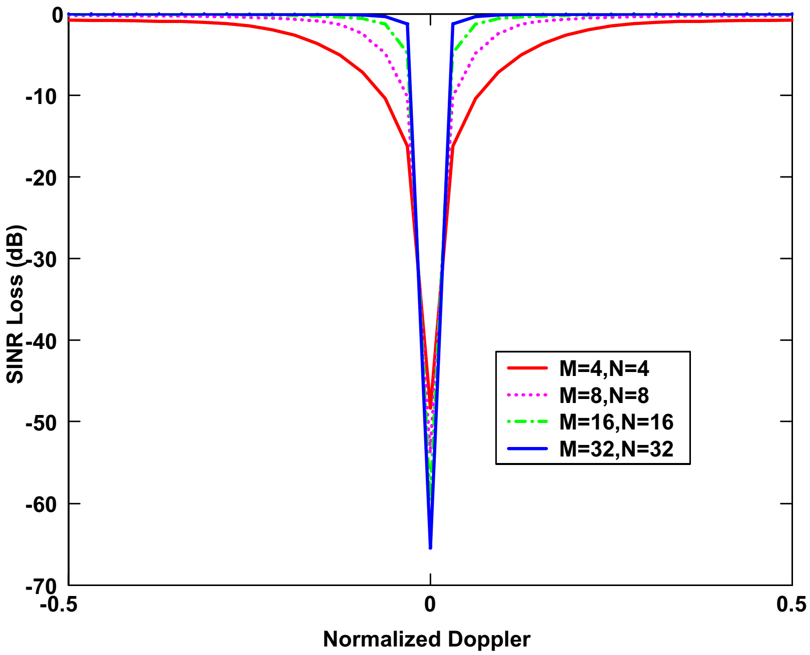

Figure 3.9: Fully Adaptive Performance: SINR loss (dB) vs. target Doppler frequency; Doppler frequency is normalized to PRF; Target azimuth angle is at boresight; Signal-to-noise ratio, $SNR = 0$dB; Number of elements, $N$ is varied from 4 to 32; Number of pulses, $M$ is varied from 4 to 32; Clutter-to-noise ratio, $CNR = 40$dB; Clutter foldover factor, $\beta = 1$

## 3.6 Summary

This chapter begins with a generic radar system model for the signals received from an airborne radar. A space-time snapshot was defined to be the slice of the datacube corresponding to a single range bin. This data may contain a target component as well as undesired components due to noise, jamming, and clutter. The target signal is modeled as a random amplitude times a space-time steering vector that has the target's azimuth and elevation angles and Doppler frequency. The undesired signal components are modeled as random processes. The use of space-time adaptive signal processing (STAP) is required because the two-dimensional extent of ground clutter exhibits both azimuth angle and Doppler frequency.

A STAP processor is composed of $N$ antenna elements which provide spatial degrees of freedom and a $M$-tap Doppler filterbank with time lags that correspond to the radar pulse repetition interval (PRI). The total number of adaptive space-time degrees of freedom is then $N_{dof} = MN$. Fully adaptive STAP can be implemented using the sample matrix inverse (SMI) or the Wiener filter. These approaches however require computational complexity and are optimum only when the statistics of the interference are known. Next, the well-known Brennan's rule in STAP that helps determine the expected rank of an ideal clutter covariance matrix was described. In practice, the effective rank of the clutter covariance matrix is much larger than the expected rank predicted by Brennan's rule.

These concepts provide an introduction to the effect of eigenvalue spreading, which refers to an increase in the number of interference eigenvalues of the covariance matrix due to real-world effects such as aircraft crabbing, non-linear array geometry, intrinsic clutter motion (ICM), and scattering from near-field obstacles. Eigenvalue spreading can be modeled by simulating the effect of intrinsic clutter motion (ICM), which refers to the fluctuations from pulse to pulse. In practice, eigenvalue spreading is always present particularly in nonhomogeneous environments, causing a significant increase in the rank of the covariance matrix and the required larger number of degrees of freedom for effective interference cancellation. These shortcomings lead in the next chapter to the consideration of reduced-rank algorithms.

# Chapter 4

# Reduced Rank Adaptive Signal Processing

As described previously, fully adaptive signal processing techniques are quite computationally intense and may not even be possible for real-time operation. Moreover, these approaches were theoretically based on the underlying assumptions that the noise was Gaussian, as well as independent and identical distributed (i.i.d.) over range. Future airborne surveillance drives the requirement for larger numbers of degrees of freedom, which also drives the need for larger numbers of homogeneous samples. The number of required samples must be on the order of the number of the radar's degrees of freedom to fulfill the above assumptions. In addition, as real-world environments could be unpredictable and nonstationary, the acquisition of a sufficiently large number of homogeneous samples may be impossible. Consequently, it is very difficult to satisfy these underlying statistical assumptions. Reduced-rank signal processing techniques operate directly and reduce the number of the rank associated with the interference. These techniques promise near or better than full adaptive signal processing performance at reduced sample support and computation, and are of great interest. For airborne radar applications, as the degrees of freedom are larger, the underlying rank of the interference is usually smaller than the total available degrees of freedom [24]. Rank reduction techniques can be exploited for effective airborne clutter suppression while meeting the above underlying assumptions.

In this section, three adaptive reduced-rank approaches will be introduced. The first method is based on a principal-components decomposition of the interference-only covariance matrix [65], which is also known as the eigencanceller method [35]. The second method is based on the cross-spectral metric (CSM) information [26], which measures the cross-correlation between the desired signal and observed interference data correlated with the desired signal. This CSM information is used to rank the relative contribution of related eigenvectors in order to minimized the output mean square error. The third method is the recently developed multistage Wiener filter technique (MWF), which has been demonstrated to have the best performance at a much lower rank than any other reduced rank method [23], [24], [25]. Finally, numerical results based on both ideal covariance matrices and estimated covariance matrices will be presented to examine the performance of these approaches. More importantly, the SINR loss will be assessed as a function of both the effective rank and the amount of training data in the presence of eigenvalue spreading. This SINR loss is called the region of convergence for adaptivity (ROC) which provides an informative way to analyze the potential benefits of the new approach as a function of finite sample support with eigenvalue spreading. Results that were published previously have not examined the MWF performance in the presence of eigenvalue spreading

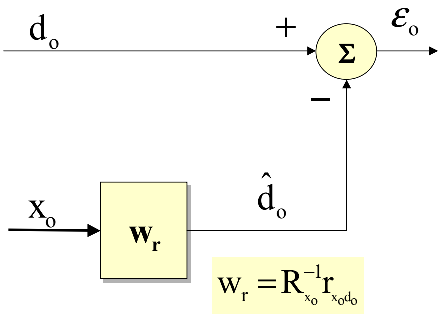

Figure 4.1: Classical Wiener Filter; $d_0$ = desired signal; $\mathbf{x}_0$ = observed data vector; $\mathbf{w}_r$ = Wiener filter weight vector; $\widehat{d_0}$ = estimate of desired signal; $\varepsilon_0$ = error signal

## 4.1 Principal Components (PC)

In general, the principal-components (PC) approach can be simply implemented in a direct form structure, in which eigenvalue decomposition is directly obtained from the total interference covariance matrix. It can also be implemented as a signal dependent structure based on the classical Wiener filter structure as illustrated in Section 2.4.

The Wiener filter is reconstructed in Figure 4.1 for convenience, in which the scalar process $d_0$ represents the "desired" signal that is usually the output of the conventional beamformer and the process $\mathbf{x}_0$ is the observed data vector consisting of data different from the desired signal that is received at a sensor array. The optimum weight that minimizes the output mean square error (MMSE) between $d_0$ and its estimate $\widehat{d_0}$ is repeated here as

$$\mathbf{w}_r = \mathbf{R}_{x_0}^{-1}\mathbf{r}_{x_0 d_0}, \tag{4.1}$$

where $\mathbf{R}_{x_0}$ is the covariance estimate of the noise process $\mathbf{x}_0$, and $\mathbf{r}_{x_0 d_0}$ is the cross-correlation between the processes $d_0$ and $\mathbf{x}_0$.

The principal-components (PC) approach, as implied by its name, selects and truncates only those dominant eigenvectors of the interference-plus-noise covariance matrix. In particular, the PC technique approximates $\mathbf{R}_{x_0}$by the retention of $K$ dominant eigenvectors of the following Karhunen-Loeve expansion [65]

$$\mathbf{R}_{x_o} \simeq \mathbf{R}_{pc} = \mathbf{E}\boldsymbol{\Lambda}\mathbf{E}^H = \sum_{i=1}^{K} \lambda_i \mathbf{E}_i \mathbf{E}_i^H, \tag{4.2}$$

where $K < N-1$ and $\mathbf{E}$ is the $(K \times K)$ matrix that contains eigenvectors $\mathbf{E}_i$. Note that $\boldsymbol{\Lambda}$ is the diagonal matrix of corresponding eigenvalues $(\lambda_i\ )$ where $\lambda_1 \geqslant \lambda_2 \geqslant ...\lambda_{N-1}$. In this case, $K$ is the assumed rank of the major interference, which also corresponds to the number of largest eigenvalue magnitudes to be retained.

The PC weight vector is then given by

$$\mathbf{w}_{pc} = \mathbf{R}_{pc}^{-1}\mathbf{r}_{x_0 d_0} = \sum_{i=1}^{K} \frac{\mathbf{E}_i^H \mathbf{r}_{x_0 d_0} \mathbf{E}_i}{\lambda_i}. \tag{4.3}$$

The resulting covariance matrix ($\mathbf{R}_{pc}$) is the best low rank representation of the full-rank covariance ($\mathbf{R}_{x_0}$), provided that $\mathbf{R}_{pc}$ contains essentially the dominant subspace of the color portion of the interference subspace. This will provide the lowest minimum mean square error (MMSE) and the maximum SINR on this eigensubspace.

When the interference is strongly low rank, $K$ is much smaller than $N-1$ and the approach can provide a sufficient degree of adaptation with less observed data. However, the technique is inherently not well suited when $K$ is not clearly defined and a dominant interference subspace is not clearly present, as is typical for non-homogeneous environments with eigenvalue spreading. As will be shown later, its performance degrades poorly in eigenvalue spreading. Moreover, when selecting the dominant eigenvectors, this technique does not utilize the signal steering vector of interest. In general, it can only achieve a maximum rank reduction to the effective rank of the signal subspace. As a result, it does not achieve maximum compression relative to the cross-spectral metric method which will be described in the next section. The cross-spectral metric technique can further compress data rank below the signal subspace dimension without adversely affecting the mean square error (MSE) performance.

## 4.2 Cross Spectral Metric (CSP)

The cross-spectral metric (CSP) technique [26] utilizes knowledge of the signal steering vector to provide a deeper insight to the rank-reduction and dimensionality reduction, thereby achieving greater subspace compression.

The CSP rank reduction method selects only those eigenvectors contributing to maximize the output SINR, or equivalently to minimize the output mean square error (MSE) of the Wiener filter. The minimum mean square error (MMSE) (2.13) can be expressed in terms of the eigenvectors ($\mathbf{E}_i$) and corresponding eigenvalues ($\lambda_i$) of $\mathbf{R}_{x_o}$

$$\xi_o = \sigma_d^2 - \mathbf{r}_{x_0 d_0}^H \mathbf{R}_{x_0}^{-1} \mathbf{r}_{x_0 d_0} = \sigma_d^2 - \sum_{i=1}^{N-1} \frac{\left|\mathbf{E}_i^H \mathbf{r}_{x_0 d_0}\right|^2}{\lambda_i}, \tag{4.4}$$

where $\sigma_d^2$ is the desired signal power, $\mathbf{R}_{x_0}$is the covariance estimate of process $\mathbf{x}_0$, and $\mathbf{r}_{x_0 d_0}$ is the cross-correlation between the processes $d_0$ and $\mathbf{x}_0$.

By examining (4.4), it is apparent that a minimum MSE can be obtained by selecting those $K$ eigenvectors corresponding with the maximum values of the following quantity

$$\frac{\left|\mathbf{E}_i^H \mathbf{r}_{x_0 d_0}\right|^2}{\lambda_i}, \tag{4.5}$$

where $K \ll N-1$. This efficient rank-ordering of the eigenvectors of $\mathbf{R}_{x_0}$ takes into account the cross-correlation between $\mathbf{E}_i$ and $\mathbf{r}_{x_0 d_0}$, which also depends on the signal steering vector $\mathbf{s}$. The new interference covariance is estimated by retaining these eigenvectors and the resulting rank reduction CSP weight can be found

$$\mathbf{w}_{csp} = \sum_{i=1}^{K} \frac{\widetilde{\mathbf{E}}_i^H \mathbf{r}_{x_0 d_0} \widetilde{\mathbf{E}}_i}{\widetilde{\lambda}_i}, \tag{4.6}$$

where it is assumed that $\widetilde{\lambda}_1 \geqslant \widetilde{\lambda}_2 \geqslant ...\widetilde{\lambda}_{N-1}$, and $\widetilde{\lambda}_1$ is corresponded to the largest quantity in (4.5).

Essentially, the CSP approach maximizes the SINR and significantly reduces the rank dimension by selecting only interference eigenvectors maximally correlated with the signal of interest. Thus while the principal-components algorithm simply chooses the eigenvectors corresponding to largest eigenvalues, the CSP technique is more robust since it selects only the eigenvectors which maximize mutual information between the interference and desired process. However, it is still limited to the selection of eigenbasis arising from $\mathbf{R}_{x_0}$, which is not directly influenced by the signal steering vector. Moreover, the CSP technique still requires an eigendecomposition and a matrix-inverse computation, which are not practical for nonstationary and real-world environments. These shortcomings can be resolved with the recently developed multistage Wiener filter approach.

## 4.3 The Multistage Wiener Filter (MWF)

The multistage Wiener filter (MWF) technique extends the traditional Wiener filter structure to form a nested chain of scalar Wiener filter stages, thereby achieving a faster rank reduction [24], [23]. It is also a signal-dependent approach which maximizes information between the desired signal and correlated interference. The weights are estimated to minimize the mean square error (MSE) at each successive stage. Unlike previous adaptive rank-reduction approaches, the MWF technique naturally optimizes data for truncation and requires much less sample support. Additionally, it does not need any overhead for an eigenvector decomposition, calculation of the covariance matrix and the inverse of the covariance matrix. The MWF will first be described in a most simple form using orthogonal decomposition [25] and it will then be examined in a more efficient implementation using a correlation and subtraction architecture (CSA) [53].

### 4.3.1 MWF Decomposition Using Orthogonal Projection

The most simple implementation of the MWF structure is shown in Figure 4.2 which represents an orthogonal decomposition of the Wiener filter.

It is assumed that the reference signal $d_0(k)$ ("mainbeam" signal) and observed data $\mathbf{x}_0(k)$ (noise process) at a snapshot index $k$ are obtained by

$$\begin{aligned} d_0(k) &= \mathbf{s}^H \mathbf{x}(k), && (4.7) \\ \mathbf{x}_0(k) &= \mathbf{B}\mathbf{x}(k), && (4.8) \end{aligned}$$

where $\mathbf{B}$ is a matrix whose rows span the null space of vector $\mathbf{s}$.

The algorithm starts decomposing the observed data $\mathbf{x}_0$ into a set of natural orthogonal basis vectors and its orthogonal null space. Each basis vector $\mathbf{h}_i$ is defined as the normalized cross-correlation between the reference signal $d_{i-1}$ and observed data $\mathbf{x}_{i-1}$ on each previous stage

$$\begin{aligned} \mathbf{h}_i &= \frac{\mathbf{r}_{x_{i-1}d_{i-1}}}{\delta_i}, && (4.9) \\ \text{where } \delta_i &= \left\|\mathbf{r}_{x_{i-1}d_{i-1}}\right\| = (\mathbf{r}^H_{x_{i-1}d_{i-1}} \mathbf{r}_{x_{i-1}d_{i-1}})^{1/2}. && (4.10) \end{aligned}$$

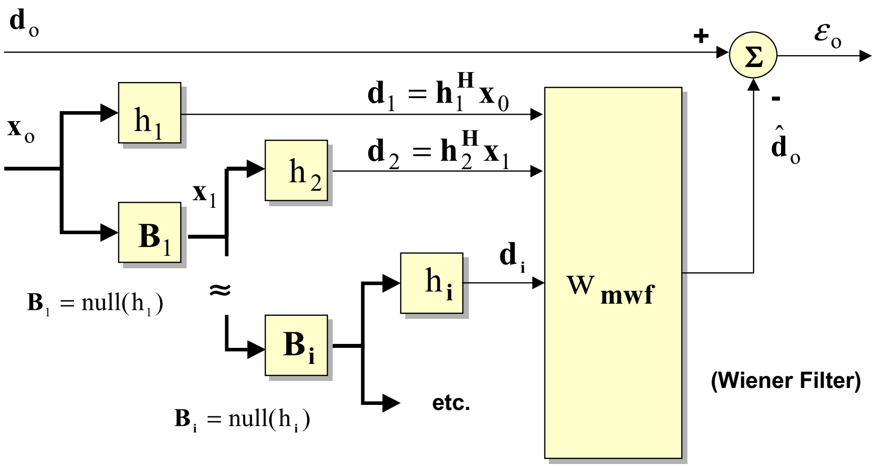

Figure 4.2: Multistage Wiener Filter Orthogonal Decomposition Structure; $d_o =$ desired signal; $d_o = \mathbf{s}^H\mathbf{x}$ where $\mathbf{s}$ is steering vector and $\mathbf{x}$ is array data; $\mathbf{x}_o =$ observed signal; $\widehat{d_0} =$ estimate of desired signal; $\epsilon_o =$ error signal

The reference signal for the next stage is derived from the inner-product between this cross-correlation vector and the current observed data. The observed data for the next stage is formed by projecting the current data onto the orthogonal complement of the current cross-correlation vector. The MWF rank corresponds to the number of stages retained, providing a robust solution and a significant reduction in computation.

The MWF weight is found by minimizing the mean square error between the desired signal and its estimate

$$\mathbf{w}_{mwf} = \mathbf{R}_d^{-1}\mathbf{r}_{dd_0}, \tag{4.11}$$

where $\mathbf{R}_d = E(\mathbf{d}\mathbf{d}^H)$, $\mathbf{r}_{dd_0} = E(\mathbf{d}d_0^H)$, $\mathbf{d} = [d_1\ d_2...d_k]^T$, and $k$ is the number of stages retained. At each stage, the information that is useful for estimating the signal $\widehat{d_o}$ from $\mathbf{x}_o(k)$, is compressed. Signal compression is achieved by successive rank-one subspace selections, which are chosen to minimize the MSE at each stage and compactly represent the correlated interference in the auxiliary branch. This reduction in rank and the decomposition is continued for the extent and the rank of the data until no color noise is present. The full-rank solution is achieved when the stage-to-stage decomposition is continued until the subspace spans the entire original data space.

The final weight can be expressed as

$$\mathbf{w} = \mathbf{s} - \mathbf{B}^H \mathbf{L} \mathbf{w}_{mwf}, \tag{4.12}$$

where

$$\mathbf{L} = \begin{bmatrix} \mathbf{h}_1^H \\ \mathbf{h}_2^H \mathbf{B}_1 \\ \mathbf{h}_3^H \mathbf{B}_2 \mathbf{B}_1 \\ \cdots \\ \mathbf{B}_N \mathbf{B}_{N-1} \ldots \mathbf{B}_2 \mathbf{B}_1 \end{bmatrix}. \tag{4.13}$$

where $\mathbf{B}_i$ is a matrix whose rows span the null space of vector $\mathbf{h}_i$. Note that $\mathbf{L}$ (4.13) represents the subspace formed by the progression of projection of the cross-correlation vectors into the interference data, in which it is truncated to obtain a reduced-rank $\mathbf{R}_d$. In addition, since the MVDR weight (2.10) is equivalent to the Wiener filter, the MWF is essentially a reduced rank version of the MVDR.

### 4.3.2 Efficient Implementation Structures

In practice, the multistage Wiener filter (MWF) is implemented in a modular and scalar form, in which the scalar weights are computed recursively and based on the filter error from each previous stage. This correlation and subtraction architecture

(CSA) of the MWF structure is displayed in Figure 4.3, which employs a new arrangement of the algebra flow that provides significantly greater computational efficiency [53].

The CSA implementation consists of an upper chain which analyzes the data from left to right, and a lower chain which synthesizes the filter weights, the filter output and filter error from right to left. The reference signal $d_0(k)$ and observed data $\mathbf{x}_0(k)$ at a snapshot $k$ were defined in (4.7) and (4.8)

$$\begin{aligned} d_0(k) &= \mathbf{s}^H\mathbf{x}(k), && (4.14) \\ \mathbf{x}_0(k) &= \mathbf{B}\mathbf{x}(k), && (4.15) \end{aligned}$$

where $\mathbf{B}$ is a matrix that projects the data onto the null-space of $\mathbf{s}$. The blocking matrix is conventionally chosen rectangular to account for the result being an $N-1$ dimensional vector. The other possibility is using an $N \times N$ square matrix

$$\mathbf{B} = \mathbf{I} - \mathbf{s}\mathbf{s}^H \tag{4.16}$$

where $\mathbf{I}$ is an $N\times N$ identity matrix. Thus, the standard blocking matrix $\mathbf{B}$ in Figure 4.2 can be replaced using this algebraic expression.

The observed data $\mathbf{x}_0$ can then be expressed using (4.14), (4.15), (4.16)

$$\mathbf{x}_0(k)= (\mathbf{I} - \mathbf{s}\mathbf{s}^{\mathbf{H}})\mathbf{x}(k)= \mathbf{x}(k)-\mathbf{s}d_0(k). \tag{4.17}$$

By accounting for the projection with the subtraction shown in (4.17), the computation cost is significantly reduced over the blocking matrix multiplication in (4.15). Given $d_0(k)$ and $\mathbf{x}_0(k)$ as inputs, the processing continues with a recursion of adaptive stages. The normalized cross-correlation $\mathbf{h}_i$ between the reference signal and observed data on each stage was defined in (4.9). The projection of the data along this direction and orthogonal to this direction are computed as

$$\begin{aligned} d_i(k) &= \mathbf{h}_i^H \mathbf{x}_{i-1}(k) &(4.18)\\ \mathbf{x}_i(k) &= (\mathbf{I} - \mathbf{h}_i \mathbf{h}_i^H)\mathbf{x}_{i-1}(k) = \mathbf{x}_{i-1}(k) - \mathbf{h}_i d_i(k). &(4.19)\end{aligned}$$

In this form, the orthogonal vectors $\left[\mathbf{s}, \mathbf{h}_{1,} \mathbf{h}_{2,} \mathbf{h}_{3,} ..\right]$ all have $N$ entries.

This recursive analysis may be terminated at any desired stage at which the truncation sets the initial error ($\varepsilon_2$) as shown in Figure 4.3 for a 2-stage implementation

$$\varepsilon_2(k) = d_2(k). \tag{4.20}$$

After the analysis is finished, this initialization begins the synthesis along the lower chain of Figure 4.3 from right to left in a recursive fashion. For each adaptive stage $i$ (from $i = 2$ to $i = 1$), the mean square error $\xi_i$, the scalar weight $w_i$, and the filter output $\varepsilon_{i-1}$ can be calculated as

$$\begin{aligned} \xi_i &= \left\langle |\varepsilon_i(k)|^2 \right\rangle, &(4.21)\\ w_i &= \delta_i / \xi_i, &(4.22)\\ \varepsilon_{i-1}(k) &= d_{i-1} - w_i \varepsilon_i(k), &(4.23)\end{aligned}$$

where $\delta_i$ was defined in (4.10). The goal is to obtain the final scalar filter output $\varepsilon_0(k)$, based on the scalar weights obtained from each recursive stage.

When the adaptive weight vector is desired, the synthesis of $\varepsilon_0(k)$ can be expressed in a direct form in order to compare to other filters that use the weight vectors explicitly

$$\begin{aligned} \varepsilon_0(k) &= d_0(k) - w_1\left[d_1(k) - w_2\left[d_2(k) - w_3\left[d_3 - ...\right]\right]\right] &(4.24)\\ &= \left[\mathbf{s}^H - w_1 \mathbf{h}_1^H + w_1 w_2 \mathbf{h}_2^H - w_1 w_2 w_3 \mathbf{h}_3^H + ...\ \right]\mathbf{x}\left(k\right) &(4.25)\end{aligned}$$

This illustrates an equivalent weight vector for the multistage Wiener filter where $\mathbf{x}(k)$ is the data input and $\varepsilon_0(k)$ is the output

$$\mathbf{w} = \mathbf{s}^H - w_1\mathbf{h}_1^H + w_1w_2\mathbf{h}_2^H - w_1w_2w_3\mathbf{h}_3^H + ... \tag{4.26}$$

In general, this weight vector is not needed, since the recursive analysis provides direct access to the filter output $\varepsilon_0(k)$ as shown in Figure 4.3.

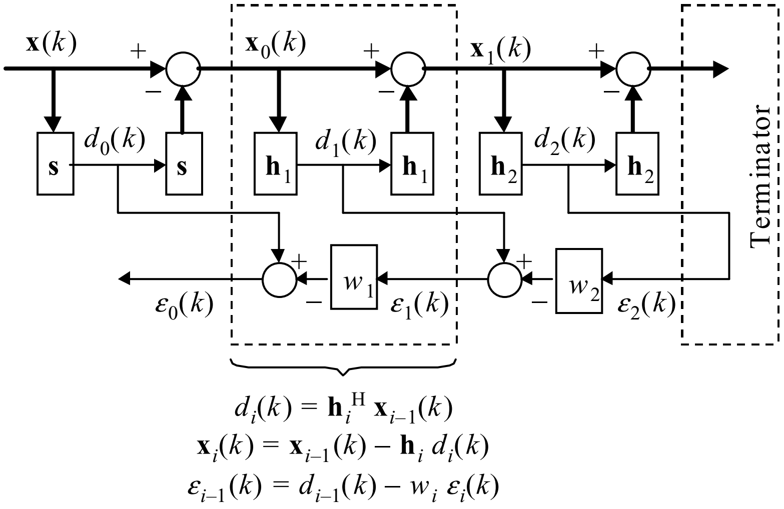

Figure 4.3: Multistage Wiener Filter Correlation Subtraction Architecture; $\mathbf{x}(k)$ = array data; $d_o$ = desired signal; $d_o = \mathbf{s}^H\mathbf{x}$ where $\mathbf{s}$ is steering vector; $\epsilon_o(k)$ = error signal; The upper chain analyzes the data flowing from left to right and the lower chain synthesizes the filter weights flowing from right to left

## 4.4 Numerical Results Using Known Covariance

In this section, relative performance of adaptive rank reduction approaches will be compared using ideal interference covariance with and without the presence of eigenvalue spreading. The performance of these methods using sample statistics will be considered in a subsequent section. In general, the covariance is usually unknown and estimated over a range of data, which may introduce random estimation and convergence errors. In this simulation, the interference covariance is assumed known and can be theoretically computed in order to obtain optimum results.

The theoretical jammer covariance can be computed using (2.7) and the theoretical clutter covariance can be calculated using (3.12). The clutter is assumed unambiguous in Doppler frequency and modeled as a distribution of randomly located scatterers having a Gaussian distribution of radial velocity. All signals and jammers are modeled as narrowband, white, complex Gaussian random processes. In addition, an accurate estimate of the true target steering vector is assumed available to form the adaptive weights. The antenna array is assumed uniform, linear, half-wavelength element spacing, boresight-aligned, and untapered in both spatial and Doppler sidelobes.

First, a simple environment with jamming only is considered as shown in Table 4.1, which defines the signal environment for Test Case 1. This simple one-dimensional (1-D) adaptive beamforming environment helps demonstrate both the underlying concepts and relative performance of the adaptive rank reduction methods with a minimum of application-specific overhead. There are seven signals impinging on the array, representing one desired signal and six independent sidelobe point-source noise jammers. All jammer-to-noise ratios (JNR) are set at 50 dB above receiver noise. All signals are modeled as narrowband, white, complex Gaussian random processes. The sensor array is again assumed to be linear and composed of 16 elements. Since clutter is not present, the number of dominant eigenvectors is six, which is also equal to the effective rank of the interference subspace. The spatial adaptive beampattern

| **Signal** | **Location** | **SNR** |
|---|---|---|
| Desired | 0° | 0 dB |
| Jammer 1 | −65° | 50 dB |
| Jammer 2 | −40° | 50 dB |
| Jammer 3 | −25° | 50 dB |
| Jammer 4 | 30° | 50 dB |
| Jammer 5 | 45° | 50 dB |
| Jammer 6 | 65° | 50 dB |

Table 4.1: Signal Geometry for Test Case 1 (N=16 elements; Location is in azimuth angle)

power as a function of direction sine for the multistage Wiener (MWF) technique is shown in Figure 4.4. Note that the beampattern power was defined in 3.32 and the weight is implemented at a reduced rank of 4. As observed, the MWF response attenuates all six jammers ($J1..J6$) and maintains a maximum gain at the azimuth angle of the desired signal.

Next, the performance of adaptive rank reduction approaches is compared using the same environment. The SINR loss performance as a function of rank is displayed in Figure 4.5, which compares the following rank reduction techniques: principal-components (PC), cross-spectral metric (CSP), and multistage Wiener filter (MWF). Note that the SINR loss performance metric was defined in 3.34, which is the ratio of array output SINR for the target at boresight (azimuth angle = 0°) relative to the optimum matched filter output SNR in a white noise environment. For the PC and CSP cases, rank refers to the number of principal components retained, while for the MWF method, it refers to the stages (basis) truncated in the MWF structure. As expected, optimum performance is obtained by both the PC and CSP approaches for all ranks greater than the number of significant eigenvectors (6), with the CSP technique converging faster. Note that, the SINR loss rolls off slowly for

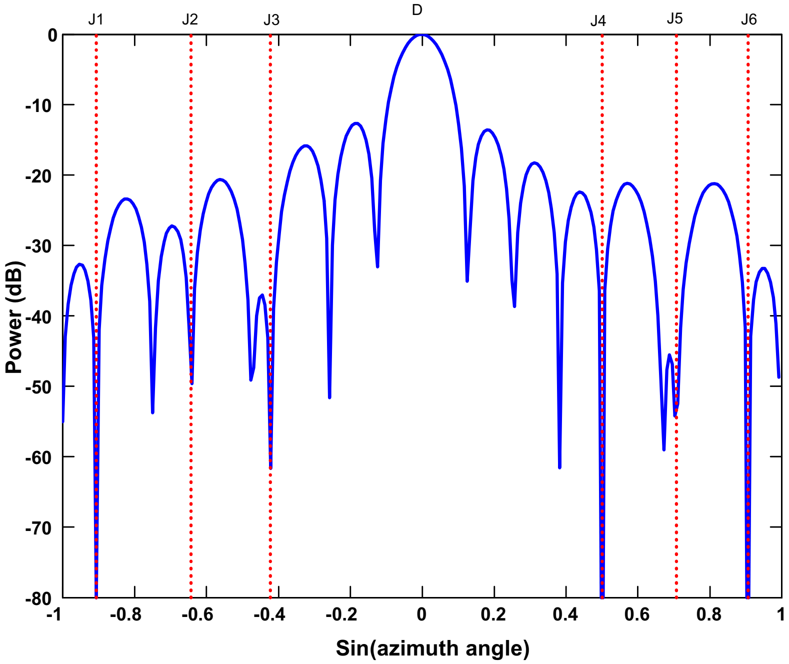

Figure 4.4: MWF Beampatterns: Receiver output power (dB) vs. sin(azimuth angle) (Test Case 1); Rank = 4; Number of elements, $N = 16$; Six jammers are at -65, -40, -25, -30, 45, 65 degrees; $J_1..J_6$ are jamming locations; Jammer-to-noise ratio, $JNR = 50$ dB for each jammer; Target is at boresight with $SNR = 0$ dB

all ranks below 4, because there are simply not enough degrees of freedom (DOF) available to counter the interference. As each rank is increased, PC approaches simply pick a remaining eigenvector with the largest magnitude. On the other hand, the CSP approach utilizes knowledge of a desired steering vector and selects a remaining eigenvector most nearly correlated with the desired steering vector. As a result, it achieves a better SINR and is closer to the optimal Wiener solution. However, it still requires retention of the full jammer subspace before reaching the optimum level. This is as expected, since both the PC and CSP methods still use identical subspace representation. The new multistage Wiener filter structure however outperforms both

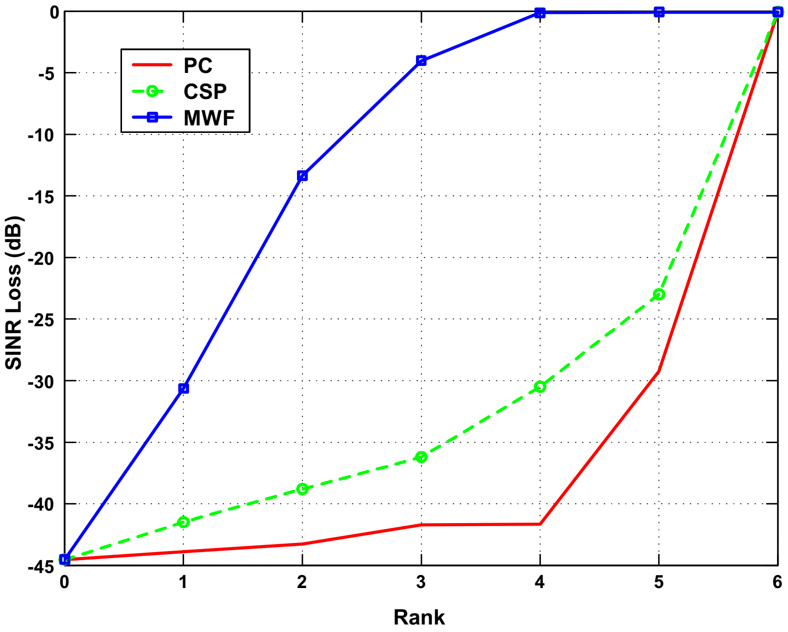

Figure 4.5: Rank Performance for 1-D Array: SINR loss (dB) vs. rank of Wiener filter (Test Case 1); PC = Principal Components; CSP = Cross Spectral Metric; MWF = Multistage Wiener Filter; Number of elements, $N = 16$

of these approaches and rapidly reaches the optimal solution at the $4th$ rank. By selecting a subspace based on both the steering vector and the interference statistics, it provides a better SINR performance in every rank and achieves significant interference rejection within the first few stages of decomposition.

The next example evaluates these rank reduction techniques for two-dimensional (2-D) STAP using a new environment with clutter as shown in Table 4.2, which defines the signal environment for Test Case 2. The platform and radar system parameters were displayed in Table 3.1. The linear array used in this study has a $N = 18$ elements and $M = 10$ pulse coherent processing interval (CPI). The clutter-to-noise ratio (CNR) is 40 dB per element and pulse. It is assumed that there is no velocity

| **Signal** |
|:---:|
| Desired Signal at 0° azimuth angle |
| Desired Signal SNR = 0 dB |
| Normalized Doppler frequency = 0.25 |
| |
| **Clutter** |
| Clutter-to-noise (CNR = 40 dB) |
| Index of Clutter Foldover ($\beta = 1$) |
| Velocity misalignment angle = $0^\circ$ |
| Number of clutter patches = 180 |
| |
| **Antenna Array** |
| Number of elements ($N = 18$) |
| Number of pulses ($M = 10$) |

Table 4.2: Signal Geometry for Test Case 2 (N=18 elements; M=10 pulses; Clutter return from each range sample is the superposition of all clutter patches evenly distributed in azimuth angles)

misalignment (i.e. no platform crabbing) and no intrinsic clutter motion present. The target is located at the boresight (0°), with a normalized Doppler frequency of 0.25 and the associated signal-to-noise ratio (SNR) is 0 dB.

The relative subspace compression performance of these algorithms is displayed in Figure 4.6. The underlying rank of the clutter covariance matrix is defined as rank $= [N + (M-1)\beta] = 27$, based on Brennan's rule (3.26). As predicted, both the PC and CSP approaches reach optimum solutions for all ranks greater than 27, while the CSP performs better. The PC algorithm degrades rapidly if fewer than 20 dominant eigenvectors are retained. The MWF outperforms these two methods in every rank and rapidly obtains an optimum level at rank 12, which is robust for a finite sample support environment.

The relative performance of these algorithms in the presence of eigenvalue spreading is displayed in Figure 4.7. An intrinsic clutter velocity of $\sigma_v = 1m/s$ is added to the data and eigenvalue spreading increases the effective rank of the interference covariance up to 40 as observed. Note that eigenvalue spreading is also equivalent to clutter spectral spreading which increases the rank of the data. As a result, both the PC and CSP approaches converge slowly and do not reach optimal performance until all ranks greater than 40, with the CSP method adapts better. The MWF is again most robust and capable of obtaining an output SINR within 3 dB of the optimum level at a rank of 20, which is much less than that required by the PC and CSP approaches. This is an excellent performance considering the fact that the MWF approach does not require an eigendecomposition of the data covariance matrix. It converges rapidly by robustly compressing interference subspaces and generating new basis through the multistage decomposition.

### 4.4.1 Summary

The MWF was evaluated with the principal components and cross-spectral metric using known covariance matrices in both 1-D spatial-only and 2-D STAP array examples. These results have confirmed the remarkable convergence of the multistage Wiener filter algorithm as a function of rank. The improvement was more clearly observed in an environment with eigenvalue spreading (clutter spectral spreading), where robustness to rank and subspace compression is critical. More importantly, this provides enormous potential in applications for nonhomogeneous environments where eigenvalue spreading is always present and limited sample support is available. The robustness of the MWF in these sample limited environments will be examined

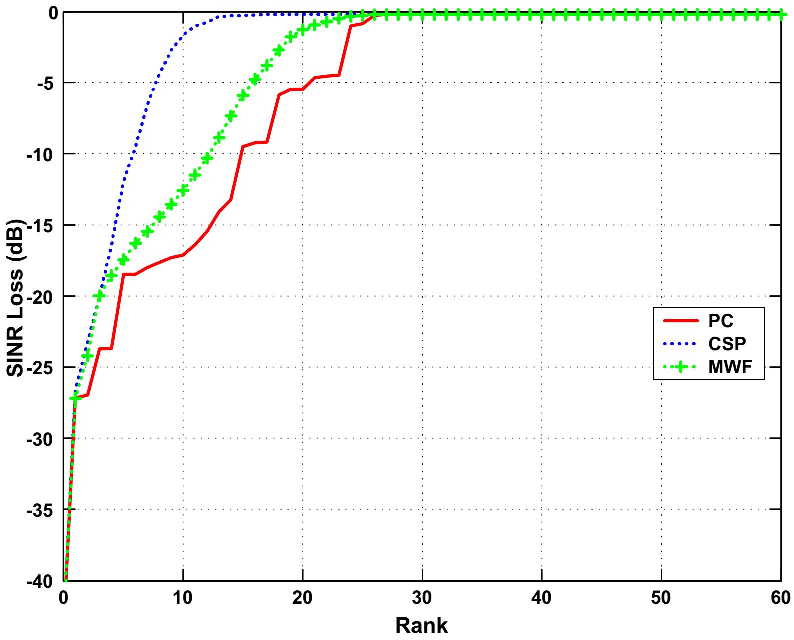

Figure 4.6: Rank Performance for 2-D Array: SINR loss (dB) vs. rank of Wiener filter (Test Case 2); PC = Principal Components; CSP = Cross Spectral Metric; MWF = Multistage Wiener Filter; Number of elements, $N = 18$; Number of pulses, $M = 10$; Clutter-to-noise ratio, CNR = 40dB; Target is at boresight with $SNR = 0$ dB

in the next section.

## 4.5 Numerical Results Using Sample Data

In the last section, the multistage Wiener filter (MWF) approach was examined using ideal interference covariance matrices. Its performance will now be evaluated in sample-limited environments and in the presence of eigenvalue spreading. In these environments, additional losses are expected since the covariance matrices must be estimated from a limited number of samples available. More importantly, the SINR loss is assessed as a function of both the effective rank and the amount of training

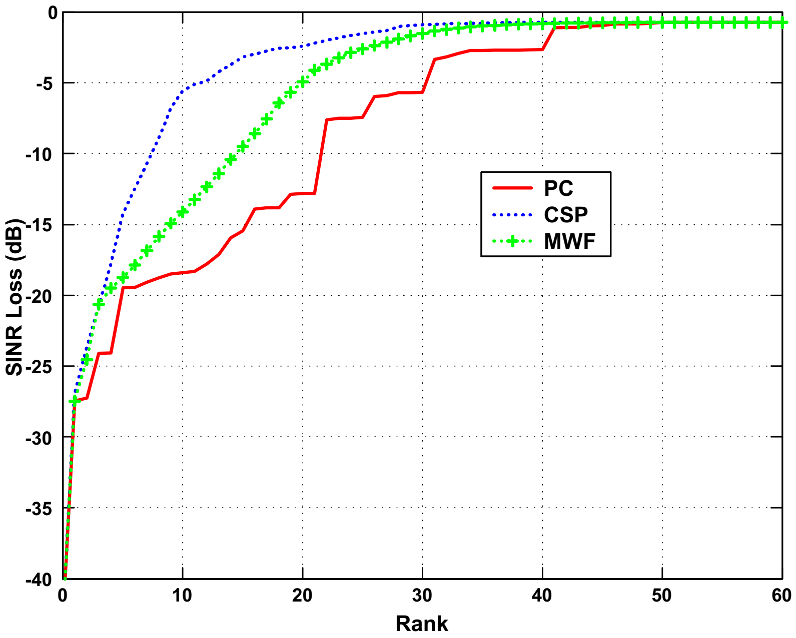

Figure 4.7: Rank Performance for 2-D Array: SINR loss (dB) vs. rank of Wiener Filter for 2-D Array with Intrinsic Clutter Motion (Test Case 3); Intrinsic clutter velocity $(\sigma_v) = 1m/s$; Number of elements, $N = 18$; Number of pulses, $M = 10$; Clutter-to-noise ratio, CNR= 40 dB; Target is at 0° with $SNR = 0$ dB;

data. This SINR loss is called the region of convergence for adaptivity (ROC) which provides an informative way to analyze the potential benefits of the new approach for reduced rank processing as a function of finite sample support. Note that the SINR loss performance metric was defined in 3.34, which is the ratio of array output SINR for the desired target relative to the optimum matched filter output SNR in a white noise environment. The following Monte Carlo simulations consist of 50 independent realizations.

As a baseline example, Table 4.3 defines the signal environment for Test Case 3. The clutter-to-noise CNR is 40 dB per element and pulse, and its foldover factor $\beta$ is equal to 1. The uniform linear array consists of $N = 10$ elements, half-wavelength element spacing, with $M = 10$ pulse CPI. The target is again located at the boresight ($0°$), with a normalized Doppler frequency of 0.25 and the associated signal-to-noise ratio (SNR) is 0 dB. The eigenvalue distribution of the interference covariance matrix is presented in Figure 4.8, with $\sigma_v$ varied from $0m/s$ to $1m/s$. As expected, the underlying rank follows Brennan's rule, which is is equal to $N + (M - 1)\beta$ or 19 when $\sigma_v = 0m/s$ (3.26). Nonzero intrinsic clutter motion has little effect on the portion corresponding to the largest eigenvalues. The clutter velocity standard deviation $\sigma_v$ is proportional to the spectral standard deviation (3.31). As this value increases, the tails of the eigenspectrum become larger and the rank of the covariance increases (3.29). As observed, when $\sigma_v = 1m/s$, the dimension of the noise-subspace eigenstructure is significantly increased to 40. The ROC for the MWF and principal components will be examined for both of these cases.

The ROC response for the principal components (PC) method is displayed in Figure 4.9. The area of this plot where the sample support is less than the rank (the lower-left triangular region) represents the region where the reduced-rank data matrix is numerically unstable. The slope or roll-off of the performance surface represents both the robustness and the sensitivity of the processor as a function of rank and sample support. The lower right region where the SINR loss is negligible represents the region of convergence for adaptivity with respect to the PC method. Recall that the effective rank of the interference covariance matrix is 19, which is also observed as the minimum rank for the PC method to reach the optimum level. The necessary sample support is about 35 as seen.

| **Signal** |
|---|
| Desired Signal at 0° azimuth angle |
| Normalized Doppler frequency = 0.25 |
| Desired Signal SNR = 0 dB |
| |
| **Clutter** |
| Clutter-to-noise (CNR = 40 dB) |
| No. of Clutter Foldover ($\beta = 1$) |
| Velocity misalignment angle= $0^{\circ}$ |
| Number of clutter patches = 180 |
| |
| **Antenna Array** |
| Number of elements ($N = 10$) |
| Number of pulses ($M = 10$) |

Table 4.3: Signal Geometry for Test Case 3 (N=10 elements; M=10 pulses; Clutter return from each range sample is the superposition of all clutter patches evenly distributed in azimuth angles)

The ROC response for the MWF method is displayed in Figure 4.10, which demonstrates a much greater region of support and has vast improvement in SINR for $7 < k < 18$ where $k$ denotes the rank. The PC method, on the other hand, will not converge when $k < 15$ even with large sample support. Next, the presence of eigenvalue spreading is considered and the same example is again examined with an intrinsic clutter velocity $\sigma_v = 1m/s$.

The ROC response for the PC method is displayed in Figure 4.11. Here it is evident that the PC technique is not able to obtain an optimum SINR within 3 dB loss until all ranks are greater than 21. Note that the actual noise-subspace eigenstructure is now greater than the theoretical efficient rank (19) because of eigenvalue spreading. On the other hand, the ROC for the MWF shown in Figure 4.12 again displays a vast improvement that covers the region of both lower sample support and significantly

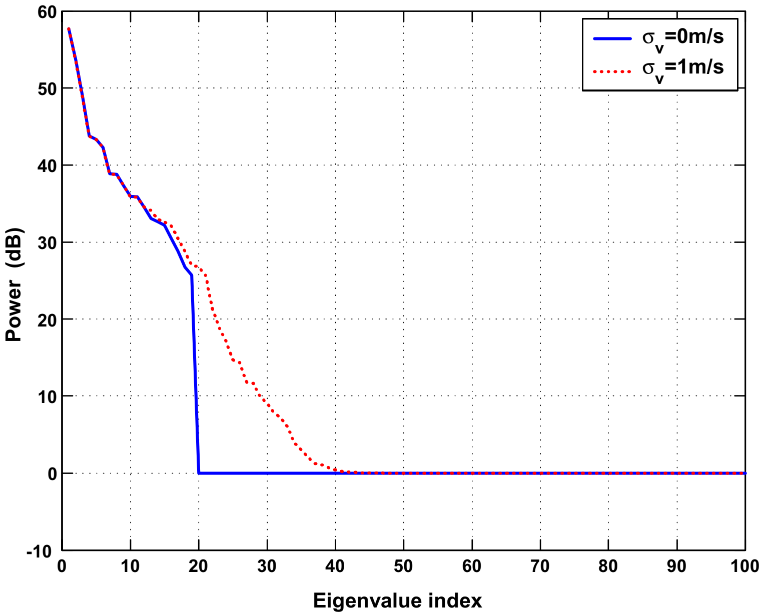

Figure 4.8: Eigenspectra of Clutter Covariance Matrix with Intrinsic Clutter Motion; Eigenvalue power (dB) vs. eigenvalue index; $N = 10$ elements; $M = 10$ pulses; Clutter-to-noise ratio, $CNR = 40$ dB; Clutter foldover $\beta = 1$; $\sigma_v$ = intrinsic clutter velocity

lower rank. The optimum SINR level is reached at a rank of 12, which is significantly lower than the dimension of the noise-subspace eigenstructure.

### 4.5.1 Summary

The MWF approach clearly has achieved significantly better supersession of the clutter and interference as compared to the PC approach in sample limited environments. While the PC approach requires full rank to capture the energy in the clutter space, the MWF optimizes the clutter rank with robust basis generated by the multistage decomposition. The convergence region of the MWF as a function of both rank and

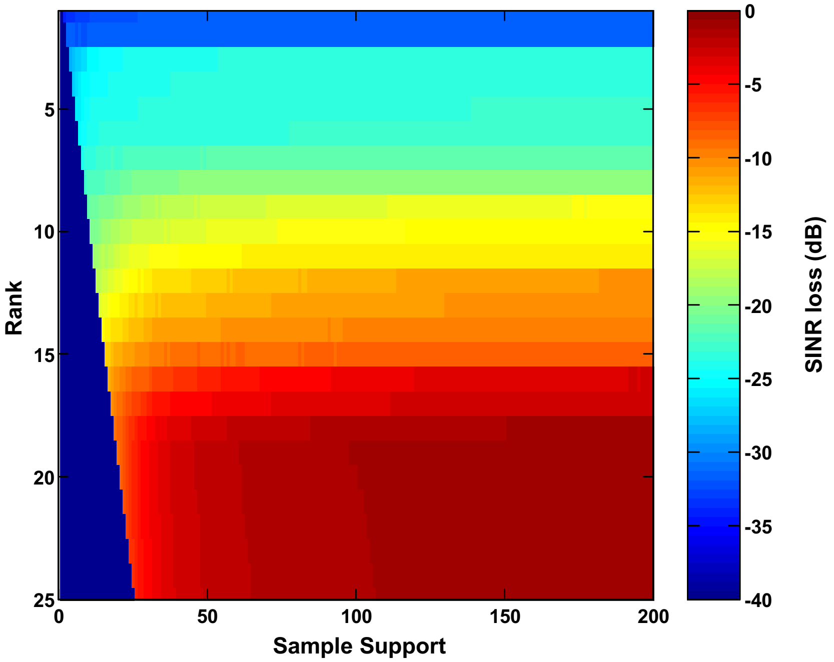

Figure 4.9: The Region of Convergence for Adaptivity (ROC) for Principal Components: SINR loss(dB) vs. rank and sample support; Intrinsic clutter velocity, $\sigma_v = 0$ m/s; $N = 10$ elements; $M = 10$ pulses; Clutter-to-noise ratio, $CNR = 40$ dB

sample support was demonstrated to be more robust, with significant SINR improvement as compared to the results obtained using principal components (PC) methods particularly in the presence of eigenvalue spreading. The robustness to eigenvalue spreading is also noteworthy considering the fact that the MWF does not even require an eigendecomposition of the observed-data covariance matrix.

Nevertheless, the impact of steering vector mismatch can still seriously degrade the MWF performance especially when the signal is included in the training data. In the next chapter, the effect of steering vector mismatch will be examined and a new MWF implementation using the well-known derivative constraints will be presented.

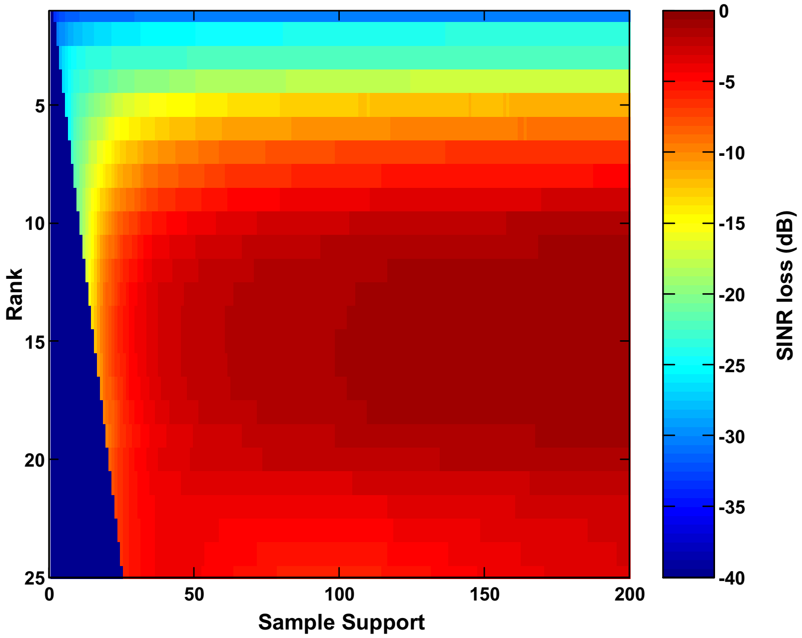

Figure 4.10: The Region of Convergence for Adaptivity (ROC) for Multistage Wiener Filter: SINR loss(dB) vs. rank and sample support; Intrinsic clutter velocity, $\sigma_v = 0$ m/s; $N = 10$ elements; $M = 10$ pulses; Clutter-to-noise ratio, $CNR = 40$ dB

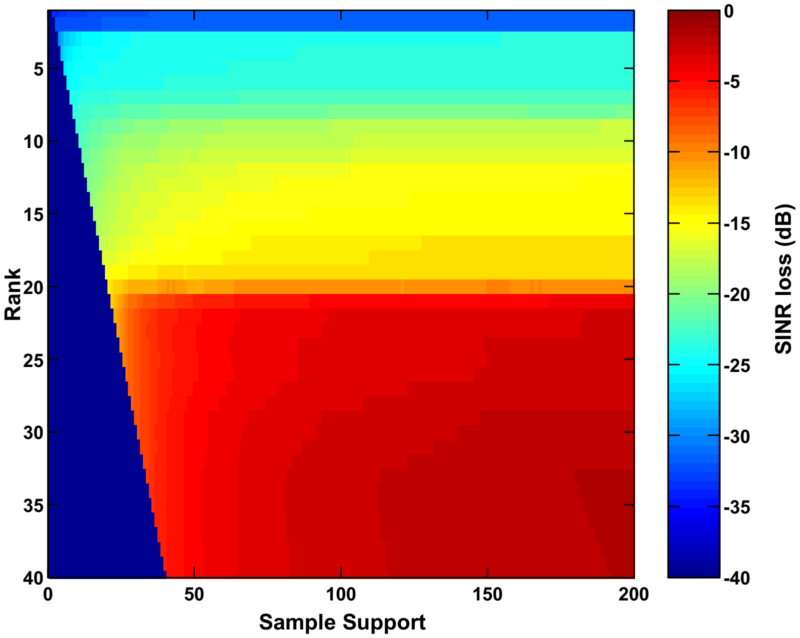

Figure 4.11: The Region of Convergence (ROC) for Principal Components with Intrinsic Clutter Motion: SINR loss (dB) vs. rank and sample support; Intrinsic clutter velocity, $\sigma_v = 1$ m/s; $N = 10$ elements; $M = 10$ pulses; Clutter-to-noise ratio, $CNR = 40$ dB

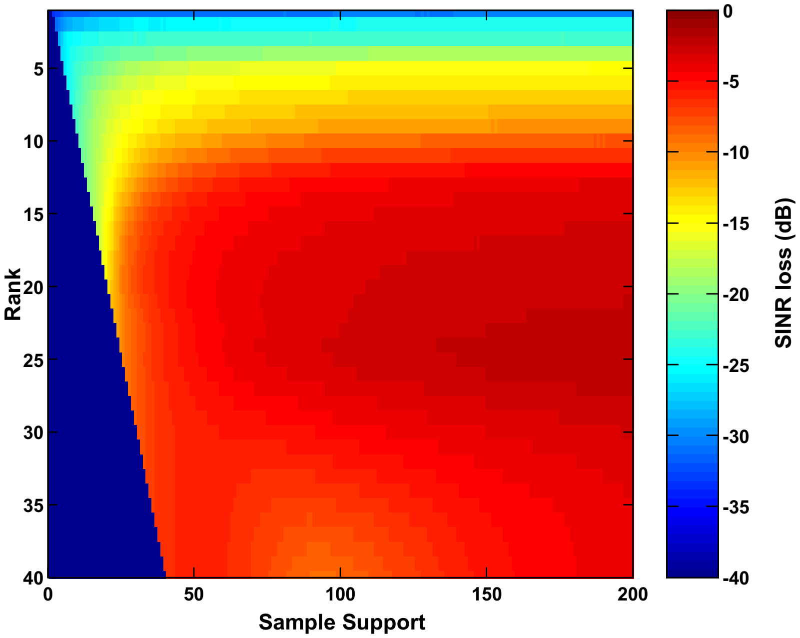

Figure 4.12: The Region of Convergence (ROC) for the Multistage Wiener Filter with Intrinsic Clutter Motion: SINR loss (dB) vs. rank and sample support; Intrinsic clutter velocity, $\sigma_v = 1$ m/s; $N = 10$ elements, $M = 10$ pulses; Clutter-to-noise ratio, $CNR = 40$ dB

# Chapter 5

# Multistage Wiener Filter (MWF) using Derivative Constraints for Steering Vector Mismatch

This chapter first examines the steering vector mismatch problem and presents an analysis of the signal-to-interference plus noise ratio (SINR) of the full-rank MVDR beamformer under steering vector errors. The analysis yields an explicit expression for the SINR in terms of the variance of the steering vector errors and related parameters affecting performance. This expected SINR loss is useful since the multistage Wiener filter (MWF) is a reduced-rank version of the MVDR and is expected to converge to the MVDR solution as the implemented rank is increased. It was known that techniques that are robust for estimation errors should also benefit in improving the steering vector perturbation errors, and the MWF is therefore also expected to be less susceptible to steering vector errors as compared to full-rank approaches [21]. Finally, a new MWF implementation using derivative constraints is presented in which the robustness for steering vector errors is examined and its major drawbacks are identified.

## 5.1 Problems with Steering Vector Mismatch

The MWF approach was analyzed under the assumption of ideal signal characteristics and an array configuration with a known desired steering vector. The adaptive weight is computed by minimizing the beamformer output power subject to a unity signal-response constraint in the beam steer direction. The results are optimum under the assumption of plane wave signals and ideal propagation medium. In practice, these ideal assumptions do not hold, and signal suppression can arise from causes such as beam steering angle errors, phase errors in the beamformer and multipath propagation. This problem is inherent in all approaches that require knowledge of the target steering vector. It has been shown that the effectiveness of these adaptive beamfomers can be destroyed if even a small mismatch arises [21], [34].

In radar and sonar systems, the steering vector mismatch problem can lead to increased false alarms from undernulled clutter, reverberations, and unexpected interferers. In sonar applications, the array is passive and the target signal is usually spread over all time samples. The assumed steering vector used as a reference for the sonar target may not actually equal the target response. The component of the true target vector different from the presumed vector is treated as interference and a small mismatch in the look direction can result in serious degradation in performance. The signal suppression problem is also observed in active array applications in radar where the target is confined to a single range cell. In these environments, the problem is particularly pronounced in a limited data support for a strong target signal, where the information provided by the target cell has a larger impact in the covariance matrix. Using a larger data set may however cause problems due to nonhomogeneous clutter effects. Commonly, the range cell under observation and some guard cells are excluded from the data set, and a new weight estimate is based on a so-called secondary training data set. This signal free training data set prevents the signal cancellation problem, however, it requires more samples to be utilized for the guard cells and also adds considerable computational complexity.

For airborne sidelooking radar working in a high-pulse repetition frequency (HPRF) mode, the range is highly ambiguous and the clutter return of each range bin is the superposition of many clutter echoes coming from different ranges with different depression angles. In these situation, steering vector mismatch errors not only have significant effects on clutter suppression performance, but also cause the adapted array patterns to suffer much distortion (high sidelobe and distorted mainlobe) which may result in an increase of false-alarm probability [70]. Furthermore, it is commonly believed that STAP has the potential to improve the performance of an AEW radar without the costly antenna refinements normally needed to reduce array sidelobes and clutter. Therefore, a practical STAP algorithm should be robust against various kinds of mismatch errors. Although theoretical performance prediction of many STAP algorithms is excellent, their practical performance is not so encouraging. Many algorithms suffer significant performance degradation when there exist mismatch errors and consequently the robustness of STAP algorithms to these problems is a very important issue.

## 5.2 Performance Analysis under Steering Vector Errors

In this section, the output signal-to-interference plus noise ratio (SINR) for the full-rank MVDR beamformer is computed analytically to assess the effect of pointing errors in the case of a known covariance matrix. The results are first analyzed for a simple case with white noise only and then extended with the additional presence of a single jammer. Finally, the average SINR loss for reduced rank approaches will be analyzed as a function of sample support and the MWF is expected to be less susceptible to steering vector errors as compared to full-rank approaches.

### 5.2.1 Full-Rank Approaches

A general Wiener filter structure for a full-rank MVDR algorithm is displayed in Figure 5.1, in which the upper branch represents the desired signal in the mainbeam direction and the lower branch consists of signals from all directions other than the mainbeam. The lower branch is also referred to as the sidelobe cancelling branch, which uses a standard blocking matrix to prevent any signal coming from the mainbeam direction. The output SINR will be computed under steering vector errors.

Assume that a desired signal in direction $\theta$ is present in addition to the interference, the covariance matrix can be represented as

$$\mathbf{R} = \sigma_s^2 \mathbf{s}(\theta)\mathbf{s}(\theta)^H + \mathbf{R}_i \tag{5.1}$$

where $\sigma_s^2$ is the signal power at each element, $\mathbf{s}(\theta)$ is the steering vector in direction $\theta$, and $\mathbf{R}_i$ is the interference plus noise covariance matrix. When the array points at

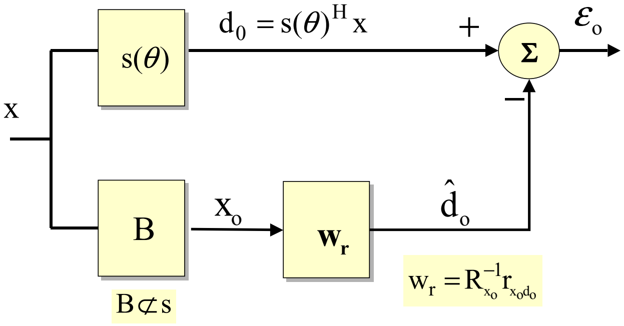

Figure 5.1: Wiener Filter Structure; $\mathbf{x}$ = array data input; $d_0$ = desired signal; $\mathbf{s}$ = mainbeam direction; $\mathbf{B} \notin \mathbf{s}$; $\mathbf{x}_0$ = observed data vector; $\mathbf{w}_r$ = Wiener filter weight; $\widehat{d_0}$ = estimate of desired signal; $\varepsilon_0$ = error signal

boresight and perfecting pointing accuracy is achieved ($\theta = 0°$), then no signal leaks into the sidelobe cancelling branch. However, with pointing error present ($\theta \neq 0°$), the signal will leak into the sidelobe cancelling branch and the leakage tends to cancel the signal output causing the output SINR to degrade.

The presumed steering vector $\widetilde{\mathbf{s}}$ due the pointing error may be different from the true steering vector $\mathbf{s}$ as follows

$$\mathbf{s} = \widetilde{\mathbf{s}}(1 + \Delta_v), \tag{5.2}$$

where the complex-valued "gain error" term $\Delta_v$ is assumed to be zero mean with variance of $\sigma_v^2$ and i.i.d. over the $N$ elements. The MVDR weight (2.10) can be expressed as

$$\mathbf{w}_{mvdr} = \frac{\mathbf{R}^{-1}\widetilde{\mathbf{s}}}{\widetilde{\mathbf{s}}^H\mathbf{R}^{-1}\widetilde{\mathbf{s}}}, \tag{5.3}$$

and the corresponding output SINR (2.6) is denoted by

$$SINR{=}\xi\frac{\left|\mathbf{w}^H\mathbf{s}\right|^2}{\mathbf{w}^H\mathbf{R}_i\mathbf{w}} = \xi\frac{\left|\widetilde{\mathbf{s}}^H\mathbf{R}^{-1}\mathbf{s}\right|^2}{\widetilde{\mathbf{s}}^H\mathbf{R}^{-1}\mathbf{R}_i\mathbf{R}^{-1}\widetilde{\mathbf{s}}} \tag{5.4}$$

where $\xi = \sigma_s^2/\sigma_o^2$ is the input signal-to-noise ratio (SNR) at each element, $\sigma_o^2$ is the noise variance, and $\mathbf{R}_i$ is again the interference plus noise covariance matrix. The degree to which perturbation and mismatch errors affect the output SINR depends upon the input SNR, and the optimum output SINR (2.9) repeated below

$$SINR_{opt} = \sigma_s^2 \mathbf{s}^H \mathbf{R}_i^{-1} \mathbf{s}. \tag{5.5}$$

If the latter term is a large quantity, even very small mismatch error can cause substantial degradation in performance. The following example for the case with white noise only illustrates this effect.

When the array operates with white noise only, the interference covariance matrix can be simply denoted

$$\mathbf{R}_i = \sigma_0^2 \mathbf{I}, \tag{5.6}$$

and the corresponding output SINR (5.4) can be expressed in the presence of steering vector mismatch

$$SINR{=}\xi \frac{\left|\mathbf{w}^H \mathbf{s}\right|^2}{\mathbf{w}^H \mathbf{w}} = \xi \frac{P_s}{P_n}, \tag{5.7}$$

where $P_s$ and $P_n$ correspond to signal power and noise power respectively [21]

$$P_s = \frac{\mathbf{s}^H \mathbf{s} \cos^2 \phi}{N(1 + \sin^2 \phi SINR_{opt})^2}, \tag{5.8}$$

$$P_n = \frac{1 + \sin^2 \phi SINR_{opt}(SINR_{opt} + 2)}{N(1 + \sin^2 \phi SINR_{opt})^2}, \tag{5.9}$$

where the error angle $\phi$ is measured between $\mathbf{s}$ and $\widetilde{\mathbf{s}}$

$$\phi \triangleq ang(\mathbf{s}, \widetilde{\mathbf{s}}) = \cos^{-1}\left(\frac{\left|\mathbf{s}^H \widetilde{\mathbf{s}}\right|}{\left|\mathbf{s}\right|, \left|\widetilde{\mathbf{s}}\right|}\right). \tag{5.10}$$

The level of SINR degradation clearly depends on the variation of angle $\phi$ from zero. Performance loss results both because the signal power term $P_s$ falls below its optimum value of $\mathbf{s}^H\mathbf{s}/N$, and because the noise power $P_n$ increases above $1/N$. The first problem is referred to as signal cancellation while the latter is termed increased noise response. When $SINR_{opt}$ is increased, both effects are further degraded. This can be shown by differentiating $P_s$ and $P_n$ with respect to $SINR_{opt}$. Inspection of (5.8) also reveals that negligible decrease in $P_s$ is observed if $\cos^2\phi \approx 1$ and if $\sin^2\phi \; SINR_{opt} \ll 1$. The increase in $P_n$ is insignificant if the latter condition holds and if $\sin^2\phi \; SINR_{opt}^2$ is not large.

When the array operates in the presence of white noise and a single jamming source with steering vector $\mathbf{s}_j$ and power $\sigma_j^2$, the interference covariance matrix can be expressed as

$$\mathbf{R}_i = \sigma_0^2\mathbf{I}+\sigma_j^2\mathbf{s}_j\mathbf{s}_j^H. \tag{5.11}$$

When the jamming angle is in the sidelobe of the array and $\mathbf{R}_i$ assumed to be known, the resulting mean value for SINR can be found [21]

$$E\{SINR\} \approx \frac{\xi N}{1+\xi^2 N(N-1)\sigma_v^2}, \tag{5.12}$$

where $\sigma_v^2$ was defined before (5.2). The expected SINR value can be normalized to the number of elements ($N$), and is expressed as

$$E\{SINR_n\} \approx \frac{\xi}{1+\xi^2 N(N-1)\sigma_v^2}. \tag{5.13}$$

This expression is quite accurate when the following conditions are satisfied $\xi \cdot N \gg 1$ and $\sigma_v^2 \ll 1$.

For example, the expected SINR loss (5.13) for a MVDR beamformer as a function of mismatch variance and input SNR (SNRi) is displayed in Figure 5.2. The example consists of a 10 element uniform linear array with half-wavelength element spacing.

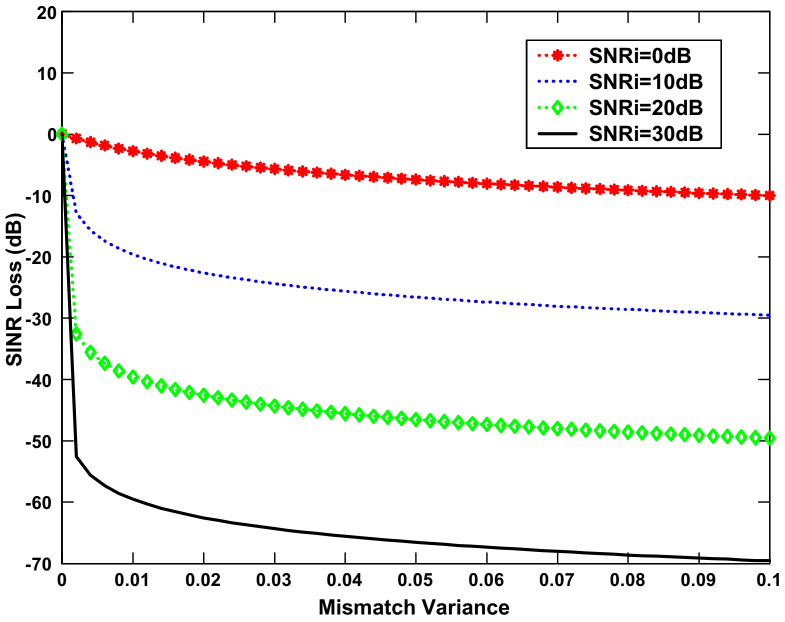

Figure 5.2: Theoretical Full-rank Mismatch Loss: SINR loss (dB) vs. steering vector mismatch variance; SINRi = Input SNR; Target azimuth angle = 0°; Number of elements, $N = 10$

Note that the output SINR loss is increased when the input SNR and mismatch variance $\sigma_v^2$ are increased.

### 5.2.2 Reduced Rank Approaches

The reduced-rank MWF is expected to be less sensitive to steering vector errors as compared to full-rank approaches. It was reasoned that sample estimation errors and steering vector mismatches have similar degrading effects on the SINR and the performance degradation for these two cases can be related through a simple model [21]. This relationship demonstrates that estimation errors due to finite sample effects are analogous to those observed with use of the wrong steering vectors when the covariance is known exactly. The result then implied that techniques known to be effective in overcoming the effects of estimation errors should also benefit in improving the steering vector perturbation errors. The MWF is therefore expected to be less susceptible to the steering vector errors and to the presence of the signal in the training set.

For the full-rank case, *Reed* has shown that a $2N$ sample support is required for a performance loss within 3 dB of the optimal array in the absence of the target signal and perturbation errors [52]. When the target is present in the data, Fieldman and Griffith [21] derived the approximation

$$E[SINR_{smi}] \approx \frac{N_s}{N_s + SINR_{opt}(N-1)} \tag{5.14}$$

where $N_s$ is the number of samples. From this expression, it follows that for performance within 3 dB of the optimum, $N_s \approx SINR_{opt}(N-1)$. The much slower convergence when the target is present is evident from comparing $SINR_{opt}(N-1)$ to $2N$.

For reduced rank approaches, the SINR loss as a function of sample support for the principal components (PC) was examined in [34]

$$E[SINR_{pc}] \approx 1 - \frac{1}{N_s}\zeta \tag{5.15}$$

where $\zeta$ is a chi-square random variable with $r$ degrees of freedom, and $r$ is also is the rank of the interference subspace. Consequently, for performance within 3 dB from its optimum, $N_s \approx 2r$. When the target is present in the data, the following result was found [34]

$$E[SINR_{pc}] \approx 1 - \frac{1}{N_s}(1 + SINR_{opt})r. \tag{5.16}$$

Therefore, the number of samples required for performance within 3 dB of the optimum can be approximated by $N_s \approx 2(1 + SINR_{opt})r$. Performance is degraded compared to the case of signal absent, but the PC approach converges at a much faster rate compared to the full-rank technique provided that the rank is smaller than the number of degrees of freedom.

The MWF has been shown to be more robust to the well-known PC method in terms of rank and sample support. Thus, the number of samples required for the PC approach can be considered as an upper limit for the MWF method. Consequently, the MWF approach is also expected to suffer a degradation loss, but its loss is much lower as compared to the full-rank method especially when the signal is present in the training set.

Many robust techniques have been proposed to overcome this sensitivity to pointing errors and to limit the degree of degradation. The approach in much of this work was to control the increase in the noise response $P_n$ in (5.9). The noise response can be bounded by either injecting white noise [13] (diagonal loading) or imposing an additional quadratic constraint [14], which is generally sub-optimum and requires additional computational burden. Other robust implementations such as derivative constraints were employed to preserve the signal power $P_s$ in (5.8). Derivative constraints help broaden the signal acceptance angle while preserving the beamformer's ability to reject interference from directions outside this acceptance angle.

## 5.3 Derivative Constraints Implementation

Derivative constraints impose a constraints band which flattens the spatial power response on the look direction in order to achieve robustness to pointing errors. The use of derivative constraints in a general linear constrained minimum variance (LCMV) beamformer has been investigated by Er and Cantoni [15] for a broadband system. Buckley and Griffiths [5] extended this application to an adaptive framework, implemented in a generalized sidelobe canceller (GSC) form of the LCMV beamformer. Derivative constraints are based on linear constraints which can be applied directly on the MWF structure. In this section a new MWF implementation with derivative constraints will be presented to improve robustness to direction errors.

### 5.3.1 Description

The response of a narrowband beamformer to a signal coming from a direction $\theta$ can be expressed as

$$y(\theta) = \mathbf{w}^H \mathbf{s}\left(\theta\right) \tag{5.17}$$

where $\mathbf{w}$ is the beamforming weight and $\mathbf{s}\left(\theta\right)$ is the steering vector. The conventional way to control the response shape is to directly constrain the derivatives of this beamformer response at a selected response point to be zero.

In general, a single directional constraint together with a number of derivative constraints are imposed on the polar response in the look direction. The single directional constraint is required to preserve the desired response in a direction $\theta_s$ to be unity

$$\mathbf{w}^H \mathbf{s}\left(\theta_s\right) = 1. \tag{5.18}$$

The first derivative of the response in the direction $\theta_s$ is constrained to be zero to ensure robustness to uncertainties in directions and mismatch problems

$$\frac{\partial}{\partial\theta} \mathbf{w}^H \mathbf{s}\left(\theta\right)|_{\theta=\theta_s} = 0 \tag{5.19}$$

Since a first derivative constraint is generally not efficient, additional derivatives may be added to enforce additional flatness on the response in the vicinity of $\theta_s$. The constraint system can be expressed as a linear relation of the adaptive weight $\mathbf{w}$

$$\mathbf{C}\mathbf{w} = \mathbf{f}, \tag{5.20}$$

where $\mathbf{f}$ is the desired response vector with constant elements corresponding to the constrained matrix $\mathbf{C}$. Each column of $\mathbf{C}$ and corresponding element of $\mathbf{f}$ represents a single constraint and each constraint uses up one degree of freedom in $\mathbf{w}$

$$\mathbf{C} = [\mathbf{s}(\theta)\ \dot{\mathbf{s}}(\theta)\ \ddot{\mathbf{s}}(\theta)...], \quad \mathbf{f} = [1,\ 0,\ 0, ...]^H \tag{5.21}$$

where $(\dot{})$ denotes differentiation with respect to $\theta$.

For a $0.5\lambda$ space uniform linear array with $N$ elements, the normalized $m$th-order derivative of a steering vector $\mathbf{s}$ is given

$$\mathbf{s}_m = \mathbf{d}^m \circ \mathbf{s}, \tag{5.22}$$

where $\mathbf{d}^m = \left[\left(\frac{-(N-1)}{2}\right)^m, \left(\frac{-(N-3)}{2}\right)^m, \ldots \left(\frac{(N-3)}{2}\right)^m, \left(\frac{(N-1)}{2}\right)^m\right]^T$,

where $\circ$ represents the Hadamard (i.e., element-wise) product operator and $(\cdot)^T$ represents the transpose operator. In this expression, the reference element is assumed at the center of the array and the $m$th-order derivative constraint is normalized to 1.

The linear constraint system can be applied to the MWF structure as shown in Figure 5.3 and the equivalent weight vector (2.14) can now be written

$$\mathbf{w} = \mathbf{C}\mathbf{w}_0 - \mathbf{C}_n\mathbf{w}_{m,} \tag{5.23}$$

where $\mathbf{w}_m$ is the adaptive reduced-rank Wiener weight, $\mathbf{w}_0$ is a non-adaptive weight vector spanned by columns of the constrained matrix $\mathbf{C}$, and $\mathbf{C}_n$ is a matrix whose

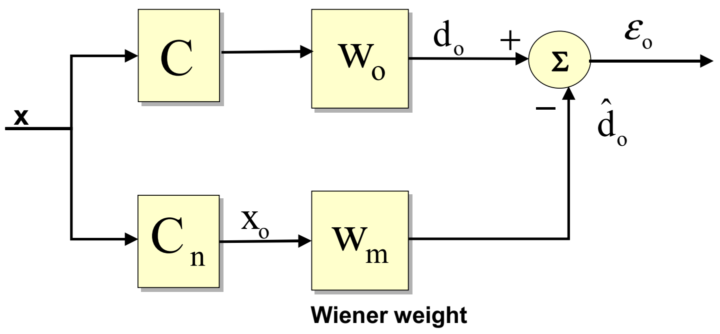

Figure 5.3: A Multistage Wiener Filter Structure with Linear Constraints; $\mathbf{x}$ = array input, $\mathbf{C}$ = linear constraints matrix; $\mathbf{C}_n \notin \mathbf{C}$; $d_0$ = desired signal and $\widehat{d_0}$ = its estimate; $\mathbf{x}_0$ = observed signal; $\epsilon_0$ = error signal; $\mathbf{w}_0$ = quiescent weight; $\mathbf{w}_m$ = adaptive Wiener filter weight

rows span the null space of $\mathbf{C}$. Applying the weight (5.23) into the constraint relation (5.20) and utilizing the orthogonal property of $\mathbf{C}$ and $\mathbf{C}_n$, the non-adaptive weight vector can be found

$$\mathbf{w}_0 = (\mathbf{C}^H\mathbf{C})^{-1}\mathbf{f}.$$

Essentially, the upper branch of Figure 5.3 can be expressed as

$$\mathbf{w_q} = \mathbf{C}\mathbf{w}_0 = \mathbf{C}(\mathbf{C}^H\mathbf{C})^{-1}\mathbf{f} \tag{5.24}$$

which represents a new quiescent weight in the MWF structure that satisfies the required linear constraints (5.20).

### 5.3.2 Numerical Results

This section presents some numerical results to examine performance degradation of full-rank and MWF approaches under steering vector errors for different levels of input signal-to-noise ratio (SNR). Additionally, the improvement of the new MWF implementation using a zero-plus-first-plus-second derivative constraint is demonstrated.

The array performance is evaluated by computing the SINR loss (3.34) which represents the output SINR normalized by the SNR obtained when using a matched filter in an interference-free environment. It can also be expressed as

$$SINR_{loss} = \frac{\left|\mathbf{w}^H \mathbf{s}\right|^2}{\mathbf{w}^H \mathbf{R}_i \mathbf{w}}, \tag{5.25}$$

where $\mathbf{R}_i$ is the ideal covariance matrix of interference plus noise and $\mathbf{w}$ is the adaptive weight vector derived from a mismatch unit steering vector. In this expression here, $\mathbf{s}$ is the unit normalized target steering vector pointing at the target direction. The results were simulated from 100 Monte Carlo trials.

First, the simulation implements a $N = 10$ element, half-wavelength spaced linear array. There is a jammer located at $-20^\circ$ and the jammer-to-noise ratio (JNR) is set to 50 dB above receive noise. The desired signal is at broadside and the SNR is 0 dB (element level). Figure 5.4 compares the MWF beampatterns of single constraint (sc) and derivative constraints (der1, der2) implementations using a rank of 1 and $2N$ sample support. The beampattern power was defined in 3.32. Note that the sc method refers to the standard MWF method with a unity signal-response constraint in the beam steer direction, while the der1 and der2 methods refer to zero-plus-first and zero-plus-first-plus-second derivative constraints respectively. As examined, these beam responses form a deep null at the jamming location as indicated by the vertical line. The beam response of the der1 method is observed to be very similar to the sc approach, thus additional derivative constraints are needed to widen the mainbeam. The mainbeam of the der2 method is more widened and robust to mismatch errors near the boresight while still suppressing jamming far

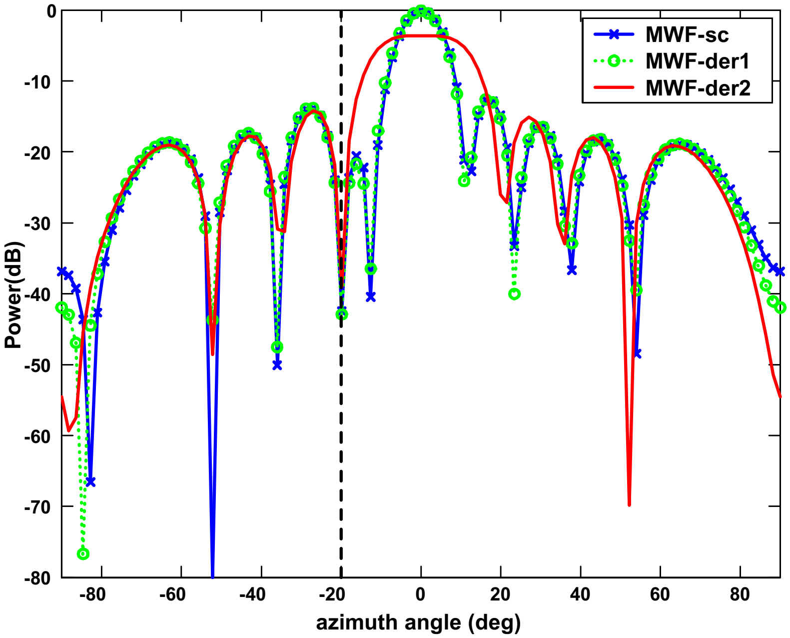

Figure 5.4: MWF Sample Beampatterns: Receiver output power (dB) vs. azimuth angle(deg); sc = single constraint; der1= 0-plus-1st derivative constraint; der2 = 0-plus-1st-and-2nd derivative constraints; Target is at boresight with $SNR = 0$ dB; Rank = 1; Number of elements, $N = 10$; Samples = $2N$; Jammer is at $-20$ degrees with $JNR = 50$ dB; Vertical line = jamming location

away from the broadside direction. The power loss at the boresight results since it only retains 7 degrees of freedoms (DOF) due to the constraints imposed on the zero, first and second derivatives. Derivative constraints impose linear constraints to broaden the mainbeam response near the desired look direction; however, these constraints can result in lower angle resolution and further loss in mainbeam jamming. The effect of mainbeam jamming will be discussed in Chapter 9. The number of derivatives implemented must be selected for trade-off between the angle resolution and robustness to directional mismatch.

Next, the same example is considered for a scenario for which the target is assumed

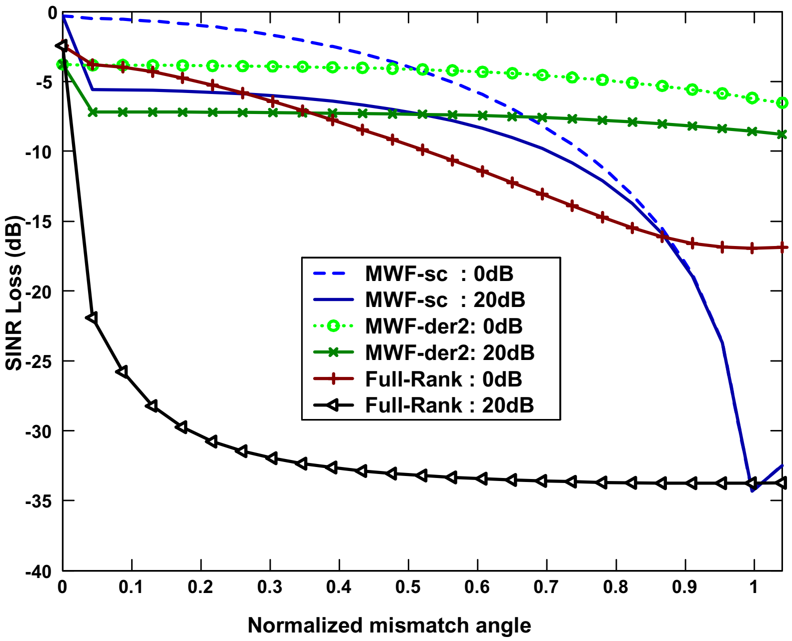

Figure 5.5: Mismatch Performance for Various Input Signal-to-noise ratios: SINR loss (dB) vs. mismatch angle normalized to $\frac{1}{2}BW_{nn}$; $BW_{nn}$(beamwidth null-to-null) $= \sin^{-1}(4/N)$; Target is located at boresight with $SNR = 0$ dB, which is present in all samples under steering vector errors; Input SNR = 0 dB or 20 dB; Rank = 1; Number of elements, $N = 10$; Samples = $2N$; Jammer is at $-20$ degrees with $JNR$ = 50 dB

present in all snapshots of the training data under steering vector errors. This is typical for a passive array application such as sonar or communication. Figure 5.5 compares the SINR loss performance for various input SNR levels as the steering vector mismatch angle error is varied. The example is again implemented with a rank of 1 and $2N$ sample support. The results are shown for full-rank methods and the MWF implementations of single constraint (sc) and second derivative constraints (der2). The mismatch error is normalized to half of the array null-to-null beamwidth ($BW_{nn}$), where $BW_{nn} = \sin^{-1}(4/N)$. For this example, $\frac{1}{2}BW_{nn} = 11.5°$. Due to

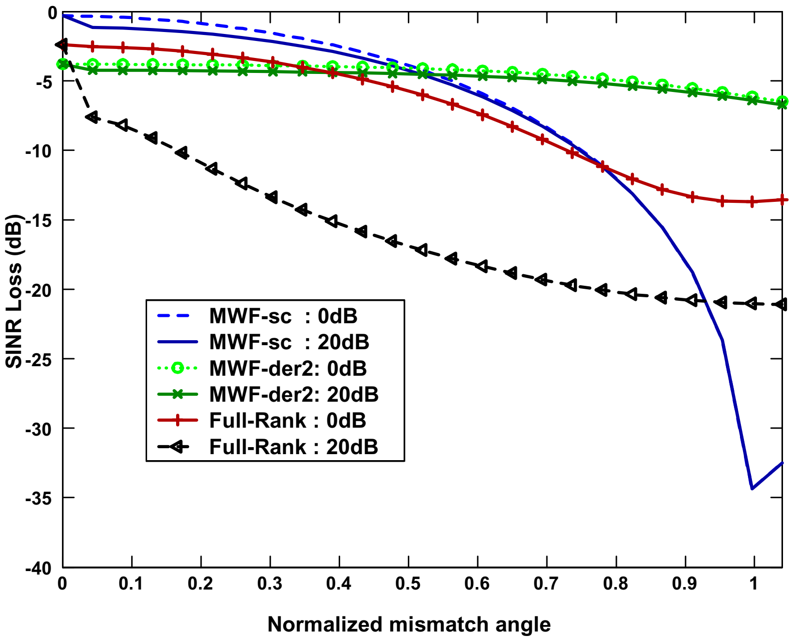

Figure 5.6: Mismatch Performance for Various Input Signal-to-noise ratios: SINR loss (dB) vs. mismatch angle normalized to $\frac{1}{2}BW_{nn}$; $BW_{nn}$(beamwidth null-to-null) $=$ $\sin^{-1}(4/N)$; Target is located at boresight with $SNR = 0$ dB, which is at a snapshot under steering vector errors; Input SNR $=$ 0 dB or 20 dB; Rank $=$ 1; Number of elements, $N = 10$; Samples $= 1N$; Jammer is at $-20$ degrees with $JNR = 50$ dB

the reduced DOF, as compared to the sc case, the der2 method suffers a slightly loss near the boresight but it performs much better as the error is larger. As expected, the full-rank performance degrades significantly as the error is larger especially at 20 dB SNR. It is observed that both of the MWF-sc and MWF-der2 implementations provide a more robust response especially with an increase in mismatch errors or SNR levels. It is expected as described previously because reduced-rank methods are more robust to sample estimation errors and therefore also less sensitive to steering vector errors as compared to full-rank approaches.

Finally, the same example is examined for an active array application such as a radar scenario for which the target is confined to a single snapshot of the training data under steering vector errors. The results are displayed in Figure 5.6 using a rank of 1 and $N$ sample support. The performance is improved and reduced-rank MWF approaches are observed less sensitive to the input SNR levels as compared to the case when the target is present in all samples. The same trend is again observed that the reduced-rank MWF approaches provide a markedly improved response especially with an increase in mismatch errors or SNR. The der2 method again performs much better as the error is larger. The performance of these approaches is however expected to degrade when more interference sources are present or limited samples are available as will be shown in the next chapter.

### 5.3.3 Summary

Derivative constraints can be easily implemented in the MWF structure, however these approaches also have some major drawbacks. It can only indirectly control the response and it is not evident how many derivatives are needed to achieve a specified level of response control over a given region. In addition, derivative constraints limit the number of degrees of freedom available and the array performance degrades from its optimum. Additionally, the beamformer output is generally complex valued in which both magnitude and phase response are constrained. The unnecessary phase constraint causes the beamformer response to be a function of the location of the spatial reference point used to define array elements positions [62]. This is undesirable since choosing a spatial reference point for the array should be for a notational convenience. A new technique employing covariance matrix tapers and quiescent pattern control in the MWF structure is introduced in the next chapter to overcome these problems.

# Chapter 6

# Multistage Wiener Filter (MWF) using CMTQ Constraints for Steering Vector Mismatch

In this chapter, a novel implementation of the multistage Wiener filter that exploits covariance matrix tapers and quiescent pattern control is presented to help alleviate problems with steering vector mismatch [48]. This combination is denoted CMTQ, which control the mainbeam and sidelobe patterns by utilizing a proper choice of taper on the data and imposing quadratic constraints on the array quiescent response. Covariance matrix tapers (CMT) are realized by the application of a conformal matrix taper to the original sample data. CMT is known robust to pattern distortion due to insufficient sample support and weight mismatch due to nonstationary interference. Quiescent pattern control (QPC) optimizes the quiescent weight for a highly directional response with low sidelobe levels in a white noise only environment. This enables the beamformer to maintain robust performance even before its response has adapted to the interferer. Both of these implementations are important for adaptive pattern control since real-world effects can lead to steering vector errors and significant degradation due to the mainbeam distortion and the antenna array sidelobe structure. It will be demonstrated that the use of CMTQ augmentation is very effective at mitigating the impact of steering vector mismatch while retaining the reduced rank and reduced sample support characteristics of the MWF. The new implementation shows its largest impact in terms of rank and sample support when compared to full-rank and the derivative-constrained MWF implementation. Furthermore, the new method is simple to implement and is more computational efficient as compared to previous approaches.

The chapter introduces the CMTQ implementation as applied to the MWF data domain structure, examines the associated performance loss, and presents some preliminary numerical results obtained with Monte Carlo simulations. In addition, an efficient implementation of quiescent pattern control (QPC) is presented exploiting the Taylor series approximation to estimate the solution at a significant reduction in computer operations.

## 6.1 Covariance Matrix Tapers (CMT)

The covariance matrix tapers (CMT) technique has been shown robust for controlling adapted pattern sidelobe and broadening the nulls in the directions of jammers [30], [67] in a full-rank beamformer. The new approach exploits CMT in the reduced-rank MWF structure to widen the mainbeam and the interference notch, providing robustness to adaptive patterns and steering vector errors.

Conventional tapers such as Chebyshev and Taylor window functions are universally used in practice for mainlobe distortion, sidelobe clutter and jammer suppression. The forms of these weights are usually chosen to suit the needs of a particular system. For example, a Chebyshev weighting is often desirable in linear array since it provides low, uniform sidelobes for the narrowest mainbeam [39]. It has been shown that such 'pre-weighting' is not effective for minimum variance adaptive arrays, since the adaptive algorithm modifies the weights to negate the effect of pre-weighting and provide a beampattern which is identical to that obtained without it [39]. Furthermore, the conventional tapered weight is optimal only when an exact knowledge of the interference statistics is known. As alluded to previously, in a non-homogeneous environment, there are many factors that induce errors into the covariance matrix estimation such as finite sample support, interference nonstationarities., and steering vector mismatch. The covariance matrix tapers (CMT) technique provides dynamic solutions to these problems while minimizing the loss incurred by conventional tapers.

### 6.1.1 Description

In general, the CMT procedure replaces the interference covariance matrix $\mathbf{R}_i$ in the adaptive weight equation (2.8) by a new tapered covariance matrix

$$\mathbf{R}_t = \mathbf{R}_i \circ \mathbf{T}, \tag{6.1}$$

where $\circ$ represents the *Hadamard* (i.e. element-wise) product operator and $\mathbf{T}$ is the positive semi-definite matrix of taper coefficients. The theories developed by Guerci [30] discussed the unifying theoretical concepts of a CMT that define some relevant properties for matrix $\mathbf{T}$. For example, the Schur Product and Eigenvalue Majorization theorems in [30] indicate that the conditional number of $\mathbf{R}_t$ improves when $\mathbf{T}$ is a real-valued positive definite matrix and $\mathbf{T}$ is simultaneously proportional to a correlation matrix.

More importantly, an optimum minimum variance beamformer can be satisfied when $\mathbf{T}$ is also associated with an auxiliary additive stochastic Gaussian process [30]. Thus, $\mathbf{T}$ can be associated with a vector stochastic process $\widetilde{\mathbf{z}}$, consisting of a deterministic boresight-aligned steering vector $\mathbf{e}$ where $\mathbf{e} = [1\ 1...1]^H$ and $\mathbf{T} = cov(\widetilde{\mathbf{z}}) = \mathbf{e}\mathbf{e}^H$. Notch widening and mainbeam broadening can be achieved by the introduction of a coherent phase "dithered" steering vector into $\mathbf{e}$. Specifically, assuming an $N$ element linear array with inter-element spacing $d/\lambda$ and boresight angle $\widetilde{\phi}$, then a vector process of $\mathbf{e}$ can be given by

$$\widetilde{\mathbf{e}} \triangleq \begin{bmatrix} 1 \\ \vdots \\ e^{j2\pi n \frac{d}{\lambda}\widetilde{\phi}} \\ \vdots \\ e^{j2\pi (N-1) \frac{d}{\lambda}\widetilde{\phi}} \end{bmatrix} \triangleq \begin{bmatrix} 1 \\ \vdots \\ e^{j2\pi n \widetilde{\omega}} \\ \vdots \\ e^{j2\pi (N-1) \widetilde{\omega}} \end{bmatrix}, \tag{6.2}$$

where $\widetilde{\omega}$ is a zero mean uniformly distributed R.V., such that $-\Delta \le \widetilde{\omega} \le \Delta$. Thus, to broaden a null or widen a mainbeam so that the fraction of beamspace it covers is $\gamma$, the $ij$ element of $\mathbf{T}$ can be calculated as

$$T_{MZ-1D} = E(\widetilde{e}\widetilde{e}^H) = \frac{sin(|i-j|\,\Delta)}{(|i-j|\,\Delta)} = sinc(|i-j|\,\gamma), \tag{6.3}$$

where the widening factor is defined as $\gamma = \Delta/\pi$. The choice of a uniform distribution of $\widetilde{\omega}$ is somewhat arbitrary and has been originally employed by Mailloux and Zatman [45], [67] for notch widening in the jamming direction. This taper matrix (6.3) is therefore also referred as the 1-D MZ taper. In this dissertation, the same concept will be extended to widening the mainbeam in the reduced-rank MWF structure and the net result is to introduce a coherent phase dither that imparts greater angular extent to a desired emitter, creating robustness in the adapted pattern without knowledge of the emitter locations.

A 2-D MZ taper can also be realized for STAP applications [30]

$$\mathbf{T}_{MZ-2D} = cov(\widetilde{e}_f) \otimes cov(\widetilde{e}_\theta) \in C^{NM}, \tag{6.4}$$

where $\widetilde{\mathbf{e}}_f \in C^M$ and $\widetilde{\mathbf{e}}_\theta \in C^N$ are mutually uncorrelated, coherent random Doppler frequency and angle phase dithers respectively

$$\widetilde{\mathbf{e}}_f \triangleq \begin{bmatrix} 1 \\ \vdots \\ e^{j2\pi m\widetilde{f}} \\ \vdots \\ e^{j2\pi(M-1)\widetilde{f}} \end{bmatrix} \text{ and } \widetilde{\mathbf{e}}_\theta \triangleq \begin{bmatrix} 1 \\ \vdots \\ e^{j2\pi n\widetilde{\theta}} \\ \vdots \\ e^{j2\pi(N-1)\widetilde{\theta}} \end{bmatrix}, \tag{6.5}$$

where $\widetilde{f}$ and $\widetilde{\theta}$ are uncorrelated zero mean and uniformly distributed random variables obeying $-\Delta_f \leq 2\pi\widetilde{f} \leq \Delta_f$, and $-\Delta_\theta \leq 2\pi\widetilde{\theta} \leq \Delta_{\theta.}$ As with 1-D adaptive array problems, nonstationarities in both angle and Doppler directions can result in poorer detection performance by the adaptive processor. A 2-D CMT can be exploited in the MWF structure for steering vector mismatch problems and nonstationarities. in the underlying clutter statistics.

An alternate expression for $\mathbf{T}_{MZ-2D}$ can be denoted as

$$\mathbf{T}_{MZ-2D} = (\mathbf{T}_f \otimes \mathbf{1}_{N\times N}) \circ (\mathbf{T}_\theta \otimes \mathbf{1}_{M\times M}), \tag{6.6}$$

where "$\circ$" is the *Hadamard* product operation, $\mathbf{1}_{N\times N}$ and $\mathbf{1}_{M\times M}$ are the $N\times N$ and $M\times M$ identity matrices, and from (6.3)

$$\mathbf{T}_f = sinc((m-n)\gamma_f), \tag{6.7}$$

$$\mathbf{T}_\theta = sinc((m-n)\gamma_\theta), \tag{6.8}$$

where $\gamma_f = \Delta_f/\pi$ and $\gamma_\theta = \Delta_\theta/\pi$.

Figure 6.1 and 6.2 display the amplitude distribution for the 1-D and 2-D MZ tapers using (6.3) and (6.6) respectively. The 1-D array consists of 10 elements with half-wavelength spacing, and the display represents uniform random modulation of angle-of-arrival over a sector with a small dither of $\gamma = 0.01$(rad). Note that the dither factor is also referred to as the widening factor. The 2-D array consists of 10 elements and 10 pulses in a CPI. The display represents uniform random modulation of over a sector with a small dither of $\gamma = 0.01$(rad) in both azimuth angle and Doppler frequency directions. Due to the implementation of the *sinc* function, the CMT matrices are observed to have a block-block Toeplitz structure with unity diagonal entries and strictly less than unity magnitude off diagonal elements. This effect is a conceptual generalization of diagonal loading although with diagonal loading only the noise eigenvalues below a fixed loading level are compressed thereby reducing the effects of randomly shaped noise eigenbeams [9], [36], [28]. Diagonal loading therefore may limit the detection of weak targets. In the CMT operation, the loading level however gradually decreases as the element index is larger.

For STAP applications, the estimation of the space-time covariance matrix $\mathbf{R}_i$ is accomplished by imposing a wide sense stationary (w.s.s.) assumption for the clutter statistics (space-time snapshots) with respect to range as described previously. For real terrain and urban environments, the spatial and temporal statistical distribution are nonhomogeneous and this assumption is generally not true. In addition, any large discrete clutter sources that are not adequately represented in the weight training process can lead to clutter-ridge null misplacement. Thus, the imperfections in the estimate of $\mathbf{R}_i$ can lead to undesirable adapted pattern artifacts and the use of CMT

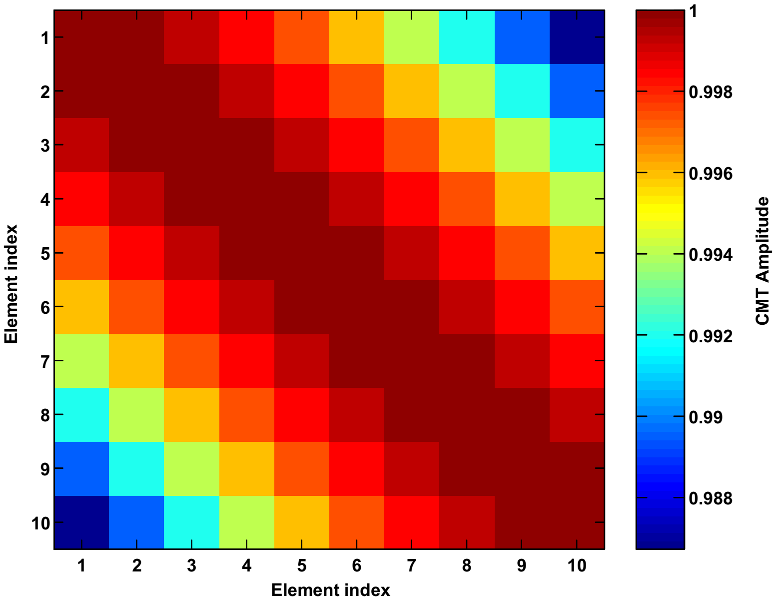

Figure 6.1: Amplitude Distribution for 1-D Mailloux-Zatman Taper: CMT amplitude vs. element index; Uniform random modulation of angle-of-arrival for a broadening factor of $\gamma = 0.01(\text{rad})$; Number of elements, $N = 10$; Note the block-block Toeplitz structure with all $1's$ on the diagonal axis

could also remedy these problems.

### 6.1.2 Data Domain Implementation

CMT can be employed in the data-domain structure by using the $Katri - Rao$ product "$\odot$", which relates to the $Hadamard$ product by [29], [51]

$$\mathbf{R} \circ \mathbf{T} = (\mathbf{x}\mathbf{x}^H) \circ (\mathbf{\Gamma}\mathbf{\Gamma}^H) = (\mathbf{x} \odot \mathbf{\Gamma})(\mathbf{x} \odot \mathbf{\Gamma})^H, \tag{6.9}$$

where $\mathbf{\Gamma} = sqrt(\mathbf{T})$ and the CMT data-domain vector is defined

$$\mathbf{x} \odot \ \mathbf{\Gamma} = [\mathbf{x}_1 \otimes \mathbf{\Gamma}_1 \ \ \mathbf{x}_2 \otimes \Gamma_2 \ \cdots \ \mathbf{x}_N \otimes \Gamma_N] \,, \tag{6.10}$$

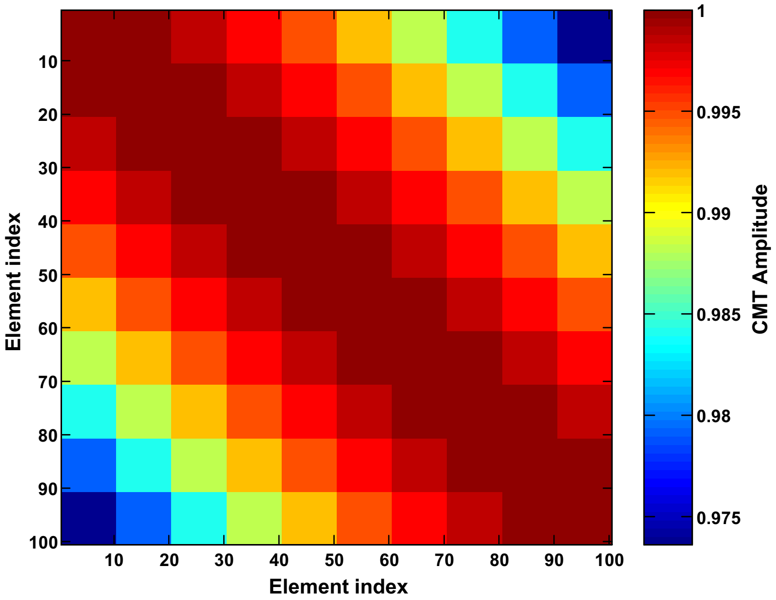

Figure 6.2: Amplitude Distribution for 2-D Mailloux-Zatman Taper: CMT amplitude vs. element index; Uniform random modulation for a broadening factor of $\gamma = 0.01$ (rad) in both azimuth angle and Doppler frequency directions; Number of elements, $N = 10$; Number of pulses, $M = 10$; Note the block-block Toeplitz structure with all $1's$ on the diagonal axis

where $\mathbf{x}_i$ is the $i^{th}$ row vector of $\mathbf{x}$, and $\Gamma_i$ corresponds to the $i^{th}$ column of $\mathbf{\Gamma}$. Note that $\mathbf{x}$ is a $N \times N_s$ sized data matrix with $N_s$ as the number of data samples. This results in an augmented data matrix that increases the original size of the data matrix from $N \times N_s$ to $N \times (N * N_s)$. For a large array and STAP processing, the adaptive weight computation can be very time consuming.

An alternative procedure is now presented, employing a direct $Hadamard$ product of the data input vector $\mathbf{x}$ and a tapering vector $\mathbf{t}$ obtained from the dominant subspace of the original matrix $\mathbf{T}$

$$\mathbf{T} = \mathbf{UVU}^H, \tag{6.11}$$

where $\mathbf{U}$ and $\mathbf{V}$ are the matrix of eigenvectors and corresponding eigenvalues respectively. Assume that $\mathbf{U}_D$ is the associated $N\times D$ matrix of signal-subspace eigenvectors and $\mathbf{V}_D$ is the $D\times D$ matrix containing square roots of the corresponding eigenvalues, the tapering vector $\mathbf{t}$ can be estimated as

$$\mathbf{t} = \mathbf{U}_D\mathbf{V}_D\mathbf{X}_r, \tag{6.12}$$

where $D$ is the number of significant eigenvalues and $\mathbf{X}_r$ denotes a $D\times N_s$ uniform random variable matrix. The resulting tapered data vector is then denoted

$$\mathbf{x}_t = \mathbf{x} \circ \mathbf{t}. \tag{6.13}$$

This operation is significantly faster since the rank of $\mathbf{T}$ is usually very low compared to the number of degrees of freedom. Use of dominant subspace approximation results in a very small SINR loss as compared with the Katri-Rao product operator, and the performance loss comparison will be examined in Section 6.3.1.

As with conventional tapers, the use of CMT increases the significant number of eigenvalues of the covariance matrix it is modifying, therefore requiring a higher rank in the MWF structure. In addition, it lacks direct control of mainlobe and sidelobe level. These shortcomings can be improved with quiescent pattern control (QPC) which imposes a robust quadratic constraint on the MWF quiescent response.

## 6.2 Quiescent Pattern Control (QPC)

Quiescent pattern control (QPC) produces a robust directional quiescent response with low sidelobe levels in a white noise environment, enabling the beamformer to maintain good performance even before its response has adapted to the interferer.

This will also make adaptive weight patterns more robust in limited sample-support and nonstationary environments, where steering vector mismatch may exist and directional interferers possess rapidly time-varying properties. A QPC strategy was developed in [56], however the solution requires iterative updates and intensive computation. The new approach imposes quadratic beampattern constraints in the MWF structure and exploits the Taylor series approximation [6] to estimate the solution at a significant reduction in computer operation.

### 6.2.1 Description

The goal is to estimate an optimum quiescent vector in the MWF structure that will restrict the mean square error ($MSE$) between a desired response $d(\theta)$ and array response over the mainlobe of interest ($\Delta\theta = \theta_u - \theta_l$) as follows

$$MSE_{mainlobe} = \frac{1}{\beta} \int_{\theta_l}^{\theta_u} \left| d(\theta) - \mathbf{w}^H \mathbf{s}(\theta) \right|^2 d\theta, \tag{6.14}$$

where $\beta$ is a scalar

$$\beta = \int_{\theta_l}^{\theta_u} d^*(\theta) d(\theta) d\theta, \tag{6.15}$$

The desired response $d(\theta)$ is normally chosen as the target steering vector. Assume that $0 \leq \epsilon \leq 1$ defines a normalized $MSE$ error over the mainlobe of interest in which the desired response is to be preserved.

This can be accomplished by minimizing the array response power over the sidelobe regions while limiting the deviation in the mainlobe of interest

$$\underset{\mathbf{w}}{Min}\ \mathbf{w}^H \mathbf{Q}_s \mathbf{w} \ \text{ Subject to } MSE_{mainlobe} \leq \epsilon, \tag{6.16}$$

where $\mathbf{Q}_s$ is a $N \times N$ -dimensional Hermitian matrix representing the outer product of steering vectors in the sidelobe region

$$\mathbf{Q}_s = \int_{\theta_1}^{\theta_2} g(\theta)\mathbf{s}(\theta)\mathbf{s}^H(\theta)d\theta + \int_{\theta_3}^{\theta_4} g(\theta)\mathbf{s}(\theta)\mathbf{s}^H(\theta)d\theta, \tag{6.17}$$

where $\{[\theta_1, \theta_2], [\theta_3, \theta_4]\}$ define the sidelobe regions. This matrix ($\mathbf{Q}_s$) is also premultiplied by a penalty function, which is chosen as $g(\theta) = |\theta - \theta_o|^p$, with $p$ as any real number defining its characteristic and $\theta_o$ as the target direction. This is used to weight the array response on the sidelobe region more heavily so that in the minimization of the integral of the weighted power response over the sidelobe region, robust sidelobe levels can be achieved. Note that $p$ is also referred to as the penalty function order. Typical good values of $p$ are ranged from 1 to 5.5, while $\epsilon$ are from 0.01 to 0.5.

The closed form solution to (6.16) is found by using Lagrange multipliers

$$\mathbf{w}_q = (\mathbf{Q}_s + \lambda\mathbf{Q}_m)^{-1}\mathbf{P}, \tag{6.18}$$

where $\mathbf{Q}_m$ is a $N \times N$ -dimensional Hermitian matrix given by the outer product of steering vectors in the mainlobe of interest

$$\mathbf{Q}_m = \frac{1}{\beta}\int_{\theta_l}^{\theta_u} \mathbf{s}(\theta)\mathbf{s}^H(\theta)d\theta, \tag{6.19}$$

and $\mathbf{P}$ is the correlation between the desired response $d(\theta)$ and steering vectors in the mainlobe of interest

$$\mathbf{P} = \frac{1}{\beta}\int_{\theta_l}^{\theta_u} d^*(\theta)\mathbf{s}^H(\theta)d\theta. \tag{6.20}$$

Note that $\lambda$ is the unknown Lagrange multiplier that has to be solved for numerically. The solution is usually computed with $\lambda$ initialized as a small positive value. Then, it must be recomputed iteratively with increasing values of $\lambda$ to satisfy (6.16).

### 6.2.2 Efficient Implementation

For a large array, the conventional QPC implementation can be computational intensive due to the required matrix inversion and weight iteration updates. By truncating the first two terms of its Taylor expansion about $\lambda = 0$ and assuming that $\lambda$ is small, the weight equation (6.18) can be expressed as

$$\mathbf{w}_q = (\mathbf{I} - \lambda \mathbf{Q}_m \mathbf{Q}_s^{-1})\widetilde{\mathbf{w}}_q \quad \text{where } \widetilde{\mathbf{w}}_q = \mathbf{Q}_s^{-1}\mathbf{P}, \tag{6.21}$$

where $\mathbf{I}$ is a $N \times N$ identity matrix. This equation can also be written as

$$\mathbf{w}_q = (\widetilde{\mathbf{w}}_\mathbf{q} - \lambda \mathbf{v}_q) \quad \text{where } \mathbf{v}_q = \mathbf{Q}_m \mathbf{Q}_s^{-1} \widetilde{\mathbf{w}}_q. \tag{6.22}$$

Since $\mathbf{Q}_m$, $\mathbf{Q}_s$, and $\widetilde{\mathbf{w}}_q$ can be computed directly, this expression can be substituted into the mainlobe constraint (6.16) to solve for $\lambda$. The solution yields a second order polynomial in $\lambda$ with a closed form expression for the roots

$$\begin{aligned} \lambda^2(A) + \lambda B + C &= 0 & (6.23)\\ \text{where } A &= \mathbf{v}_q^H \mathbf{Q}_m \mathbf{v}_q & (6.24)\\ B &= -2\,\mathrm{Re}(\mathbf{v}_q^H \mathbf{Q}_m \widetilde{\mathbf{w}}_\mathbf{q} - \mathbf{v}_q^H \mathbf{P}) & (6.25)\\ C &= 1 + \widetilde{\mathbf{w}}_q^H \mathbf{Q}_m \widetilde{\mathbf{w}}_\mathbf{q} - 2\,\mathrm{Re}(\widetilde{\mathbf{w}}_q^H \mathbf{P}) - \boldsymbol{\epsilon}. & (6.26) \end{aligned}$$

When $C > 0$, the roots are either two positive real values or a conjugate pair with real part $> 0$; $\lambda$ can be chosen as the smaller positive number in the first case, or the real part in the second case. Thus the optimum quiescent weight $\mathbf{w}_q$ can be directly obtained after $\lambda$ was found.

QPC provides robust control over the quiescent beamformer response with computational efficiency. Use of the CMTQ augmentation provides the steering vector mismatch robustness that we desire while retaining the reduced rank and reduced sample support characteristics of the MWF.

## 6.3 Numerical Results

Numerical results are now presented to demonstrate the selection of CMT and QPC parameters employed in the new approach. These parameters are selected to optimize the performance. Additionally, results from Monte Carlo simulations will be provided to evaluate the performance of the MWF weight response using the constraint implementations described previously.

### 6.3.1 Selection of CMT Parameters

As with conventional vector tapers, CMT introduces a mismatch loss that inevitably results in a SINR loss for large values of widening factor ($\gamma$). Thus $\gamma$ must be selected accordingly to minimize the SINR loss.

The extent of this loss can be determined by forming the ratio of the CMT realized $SINR_t$ to the optimal $SINR_{opt}$ (2.9)

$$SINR_{tloss} \overset{\circ}{=} \frac{SINR_t}{SINR_{opt}} = \frac{\left|\mathbf{w}_t^H \mathbf{s}\right|^2}{(\mathbf{s}^H \mathbf{R}_i^{-1} \mathbf{s})(\mathbf{w}_t^H \mathbf{R}_i \mathbf{w}_t)}, \tag{6.27}$$

where $\mathbf{w}_t$ is the MWF adaptive weight vector derived from the CMT tapered data. The results were simulated with 100 Monte Carlo trials.

First, Figure 6.3 examines the CMT tapering loss for the 1-D array example in Test Case 4, in which the signal geometry is displayed in Table 6.1. It consists of a $N = 10$ element uniform linear array. A sample of $2N$ and a rank of 5 were used. The desired signal is at the boresight and there are five jammers at -50, -40, -30, 35,

| **Signal** | **Location** | **SNR** |
|---|---|---|
| Desired | 0° | 0 dB |
| Jammer 1 | −50° | 50 dB |
| Jammer 2 | −40° | 50 dB |
| Jammer 3 | −30° | 50 dB |
| Jammer 4 | +35° | 50 dB |
| Jammer 5 | +60° | 50 dB |

Table 6.1: Signal Geometry for Test Case 4 (N=10 elements; Location is in azimuth angle)

and 60 degrees. All jammer-to-noise ratios (JNRs) are set to 50 dB and the desired level SNR is 0 dB above receive noise. When the widening factor $\gamma$ is increased from 0 to 0.05, the output SINR loss degrades as expected. This is due to an increase in eigenvalue spreading, and a rank larger than 5 in the MWF structure is required to optimize the performance. A larger $\gamma$ provides a wider mainbeam and more robust sidelobe levels, but incurs a larger loss as observed. Since the adaptive weight is employed with a finite number of samples, this loss also includes a loss due to sample estimation errors, which is about $-3$ dB for $2N$ of Gaussian sample support [52]. Nevertheless, the introduction of CMT with $\gamma$ less than 0.01 induces insignificant additional loss. For most examples in this dissertation, a value of $\gamma = 0.01$ will be selected.

For 1-D array examples, the CMT taper can be applied to the data using the Katri-Rao product operator. For a large array and STAP processing, this operation is very time consuming as described earlier, and the use of dominant subspace approximation of the CMT taper matrix is more desirable. The performance comparison is examined in Figure 6.4 using the 2-D array example with the environment defined in Table 4.3. The clutter-to-noise CNR is 40 dB per element and pulse, and its foldover factor $\beta$

is equal to 1. The linear array consists of $N = 10$ elements, half-wavelength element spacing, with $M = 10$ pulse CPI. A rank of 19 and a sample of $2MN$ were employed in the MWF approaches. The target is again located at the boresight (0°), with a normalized Doppler frequency of 0.25 and the associated signal-to-noise ratio (SNR) is 0 dB. A rank of 5 was used to approximate the dominant subspace of the CMT taper matrix. As examined, the use of the dominant subspace approximation results in very small SINR loss as compared with the Katri-Rao product operation. Note that a same value of the widening factor $\gamma$ was applied to both azimuth angle and Doppler frequency directions. When the widening factor $\gamma$ is increased from 0 to 0.2, the output SINR loss degrades as expected. As observed, the introduction of CMT with $\gamma$ less than 0.01 induces insignificant additional loss. For most examples in this dissertation, a value of $\gamma = 0.01$ will be selected for 2-D array examples.

Finally, Figure 6.5 displays the MWF sample beampatterns for the 1-D example in Test case 4, in which the implementation of single constraint (sc), derivative constraints (der2), and covariance matrix tapers (cmt) are evaluated using a sample of $2N$. Note that the sc method refers to the standard MWF method with a single constraint on the signal direction, and the der2 method implies the MWF using zero-plus-first-plus-second derivative constraints. The cmt approach was implemented with a small dither of $\gamma = 0.01$. Both the sc and der2 approaches are implemented with a rank of 5 due to the presence of five jammers. The der2 method has a wider mainbeam but suffers a loss close to the boresight due to the reduced degrees of freedom. The cmt approach requires a rank of 8, since the tapering process induces eigenvalue spreading into the data. The resulting response is evidently more robust with a moderate beamwidth, little loss in SINR, reduced sidelobe levels and markedly

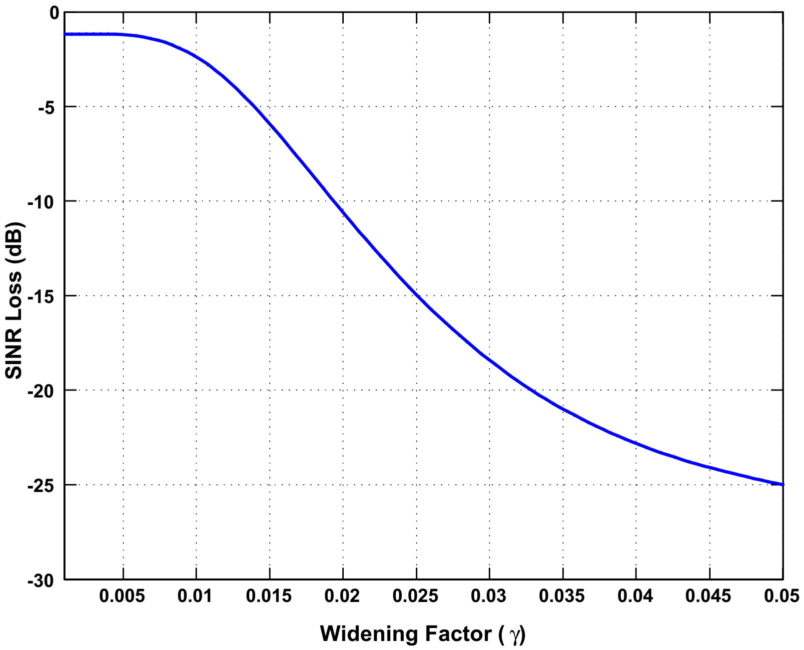

Figure 6.3: CMT Tapering Loss for 1-D Array: SINR loss (dB) vs. widening factor $\gamma$; Number of elements, $N = 10$; Samples $= 2N$; Rank $= 5$; Five jammers are at -50, -40, -30, 35 and 60 degrees; Jammer-to-noise ratio (JNR) = 50 dB each

widened nulls at all jamming directions.

### 6.3.2 Selection of QPC Parameters

Quiescent pattern control (QPC) requires selection of a desired beamwidth ($\Delta\theta$), a MSE deviation ($\epsilon$), and penalty function order ($p$). The desired beamwidth ($\Delta\theta$) represents a mainlobe of interest over which the quiescent response is to be preserved (6.14), and the MSE deviation ($\epsilon$) denotes a maximum deviation between a desired response and array response in the same beamwidth (6.16). The penalty function (6.17) provides a measure of the distance between the target azimuth angle and sidelobe azimuth angles. The penalty function order ($p$) defines the characteristic

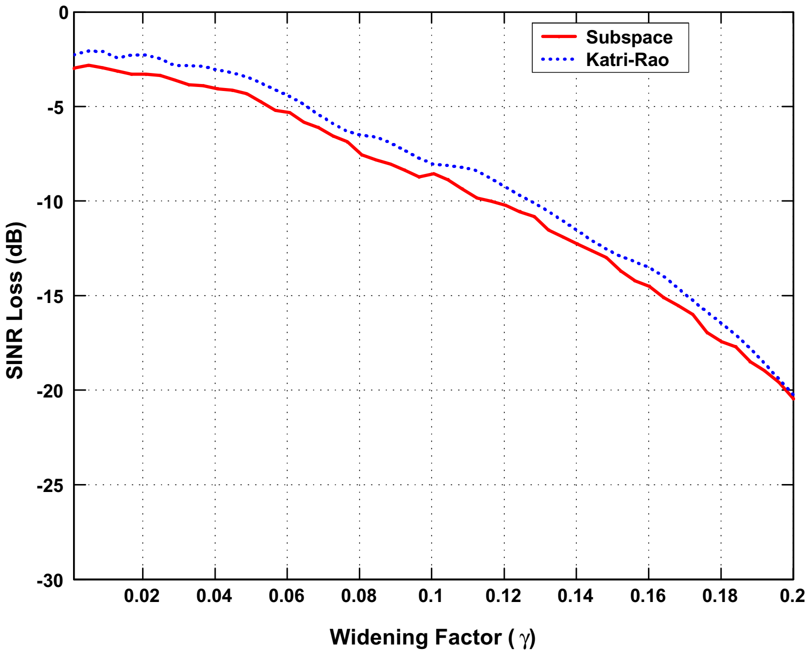

Figure 6.4: CMT Tapering Loss for 2-D Array: SINR loss (dB) vs. widening factor $\gamma$; Number of elements, $N = 10$; Number of pulses, $M = 10$; Samples = $2MN$; Rank = 19; “Katri-Rao” denotes that CMT applied to data using Katri-Rao operator; “Subspace” denotes that CMT applied using the dominant suspace approximation of the taper matrix

of the penalty function, which weights the array response further away from the mainlobe more heavily so that very low sidelobes can be achieved at the trade-off of a wider mainbeam. These parameters do not depend on the data and can be pre-selected as desired. In this section, we will examine the effect of varying these parameters.

Figure 6.6 displays QPC quiescent beampatterns (6.18) using a desired beamwidth of $\Delta\theta = 10°$ and a MSE deviation of $\epsilon = .01$. The response were obtained with the penalty function order ($p$) varied from 1.5 to 5.5 for sidelobe control. The example employs a 10 element linear array with half-wavelength spacing. There is a desired

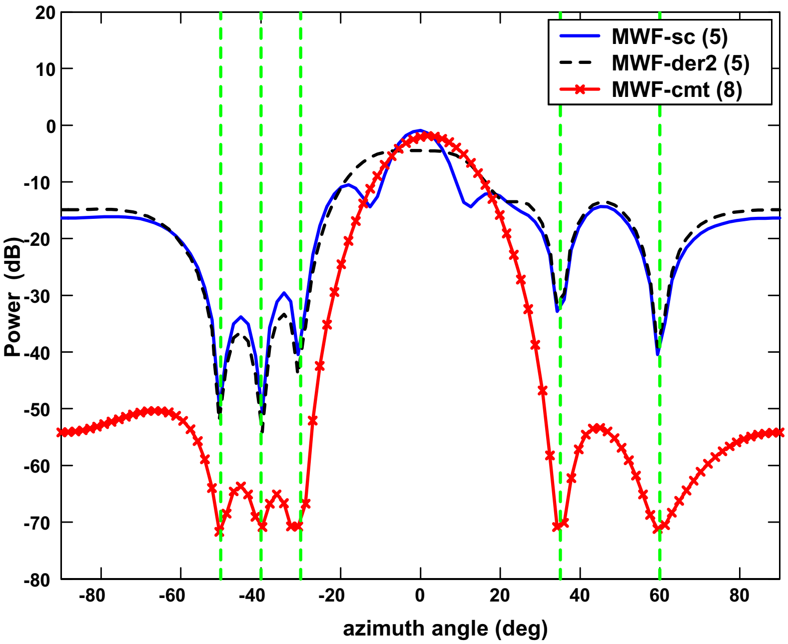

Figure 6.5: MWF Sample Beampatterns (Test Case 4): Receiver output power (dB) vs. azimuth angle (deg); sc = single constraint; der2 = 0-plus-1st-plus-2nd derivative constraints; cmt = covariance matrix tapers; Number inside parenthesis = rank; Number of elements, $N = 10$; Samples = $2N$; CMT widening factor, $\gamma = 0.01$; Five jammers are at -50, -40, -30, 35 and 60 degrees; Jammer-to-noise ratio (JNR) = 50 dB each

signal at boresight and the desired SNR is 0 dB (element level). Note that the standard quiescent beam is also shown for comparison. As the penalty function order $p$ is increased, the corresponding beamwidth is wider with more robustness in sidelobe level. As observed, the response with $p = 5.5$ is the most desirable beampattern for our application and will be employed in most of our simulations.

Next, these QPC beampatterns are now generated with beamwidth $\Delta\theta$ varied from $5^\circ$ to $20^\circ$ as shown in Figure 6.7, in which a penalty function order of $p = 5.5$ and a MSE deviation of $\epsilon = .01$ are chosen. As recalled, these beampatterns

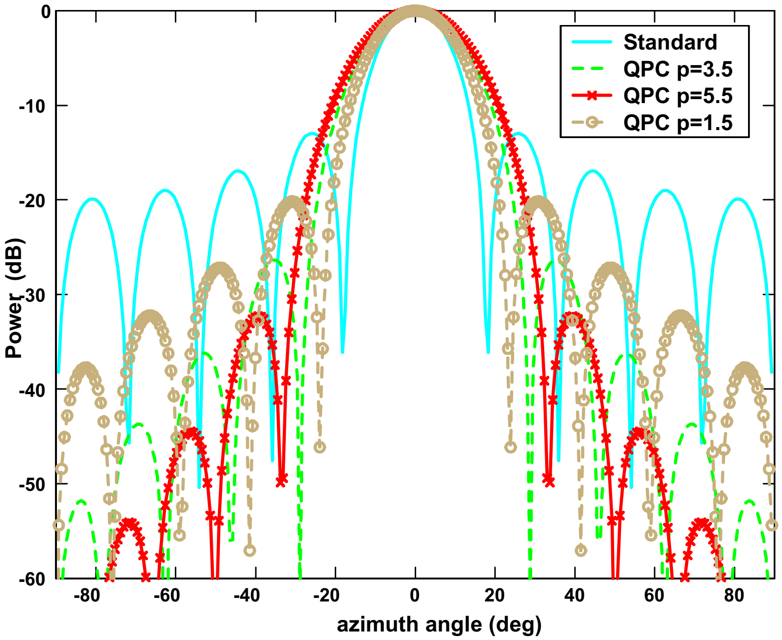

Figure 6.6: QPC Quiescent Beampatterns and Sidelobe Variation: Beampattern power (dB) vs azimuth angle (deg); A standard quiescent beam is compared with QPC quiescent beams; Penalty function order $p$ is varied from 1.5 to 5.5; Beamwidth, $\Delta\theta = 10°$; MSE deviation, $\epsilon = .01$; Number of elements, $N = 10$; Note when $p = 5.5$, QPC beam has lowest sidelobe level

are constrained on a MSE deviation between a desired response and array response over a beamwidth of interest ($\Delta\theta$) (6.14). In this example, the desired response is chosen as the target steering vector, which has a beamwidth of roughly 18° for a 10-element linear array. As a result, a large $\Delta\theta$ close to this value will cause the resulting beams to match closely to the target steering vector, which may also exhibit undesirable sidelobe levels. These can be observed for the beampatterns with beamwidth of 15° and 20°. On the other hand, beampatterns with smaller constrained beamwidth (5° and 10°) are matched to the target steering vector over a smaller angular region around the boresight. The penalty function has more freedom

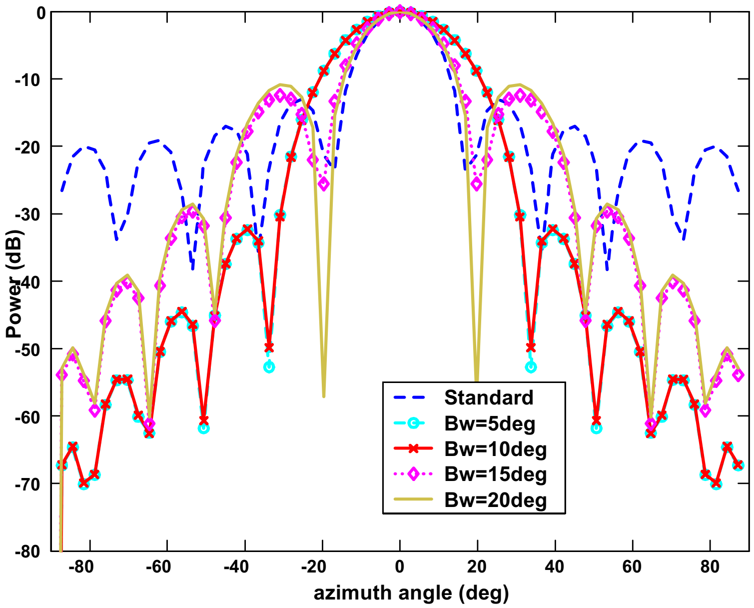

Figure 6.7: QPC Quiescent Beampatterns and Beamwidth Variation: Beampattern power (dB) vs azimuth angle (deg); A standard quiescent beam is compared with QPC beams; Beamwidth, $\Delta\theta$ is varied from 5° to 20°; Penalty function order, $p$ = 5.5; MSE deviation, $\epsilon = .01$; Number of elements, $N = 10$

to suppress the sidelobe levels which become remarkably low, as observed. This also results in a wider effective beamwidth, robust for steering vector errors. A rule of thumb is to limit the constrained beamwidth $\Delta\theta$ to 1/2 of the array beamwidth; consequently, a QPC beampattern with a beamwidth of 10° will be used in most of our simulations.

Figure 6.8 displays the MWF sample beampatterns for the same environment, comparing the implementation of single constraint (sc), derivative constraints (der2), covariance matrix tapers (CMT), quiescent pattern control (QPC), and hybrid CMTQ (cmtq) implementations using a rank of 5 and a sample support of $2N$. The qpc approach employs a QPC beam with a desired beamwidth of $\Delta\theta = 10°$, a MSE deviation of $\epsilon = .01$, and a penalty function order of $p = 5.5$. The CMT utilizes a widening factor of $\gamma = 0.01$. As compared to sc methods, the der2 method has a wider mainbeam. It however suffers a loss close to the boresight due to the reduced degrees of freedom (DOF). The cmt approach was implemented with the same rank of 5, therefore it provides a similar beamwidth as the sc method. Note that a higher rank would result in a more robust response as discussed previously in Figure 6.5. The cmt response is however still observed with more robust sidelobe levels and wider notches at all jamming directions. The qpc method has a wider mainbeam as compared to the sc approach. The best performance is the cmtq method which forms a moderate beamwidth with clearly robust sidelobe levels and wider notches at all jamming locations.

## 6.4 Summary

This chapter has introduced a robust steering vector mismatch implementation for the multistage Wiener filter (MWF) using covariance matrix tapers (CMT) and quiescent pattern control (QPC). CMT is naturally broadening the mainbeam while also adding robustness by widening the notches in the direction of clutter and interference. CMT was traditionally implemented by applying a conformal taper matrix to the original sample covariance. CMT can be employed in the MWF data-domain structure by using the $Katri - Rao$ product which is computational intensive for STAP applications. An efficient CMT implementation was presented by extracting a dominant subspace of the CMT matrix. QPC employs a constrained quiescent beam pattern in the MWF structure, and is based on a set of inequality constraints between the array response and a desired response over a given angular region. This

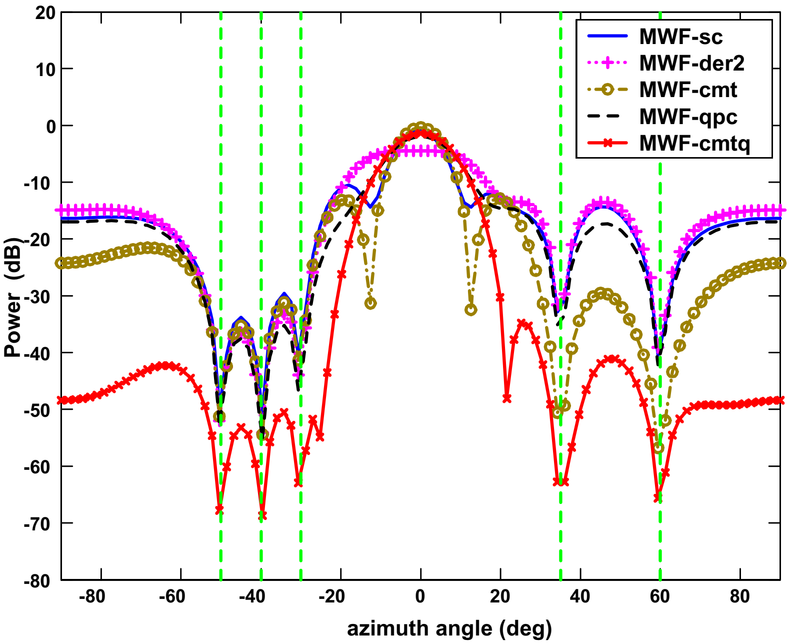

Figure 6.8: MWF Sample Beampatterns (Test Case 4): Receiver output power (dB) vs. azimuth angle (deg); Number of samples, $N = 10$; Samples $= 2N$; sc = single constraint; der2 = 0-plus-1st-plus-2nd derivatives; cmt = covariance matrix tapers; qpc=quiescent pattern control; cmtq=combination of cmt and qpc; Rank = 5; CMTQ parameters: beamwidth $\Delta\theta = 10^\circ$, mse deviation $\epsilon = .01$, penalty function order $p = 5.5$, widening factor $\gamma = 0.01$; The dotted vertical lines indicate jamming locations

helps preserve a desired mainlobe width while producing a highly adaptive pattern in white noise environments, therefore ensuring that the beamformer is robust even before its response has adapted to a colored noise environment. An efficient QPC implementation was also introduced using the Taylor series approximation. While minimizing additional complexity for real-time processing, the new QPC implementation helps preserve and improve the beamformer response at a reduced rank. Use of the CMT and QPC augmentation is denoted as CMTQ, which forms a robust beam response that we desire while retaining the reduced rank and reduced sample support characteristics of the MWF. The robustness of this approach in terms of SINR loss as a function of rank, sample support, and steering vector errors will be the focus of the next chapter.

# Chapter 7

# Performance Evaluation using Simulation Data

In this chapter, results from Monte Carlo simulations will be provided to examine the performance of the MWF with CMTQ implementation in both spatial-only (1-D) and STAP (2-D) applications. Its performance will be evaluated with the standard MWF, derivative constraint MWF, and full-rank approaches. The robustness of the new approach in terms of SINR loss will be examined as the steering vector error is varied. Additionally, the rank performance will be evaluated in the presence of steering vector mismatch. More importantly, the SINR loss is also assessed as a function of both the effective rank and the amount of training data under steering vector errors. This SINR loss is called the region of convergence for adaptivity (ROC) which provides an informative way to analyze the potential benefits of the new approach for reduced rank processing as a function of finite sample support. These results are important since the number of training samples is limited in severely nonhomogeneous environments as described before. The ROC performance of the new implementation will be demonstrated to be remarkably more robust as compared with the standard MWF and derivative constraint MWF methods under steering vector errors.

## 7.1 Performance Metric

A metric used to evaluate the array performance under steering vector errors is the SINR loss (5.25) which is repeated below for convenience

$$SINR_{loss} = \frac{\left|\mathbf{w}^H \mathbf{s}\right|^2}{\mathbf{w}^H \mathbf{R}_i \mathbf{w}} \tag{7.1}$$

where $\mathbf{R}_i$ is the ideal covariance matrix of interference plus noise and $\mathbf{w}$ is the adaptive weight vector derived from a mismatched unit steering vector. In this expression, $\mathbf{s}$ is the unit normalized target steering vector pointing at the target direction. Note that for the cmtq approach, it is assumed that $\mathbf{s}$ is matched to the constrained quiescent beam used in transmit. When implemented, the cmtq approach is also assumed to employ a QPC beam with a desired beamwidth of $\Delta\theta = 10°$, a MSE deviation of $\epsilon = .01$, a penalty function order of $p = 5.5$, and a CMT widening factor of $\gamma = 0.01$.

As a baseline, Table 7.1 and 7.2 summarize simulation parameters for the 1-D and 2-D examples respectively. For the 1-D example, the mismatch target is assumed present in all samples of the training data under steering vector errors, which represents a worst case scenario as typical for passive array applications. In the 2-D example, the mismatch target is assumed to confine to the center snapshot of the training data. As described before, the target presence in a single snapshot is typical for radar applications. The results were simulated with 100 Monte Carlo trials.

| **Signal** | **Location** | **SNR** |
|---|---|---|
| Desired | $0°$ | 0 dB |
| Jammer 1 | $-50°$ | 50 dB |
| Jammer 2 | $-40°$ | 50 dB |
| Jammer 3 | $-30°$ | 50 dB |
| Jammer 4 | $+35°$ | 50 dB |
| Jammer 5 | $+60°$ | 50 dB |

Table 7.1: Signal Geometry for Test Case 5 (N=10 elements; Location is in azimuth angle)

| **Signal** |
|---|
| Desired Signal at 0° |
| Desired Signal SNR = 0 dB |
| |
| **Jamming** |
| $-35°$, JNR= 40 dB |
| 30°, JNR = 30 dB |
| |
| **Clutter** |
| Clutter-to-noise (CNR = 40 dB) |
| No. of Clutter Foldover ($\beta = 1$) |
| Velocity misalignment angle = 0° |
| Intrinsic Clutter Velocity ($\sigma_v = 1\ m/s$) |

Table 7.2: Signal Geometry for Test Case 6 (N=10 elements, M=10 pulses; Clutter return from each range sample is the superposition of all clutter patches evenly distributed in all azimuth angles)

## 7.2 SINR Performance

The first example consists of a $N = 10$ element uniform linear array as shown for Test Case 5 in Table 7.1. Five jammers are present at -50, -40, -30, 35, and 60 degrees. All jammer-to-noise ratios (JNR) are set to 50 dB and the desired SNR is 0 dB above receive noise. The MWF weight response of single constraint (sc), derivative constraints (der2), and hybrid CMTQ (cmtq) implementations are displayed in Figure 7.1. Note that a rank of 5 and a sample support of $2N$ are implemented. The sc method refers to the standard MWF method with a single constraint on the signal direction and the der2 method implies the MWF using zero-plus-first-plus-second derivative constraints. The robustness of the cmtq beampattern is observed to have much lower sidelobe levels and wider notches at all jamming directions as compared to both of the sc and der2 approaches.

The performance of these approaches as a function of rank is shown in Figure 7.2, using $2N$ samples. Additionally, the full-rank MVDR is also considered as a benchmark, which is expected to result in a loss of 3 dB for a $2N$ Gaussian sample support [7]. Due to the presence of five jammers, all MWF approaches reach the maximum level at a rank of 5 and exceed full-rank performance. The der2 method has a poorer performance, since it only retains 7 DOF due to the constraints imposed on the zero, first and second derivatives. As observed, the cmtq method outperforms all other approaches for all ranks less than 5. While the sc method converges to full-rank (which is worse) as the rank is increased, the cmtq approach remains essentially at its peak level. Figure 7.3 displays the same simulation when a steering vector error of $6^\circ$ is introduced into the environment. Due to the mismatch error and the presence of the target in the data, the full-rank solution suffers an additional 7 dB

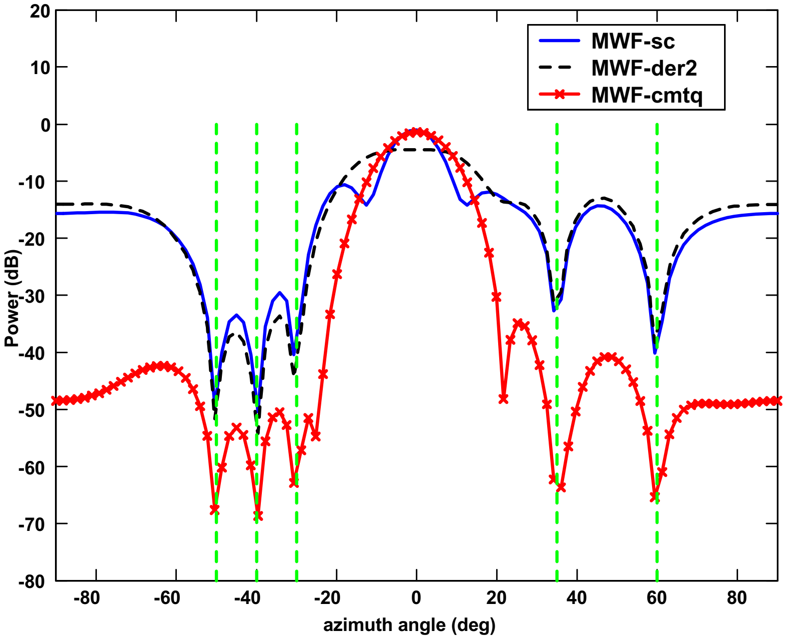

Figure 7.1: MWF Sample Beampatterns for 1-D Array (Test Case 5): Receiver output power (dB) vs. azimuth angle (deg); sc=single constraint; der2 = 0-plus-1st-plus-2nd derivatives; cmtq=combination of CMT and QPC; Number of elements, $N = 10$; Samples $= 2N$; Rank $= 5$; CMTQ parameters: beamwidth $\Delta\theta = 10°$, mse deviation $\epsilon = .01$, penalty function order $p = 5.5$, widening factor $(\gamma) = 0.01$; The dotted vertical lines indicate jammer locations

SINR loss. The sc method again converges to the full-rank solution, which hinders its performance even at the lower ranks. The der2 method is a slight improvement over the sc approach. The cmtq, on the other hand, is a significant improvement and provides a much more robust region of rank with which to implement the processor.

For completeness, the mismatch loss performance of these approaches is examined in Figure 7.4, in which the SINR loss is computed as the steering mismatch error is varied, using a sample of $2N$ and a rank of 5. The mismatch error is normalized to half of the array null-to-null bandwidth $BW_{nn}$, where $BW_{nn} = \sin^{-1}(4/N)$, which is

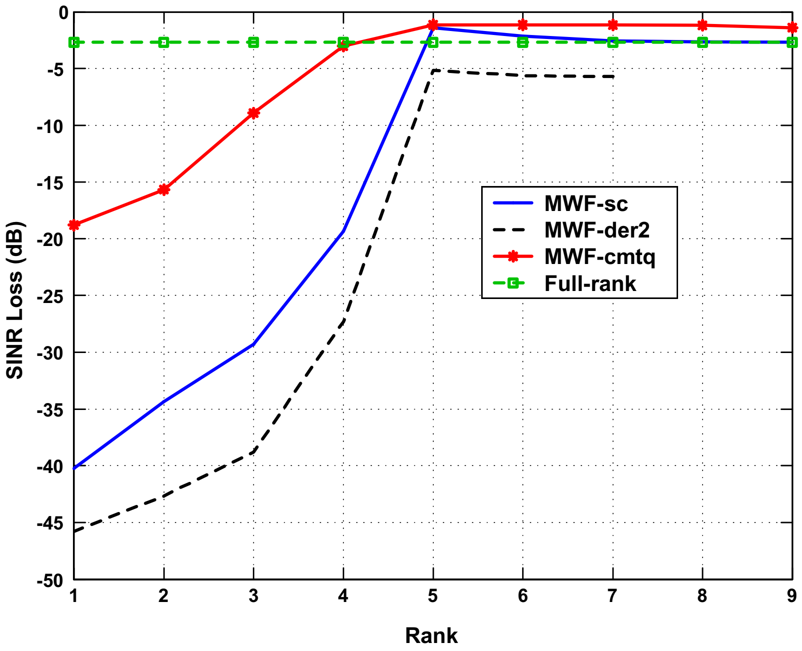

Figure 7.2: Rank Performance for 1-D Array (Test Case 5): SINR loss (dB) vs. rank of Wiener filter; Number of elements, $N = 10$; Samples $= 2N$

equal to 23° in this example. Due to the reduced DOF, as compared to the sc case, the der2 method suffers a slightly larger loss near the boresight, but it is more robust as the error is increased. Both the full-rank and sc performance degrade sharply as the mismatch increases. The cmtq method remains the best performer as the mismatch angle is varied.

Next, the 2-D STAP example for Test Case 6 in Table 7.2 is now considered. The scenario consists of an airborne sidelooking radar employing a $N = 10$ element, half-wavelength spaced linear array and a $M = 10$ pulse coherent processing interval (CPI) with no velocity misalignment (i.e. no crabbing). The dimension of the adaptive processor is thus $N_{dof} = 100$. The eigenvalue spreading in the clutter environment

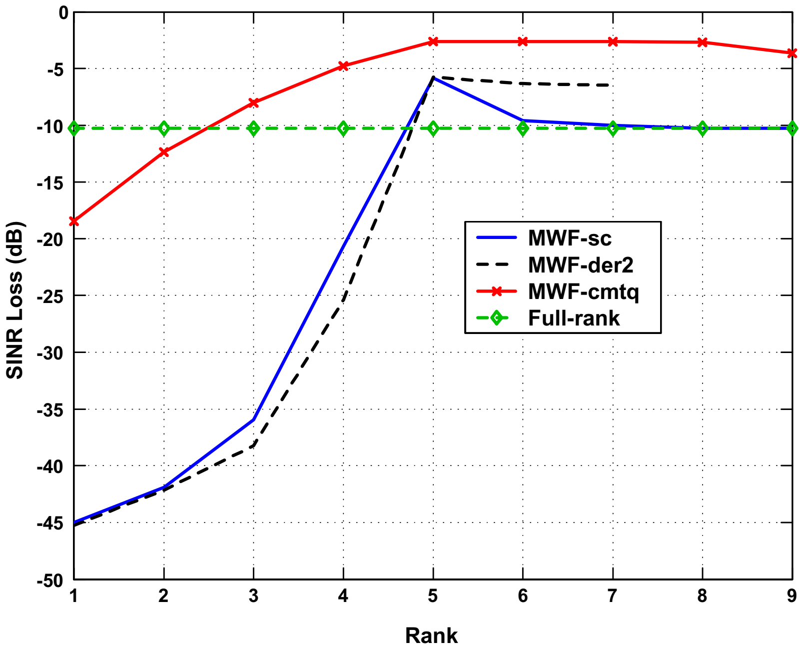

Figure 7.3: Rank Performance for 1-D Array with 6° Steering Vector Error (Test Case 5): SINR loss (dB) vs. rank of Wiener filter; Number of samples, $N = 10$; Samples $= 2N$

is modeled with an intrinsic clutter motion (ICM) of $\sigma_v = 1m/s$. The target is assumed having a SNR of 0 dB, an azimuth angle of 0° and a normalized Doppler frequency of 0.25. The clutter-to-noise ratio (CNR) is 40 dB and the clutter is assumed unambiguous in Doppler frequency with $\beta = 1$. There are two jammers at $-35$ and 30 degrees with the jammer-to-noise ratios (JNR) set at 40 dB and 30 dB above receive noise, respectively. The MWF beampatterns for single constraint (sc), derivative constraints (der2), and hybrid CMTQ (cmtq) implementations are displayed in Figure 7.5, using a rank of 45 and $2N_{dof}$ sample support. As will be shown later, a rank of 45 is best for this interference environment. When compared to the sc methods, the der2 method has a wider mainbeam, but it suffers a loss close to

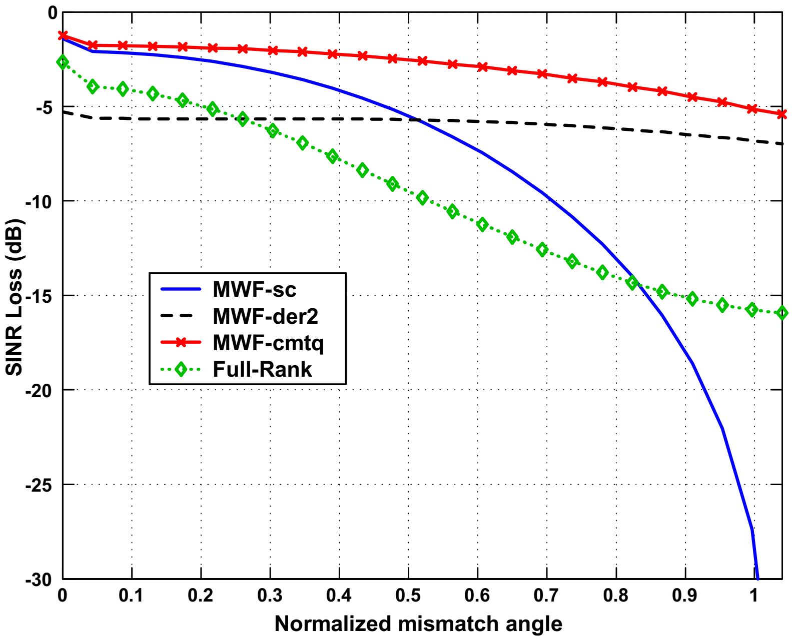

Figure 7.4: Mismatch Loss for 1-D Array (Test Case 5): SINR loss (dB) vs. mismatch angle normalized to $\frac{1}{2}BW_{nn}$; $BW_{nn}$(beamwidth null-to-null) $= \sin^{-1}(4/N)$; Rank $= 5$; Number of elements, $N = 10$; Samples $= 2N$

the boresight due to the reduced degrees of freedom. The best performance is clearly observed in the cmtq method, which creates a moderate beamwidth with remarkable sidelobe reduction and wider notches at jamming directions.

The rank performance of these approaches is shown in Figure 7.6, which represents the output SINR loss versus rank using $2N_{dof}$ sample support with no steering vector error. Due to the presence of jamming and eigenvalue spreading, the full-rank method results in a loss of 4 dB. In addition, the effective rank was observed much greater than 19 as predicted using Brennan's rule (3.26). The performance of the der2 method is again restrained due to the reduced available degrees of freedom. Both of the sc and cmtq methods exceed full-rank performance at a rank of 30 and the

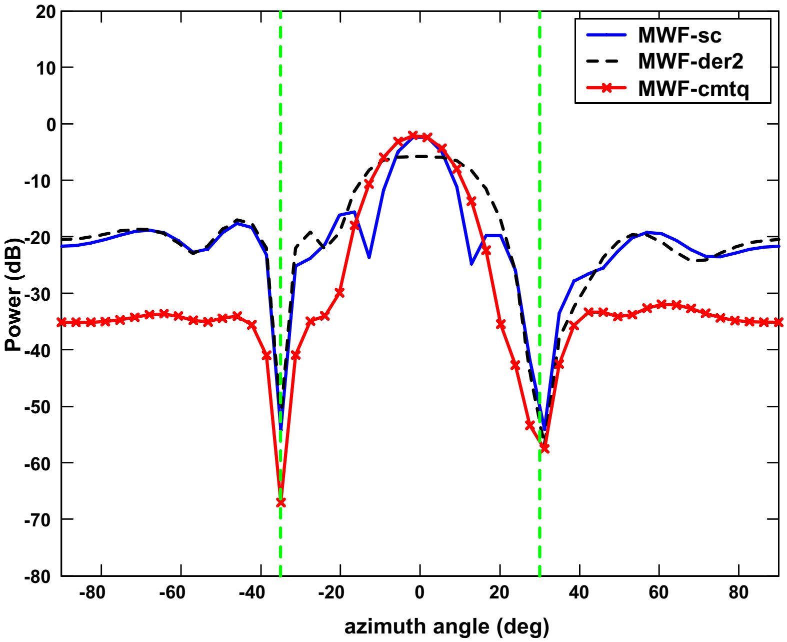

Figure 7.5: MWF Sample Beampatterns for 2-D Array (Test Case 6): Receiver output power (dB) vs. azimuth angle (deg); sc = single constraint; der2 = 0-plus-1st-plus-2nd derivatives; cmtq = combination of CMT and QPC; Intrinsic clutter velocity, $\sigma_v = 1m/s$; Two jammers are at -35, 30 degrees with JNRs = 40 and 30 dB respectively; Number of elements, $N = 10$; Number of pulses, $M = 10$; Samples $= 2MN$; Rank = 45; CMTQ parameters: beamwidth $\Delta\theta = 10^\circ$, mse deviation $\epsilon = .01$, penalty function order $p = 5.5$, widening factor $\gamma = 0.01$

sc method is slightly better. The sc approach reaches the optimum level at a rank of 40 while the cmtq method achieves its optimum level at a rank of 45. A higher rank is required for the cmtq method because the use of covariance matrix tapers (CMT) adds eigenvalue spreading into the data. This is, however, outperformed by the robustness of the cmtq approach as observed in Figure 7.7, when a steering vector error of 10° is present. Both the full-rank and sc methods suffer a loss of 14 dB as the rank is increased over 40. On the other hand, the cmtq method has a much lower loss of 5 dB at a rank of 45 and it also performs much better as compared to both

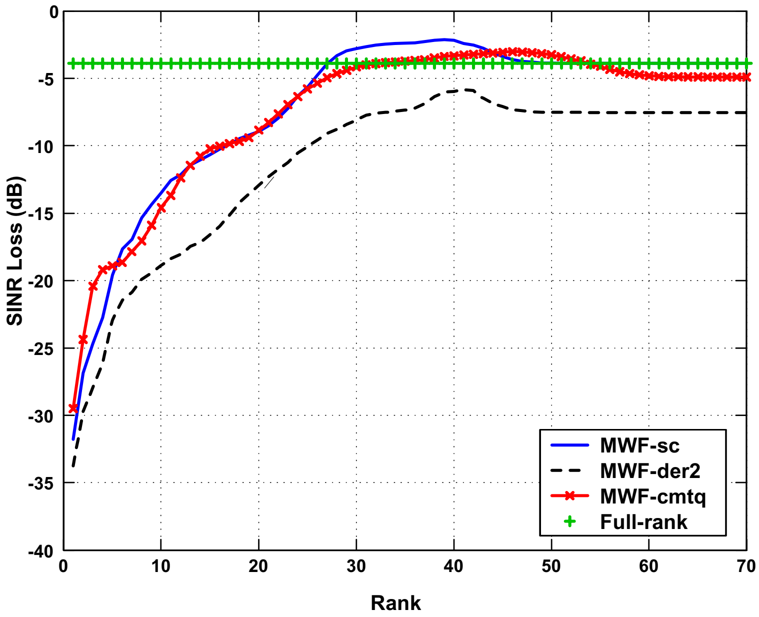

Figure 7.6: Rank Performance for 2-D Array (Test Case 6): SINR loss (dB) vs. rank of Wiener filter; Intrinsic clutter velocity, $\sigma_v = 1m/s$; Two jammers are at -35, 30 degrees with JNRs = 40 and 30 dB respectively; Number of elements, $N = 10$; Number of pulses, $M = 10$; Samples = $2MN$

the sc and der2 approaches.

Finally, for completeness in Figure 7.8, the performance of these approaches is examined as the steering mismatch error is varied, using a rank of 45 and a sample support of $2N_{dof}$. The mismatch error is again normalized to half of the array null-to-null bandwidth $(BW_{nn})$, where $BW_{nn} = \sin^{-1}(4/N)$ which is equal to 23° in this example. The same trend is observed in which the der2 has a slightly larger loss near the boresight, but it performs much better as the error is larger. Both the sc and full-rank approaches degrade sharply as the error is increased. The best performance of the cmtq method is observed as the mismatch angle is varied.

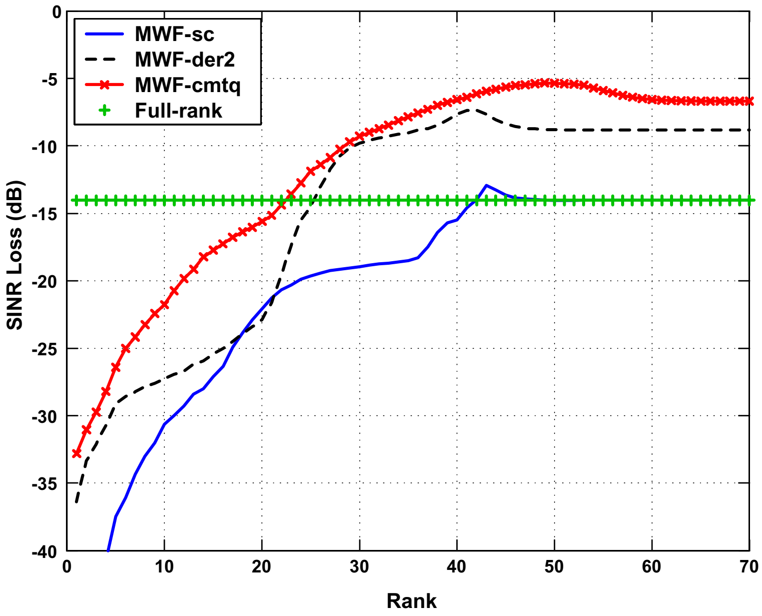

Figure 7.7: Rank Performance for 2-D Array with 10° Steering Vector Error (Test Case 6): SINR loss (dB) vs. rank of Wiener filter; Intrinsic clutter velocity, $\sigma_v = 1m/s$; Two jammers are at -35, 30 degrees with JNRs = 40 and 30 dB respectively; Number of elements, $N = 10$; Number of pulses, $M = 10$; Samples = $2MN$

## 7.3 Robustness of CMTQ Constraints

Results from Monte Carlo simulations are now provided to examine the region of convergence for adaptivity (ROC) for the MWF with CMTQ implementation. The ROC will be evaluated in terms of SINR loss as a function of sample support and rank of the Wiener filter. The robustness of the new approach will be demonstrated and compared with the standard MWF (sc) and derivative constraint MWF (der2) approaches under steering vector errors.

The first baseline example consists of a $N = 10$ element uniform linear array as shown for Test Case 6 in Table 7.1. The desired signal is at boresight. Five jammers

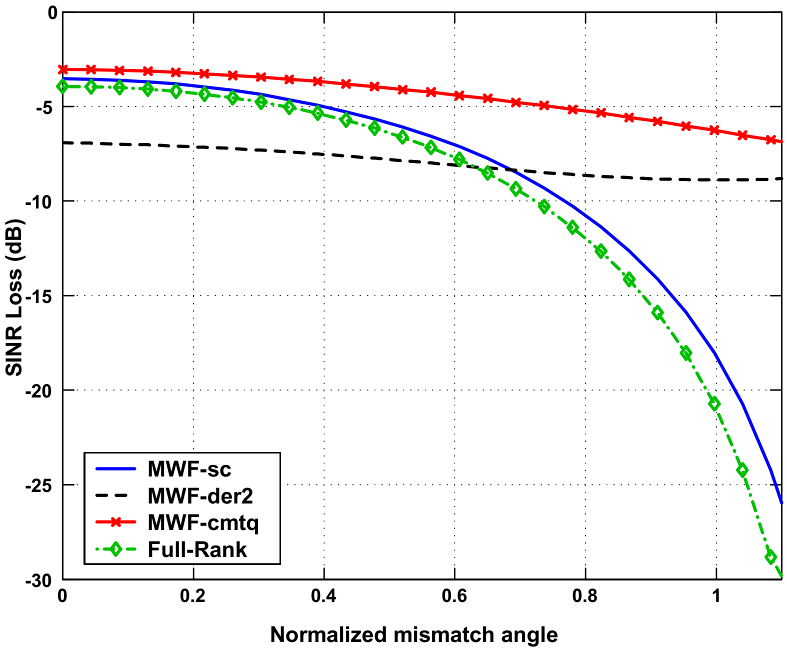

Figure 7.8: Mismatch Loss for 2-D Array (Test Case 6): SINR loss (dB) vs. mismatch angle normalized to $\frac{1}{2}BW_{nn}$; $BW_{nn}$(beamwidth null-to-null) $= \sin^{-1}(4/N)$; Intrinsic clutter velocity, $\sigma_v = 1$ m/s; Two jammers are at -35, 30 degrees with JNRs = 40 dB and 30 dB respectively; Number of elements, $N = 10$; Number of pulses, $M = 10$; Samples $= 2MN$; Rank = 45

are present at -50, -40, -30, 35, and 60 degrees. All jammer-to-noise ratios (JNRs) are set to 50 dB and the desired SNR is 0 dB above receive noise. The ROC for the sc, der2 and cmtq approaches are now being examined in the presence of 6° steering vector error. The results were computed with the rank varied from 1 to 9 and the sample support ranged from 1 to 100. When implemented, the cmtq approach is assumed to employ a QPC beam with a desired beamwidth of $\Delta\theta = 10^\circ$, a MSE deviation of $\epsilon = .01$, a penalty function order of $p = 5.5$, and a CMT widening factor of $\gamma = 0.01$.

The ROC response for the sc method is depicted in Figure 7.9. The area of this plot where the sample support is less than the rank (the lower-left triangular region) represents the region where the reduced-rank data matrix is numerically unstable. The slope or roll-off of the performance surface represents both the robustness and the sensitivity of a MWF processor as a function of rank and sample support. The effective rank of the interference covariance matrix is 5 due to the presence of 5 jammers. The results are expected to reach optimum when the rank is approaching 5 at a reasonable sample support. However, due to steering vector errors, the result has a loss of about 5 dB at rank 5 and a sample of $2N$. For all ranks greater than 5, the result is further degraded, as it converges to the full-rank solution discussed previously.

The ROC response for the der2 method is displayed in Figure 7.10. As compared to the sc method, the der2 approach also has a similar performance at rank 5 and a sample of $2N$. The improvement in SINR is observed for $6 \leq k \leq 7$ due to a wider mainbeam, which is robust for the steering vector mismatch problem. Note that $k$ denotes the rank. The performance is degraded for all ranks greater than 7, since it only retains 7 DOF due to the constraints imposed on the zero, first and second derivatives.

Finally, the ROC response for the cmtq method is depicted in Figure 7.11. The robustness of the cmtq response is remarkable as compared to both the sc and der2 approaches. It demonstrates a much greater region of support and has vast improvement in SINR especially for lower ranks ($k \leq 4$) and larger ranks ($k \geq 6$), where $k$ denotes the rank. This dominating area of coverage for adaptivity represents much better robustness and sensitivity properties in comparison with the sc and der2 approaches.

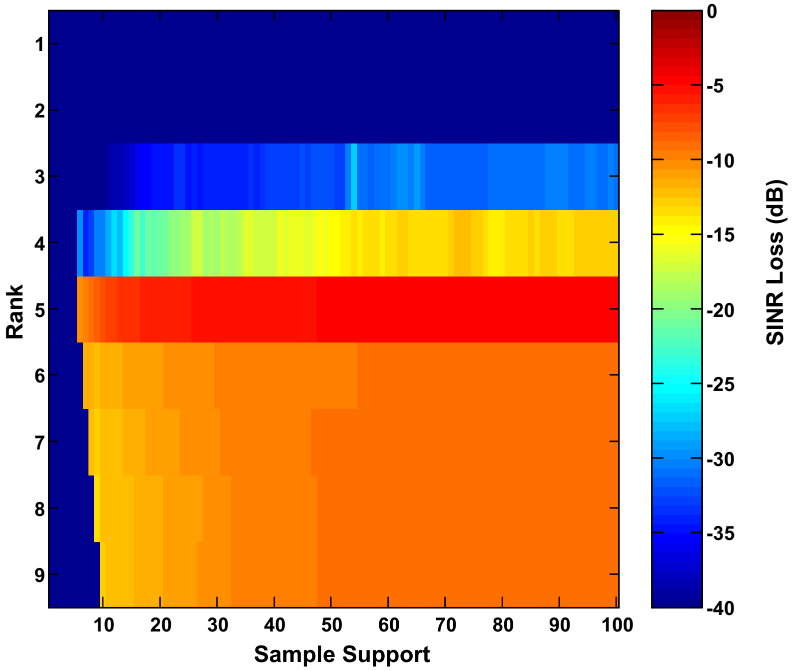

Figure 7.9: The Region of Convergence (ROC) for the MWF-sc using 1-D Array under 6° Steering Vector Error (Test Case 5): SINR loss (dB) vs. sample support and rank; Number of elements, $N = 10$; Five jammers are at -50, -40, -30, 35, and 60 degrees; Jammer-to-noise ratio, JNR = 50 dB each

Next, the 2-D STAP example for Test Case 6 in Table 7.2 is considered. The scenario again consists of an airborne sidelooking radar employing a $N = 10$ element, half-wavelength spaced linear array and a $M = 10$ pulse coherent processing interval (CPI). The dimension of the adaptive processor is thus $N_{dof} = 100$. The clutter environment is again modeled with an intrinsic clutter velocity of $\sigma_v = 1\ m/s$. The clutter-to-noise ratio (CNR) is 40 dB and the clutter is assumed unambiguous in Doppler frequency with $\beta = 1$. There are two jammers at $-35$ and 30 degrees with the jammer-to-noise ratios (JNR) set at 40 dB and 30 dB above receive noise respectively.

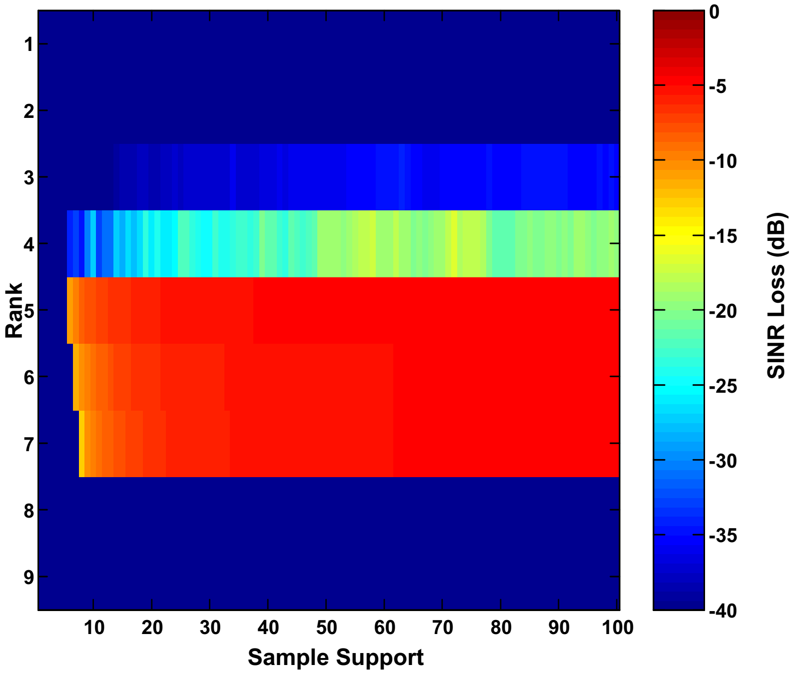

Figure 7.10: The Region of Convergence (ROC) for the MWF-der2 using 1-D Array under 6° Steering Vector Error (Test Case 5): SINR loss (dB) vs. sample support and rank; Number of elements, $N = 10$; Five jammers are at -50, -40, -30, 35, and 60 degrees; Jammer-to-noise ratio, JNR = 50 dB each

First, the ROC response for the sc method is displayed in Figure 7.12. The effective rank of the ideal clutter covariance matrix based on Brennan's rule (3.26) is about 19. However, due to the presence of two jammers and intrinsic clutter motion (ICM), the effective rank is much greater than 19 as observed. The presence of steering vector errors also causes additional loss of performance. As a result, the response can only achieve a best SINR loss of 5 dB at a rank of 40 and sample support of 200. Note that the result suffers a loss of about 15 dB at a rank of 60 and a sample of 100. This is a known problem with the MWF in very low sample support situations and when the rank is overestimated. More specifically, when the rank is

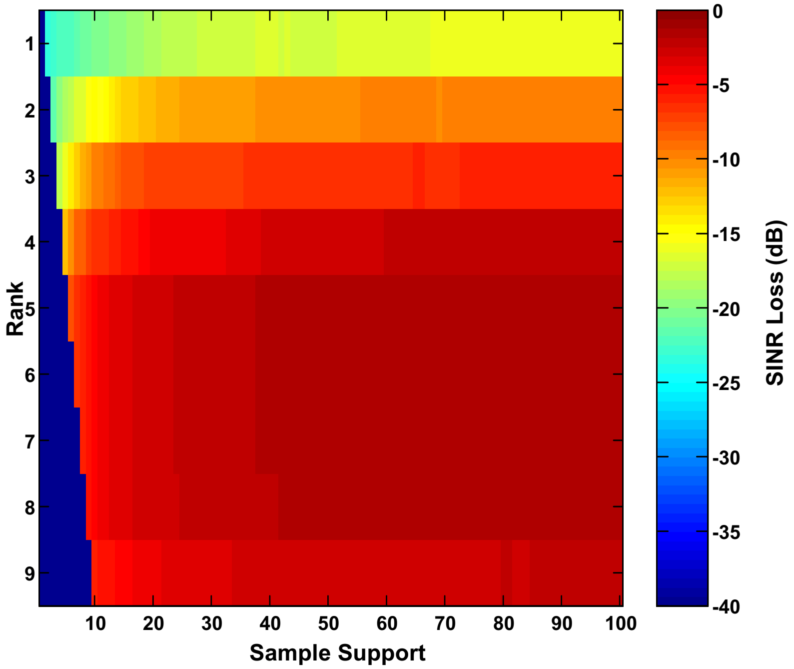

Figure 7.11: The Region of Convergence (ROC) for the MWF-cmtq using 1-D Array under 6° Steering Vector Error (Test Case 5): SINR loss (dB) vs. sample support and rank; Number of elements, $N = 10$; Five jammers are at -50, -40, -30, 35, and 60 degrees; Jammer-to-noise ratio, JNR = 50 dB each

increased such that it is larger than the dimension of the interference subspace, it is forced to choose eigenvectors lying in the noise subspace. These eigenvectors are associated with extremely small eigenvalues and insufficient sample support, which result in a distorted interference estimate and a corresponding increase in SINR loss. This loss is also intuitive, in that the result must converge to the performance of the full-adaptive STAP, in which $N_{dof} = 100$ and which is expected to have a greater loss.

Next, the ROC response for the der2 method is displayed in Figure 7.13. As compared to the sc method, the ROC covers a slightly smaller area in the rank

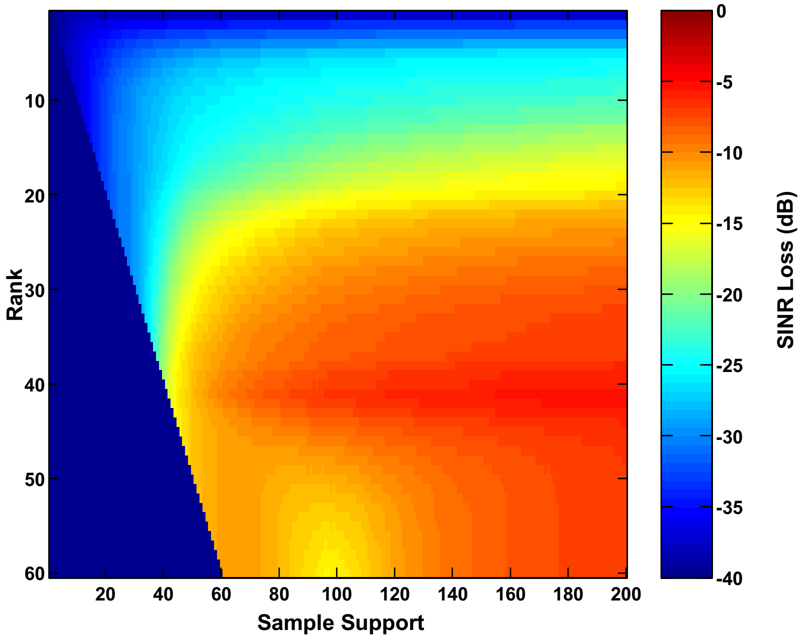

Figure 7.12: The Region of Convergence (ROC) for the MWF-sc using 2-D Array under 10° Steering Vector Error (Test Case 6): SINR loss (dB) vs. sample support and rank; Intrinsic clutter velocity, $\sigma_v = 1m/s$; Two jammers are at -35 and 30 degrees with JNRs = 40 and 30 dB respectively; Number of elements, $N = 10$; Number of pulses = 10

dimension. The best SINR loss is about 6 dB at a rank of 40 and a sample support of 200 due to the reduced degrees of freedom. For the same reason, the loss due to the rank overestimation problem at a sample of 100 and at a rank of 60 is also slightly increased.

Finally, the ROC response for the cmtq method is displayed in Figure 7.14. Here it is evident that the area covered by the ROC is significantly greater than that possible with the sc or der2 method. The ROC includes the region of both lower sample support and significantly lower rank. The result is observed having a 3 dB loss at a rank of 40 and sample support of 200. More importantly, the loss due to

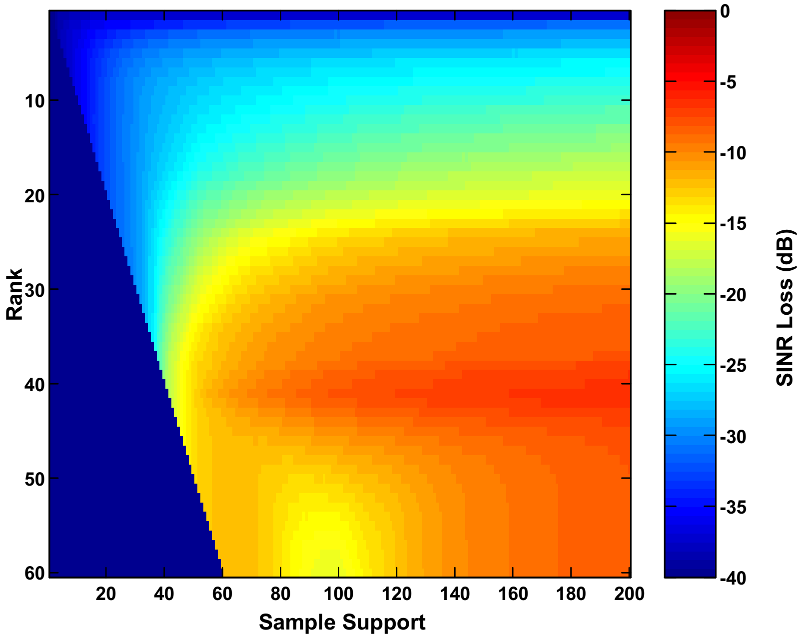

Figure 7.13: The Region of Convergence (ROC) for the MWF-der2 using 2-D Array under 10° Steering Vector Error (Test Case 6): SINR loss (dB) vs. sample support and rank; Intrinsic clutter velocity, $\sigma_v = 1m/s$; Two jammers are at -35 and 30 degrees with JNRs = 40 and 30 dB respectively; Number of elements, $N = 10$; Number of pulses = 10

the rank overestimation problem at a rank of 60 has now disappeared. The use of CMT has been shown equivalent to diagonal loading [30] which improves the noise subspace of the interference covariance matrix and also helps the rank overestimation problem. These results are important for radar detection in the real-world where the steering vector mismatch problem may be unavoidable.

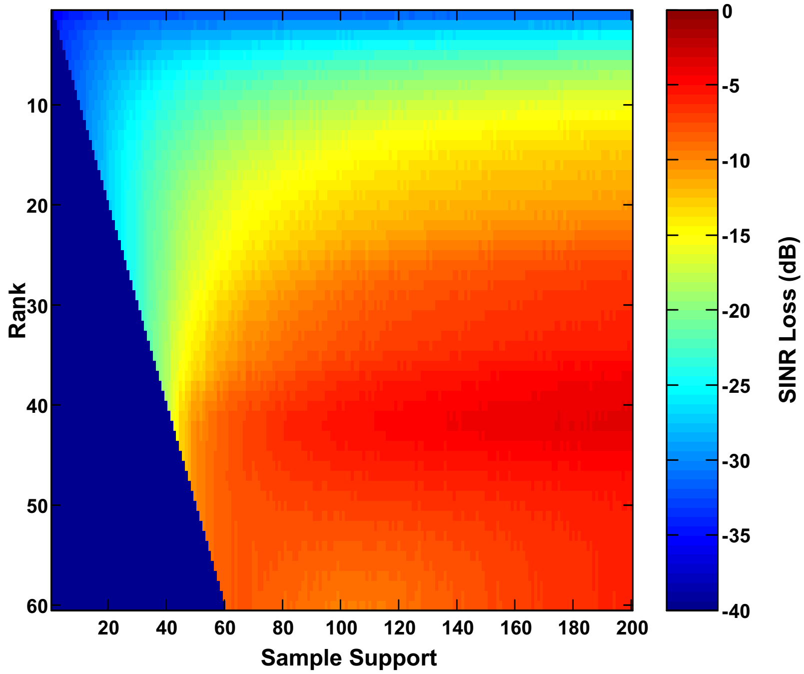

Figure 7.14: The Region of Convergence (ROC) for the MWF-cmtq using 2-D Array under 10° Steering Vector Error (Test Case 6): SINR loss (dB) vs. sample support and rank; Intrinsic clutter velocity, $\sigma_v = 1m/s$; Two jammers are at -35 and 30 degrees with JNRs = 40 and 30 dB respectively; Number of elements, $N = 10$; Number of pulses = 10

## 7.4 Summary

Numerical results in both 1-D spatial and 2-D STAP applications have demonstrated that the MWF with CMTQ implementations outperforms the standard MWF, derivative constraint MWF, and full-rank methods under steering vector errors. The 1-D example was realized with the target contaminated in all samples of the training data. The STAP example was modeled with the target confined to a data snapshot and the presence of an intrinsic clutter velocity of $\sigma_v = 1m/s$, which is typical for severely nonhomogeneous radar environments. The convergence of the new approach in both of these environments in terms of SINR loss and rank performance were remarkable under steering vector errors, and this could add significant robustness to reduced rank approaches and STAP applications. Furthermore, this chapter also examines the region of convergence for adaptivity (ROC) in which the SINR loss is computed as a function of both the effective rank and the amount of training data under steering vector errors. The vast improvement of the new approach in both lower sample support and significantly lower rank was demonstrated under steering vector errors. These results are significant for radar detection in the real world due to the greatly reduced range homogeneity requirements especially in the presence of steering vector mismatch.

# Chapter 8

# Performance Evaluation using Experimental Data

In this chapter, the robustness of the MWF with CMTQ implementation will be examined using experimental STAP data. These data are taken from the Multichannel Airborne Radar Measurement program (MCARM) [3], [59], begun by the U.S. Air Force in the early 1990's. The goal of this program was to evaluate STAP algorithms by using multichannel airborne radar data. The 2-D weight response, SINR loss, rank and sample performance under steering vector mismatch will be examined. In addition, CFAR test statistics for radar detection under steering vector errors will be evaluated. In practice, the STAP processor is restrained for each range cell such that the range cell under observation and some guard cells are excluded from the data set in order to form a signal free training data set. This process requires more samples to be utilized for the guard cells and also adds considerable computational complexity. The performance of the new approach will be evaluated as the target is present in a snapshot of the training data. It is demonstrated to outperform the standard MWF (sc), derivative-constrained MWF(der2), and full rank approaches under steering vector errors, providing robustness for real-world STAP applications.

## 8.1 Performance Metric

As defined before, the common metric employed in this dissertation is the SINR loss (5.25) which evaluates the array performance under steering vector errors

$$SINR_{loss} = \frac{\left|\mathbf{w}^H\mathbf{s}\right|^2}{\mathbf{w}^H\mathbf{R}_i\mathbf{w}}, \tag{8.1}$$

where $\mathbf{R}_i$ is the ideal covariance matrix of interference plus noise and $\mathbf{w}$ is the adaptive weight vector derived from a mismatched unit steering vector. In this expression, $\mathbf{s}$ is the unit normalized target steering vector pointing at the target direction. Note that for the cmtq approach, it is assumed that $\mathbf{s}$ is matched to the constrained quiescent beam used in transmit.

A popular adaptive constant false alarm rate (CFAR) detection test for radar is derived from the adaptive matched filter (AMF) [54]. In CFAR detection, the threshold is computed so that the radar receiver maintains a constant pre-determined probability of false alarm. The relationship between the threshold value $\alpha_t$ and the probability of false alarm $P_{fa}$ is defined as [42]

$$\alpha_t = \sqrt{2\psi^2 \ln(\frac{1}{P_{fa}})}, \tag{8.2}$$

where the noise power $\psi^2$ is assumed to be constant which is rarely true due to the dynamic nature of the airborne environment. As a result, the threshold value must be continuously updated based on the estimates of the noise variance. For full-rank STAP detection, the CFAR detection test can be based on the adaptive matched filter (AMF). The CFAR AMF value $\eta(k)$ for each range bin $k$ is defined as [54]

$$\eta(k) = \frac{\left|\mathbf{s}^H \widehat{\mathbf{R}}_k^{-1} \mathbf{x}_k\right|^2}{\mathbf{s}^H \widehat{\mathbf{R}}_k^{-1} \mathbf{s}} \gtrless \alpha, \tag{8.3}$$

where $\alpha$ is a threshold computed for some acceptable false alarm probability. Note that $\mathbf{x}_k$ refers to the single snapshot $k$ and $\widehat{\mathbf{R}}_k$ is the estimated interference covariance associated with the hypothesized range sample $k$. This test statistic is proportional to the squared magnitude of the output of the colored noise linear matched filter. The term in the denominator provides a CFAR property via a normalization by the output noise power.

In the reduced rank MWF structure, the AMF CFAR test statistic $\eta(k)$ is defined as the ratio of the Wiener beamformer output power with respect to the output noise power [24]

$$\eta(k) = \frac{\left|\mathbf{w}^H \mathbf{x}_k\right|^2}{\mathbf{w}^H \widehat{\mathbf{R}}_k \mathbf{w}} \gtrless \alpha, \tag{8.4}$$

and $\mathbf{w}$ is the adaptive weight vector derived from a presumed target steering vector.

These CFAR tests can also be used to compute a target-over-RMS metric, which is the ratio of the target AMF value $\eta(k_t)$ to the root mean square (RMS) of the other values $\eta(k \neq k_t)$ [49]

$$\text{Target-over-RMS} = 10 \log_{10} \frac{\eta(k_t)}{< \eta >_{rms}}, \tag{8.5}$$

where $k_t$ denotes a range sample where the target is present. A larger value of target-over-RMS ratio is desirable since it offers potential for better probability of target detection.

The major asset of the MCARM program was a Westinghouse L-band active-aperture antenna mounted on the port-side of a BAC 1-11 aircraft. More detailed information, including the data used here (flight 5, acquisition 575) may be found in [3], [59]. The platform was initially located west of Middletown, DE and flying due south over the Delmarva Penninsula. The boresight of the radar antenna was pointed in an easterly direction towards Atlantic City, NJ. The terrain covered in this data is relatively flat, with the primary features being rural clutter, roads and highways, and some small towns. Compared with the relatively homogeneous clutter surrounding them, radar returns from these features should cause the underlying noise and interference statistics to be nonhomogeneous.

Some specific MCARM radar parameters that will be used in this section are given in Table 8.1. The data have been preprocessed with baseband conversion decimation, channel equalization and pulse compression. For the examples in this dissertation, only the top $N = 11$ elements from the array and the first $M = 18$ pulses were employed, resulting in $N_{dof} = MN = 198$ degrees of freedom for the adaptive weight vector. When analyzing the data, a series of range-measured spatial steering vectors were provided to account for the coupling among the antenna elements. Using these provided calibrated steering vectors, artificial targets can be placed into the data.

Figure 8.1 displays the output power of MCARM radar after conventional beamforming. There are 630 unambiguous range samples available for training-data support, which are shown in the display. As observed, the first 150 range samples are dominated by transient transmit-leakage and dead-time before the first ground-returns are received. Therefore, the remaining 480 samples will be used in the examples in this section. Note that the dip in power between range cells 400 and 490 is due to the lower amplitude return from the Delaware River. This represents one form of data nonhomogeneity due to a spatial variation in the clutter-returns observed by the radar.

| **Parameter** | **Value** |
|---|---|
| Transmit Frequency | 1240 MHz |
| Transmit Beamwidth | 6.7° Az., 10.4° El. |
| Pulse Compression Ratio | 63 |
| Waveform Linear FM | 50.4 $\mu s$ (uncompressed), 1.0$us$ (compressed) |
| Range Gate | 500 ft |
| Sampling Rate | 1.25 MHz (decimated from 5 MHz) |
| Peak Transmit Power | 20 kW |
| Platform Altitude | $10,000$ ft |
| Platform Velocity | 100 m/s |
| Array Configuration | 22 elements |
| Total No. of Pulses | 128 pulses |
| Pulse Repetition Frequency (PRF) | 2 kHz |
| Number of Range Cells Available | 630 (time samples per PRI) |

Table 8.1: MCARM Data Parameters for STAP Examples (N=11 elements; M=18 pulses; Clutter echoes from rural area looking across Delaware river)

A minimum-variance distortionless response (MVDR) spectrum of the data is displayed in Figure 8.2, which is used to estimate the noise floor. The relative peak clutter-to-noise (CNR) ratio can be estimated from the spectrum to have a value of approximately 60 dB. The spectrum also indicates that the clutter is Doppler unambiguous and the clutter-ridge has a slope, or $\beta$, of approximately 1 in the angle-Doppler domain. This value can be calculated from the parameters in Table 8.1 and (3.14) yields $\beta = \frac{vT_r}{d/2} = 0.828$, where $v$ is the platform velocity, $T_r$ is the pulse repetition interval and $d$ is the element spacing.

## 8.2 SINR Performance

The MCARM data are now employed to examine the performance of the MWF with CMTQ implementation (cmtq), standard MWF (sc), derivative constraint MWF(der2)

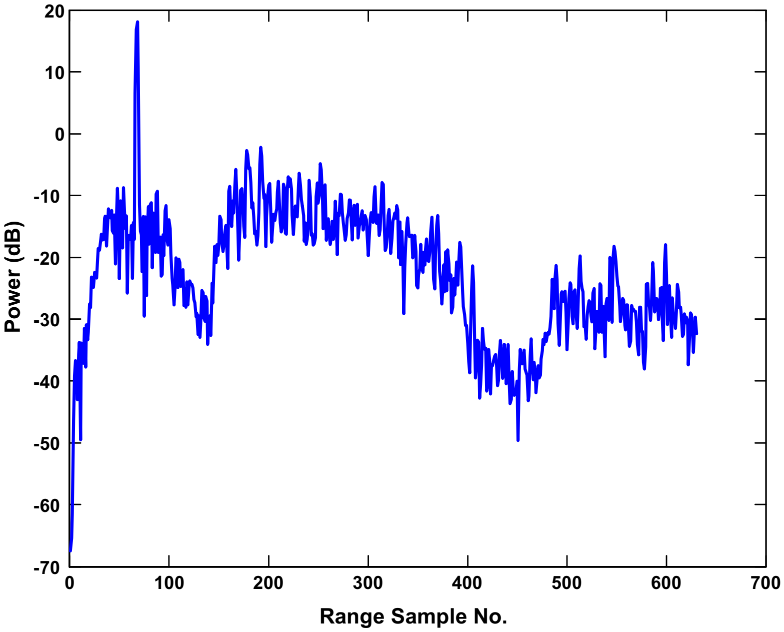

Figure 8.1: Received Power of MCARM Radar Data after Conventional Beamforming; Received power (dB) vs. range sample no.; Clutter echoes from rural area looking across Delaware river; Number of elements, $N = 11$; Number of pulses, $M = 18$; Received power shown is averaged over 18 pulses per range gate

and full rank approaches. The results will first be evaluated using $1N_{dof}$ sample support, since adaptation in low sample support is important for nonhomogeneous environments and a larger data set may cause problems due to nonhomogeneous clutter effects. The MCARM radar data considered again consists of 11 elements and 18 pulses (after pulse compression) and the total degrees of freedom is $N_{dof} = 198$. The performance in terms of SINR loss as a function of the sample support and steering vector errors will also be examined. There is one target inserted at range sample 145. The target SNR is 25 dB (element and pulse level) and the steering vector is pointing at $0^\circ$ azimuth angle with a normalized Doppler frequency of $-0.25$. When implemented, the cmtq approach is assumed to employ a QPC beam with a beamwidth

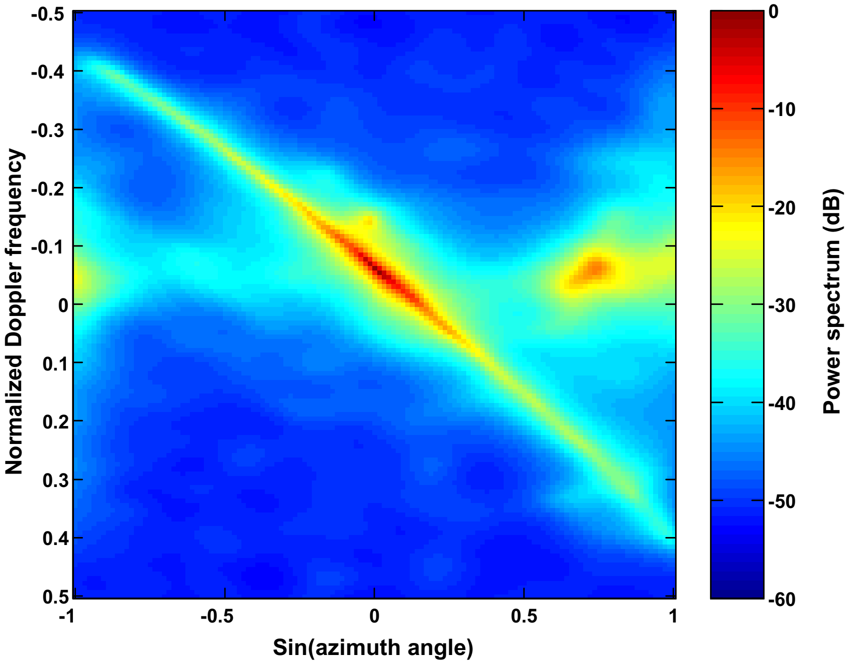

Figure 8.2: MVDR Power Spectrum for MCARM Radar Data: Power (dB) vs. normalized Doppler frequency and sin(azimuth angle); Power is normalized to 1; Doppler frequency is normalized to PRF; Number of elements, $N = 11$; Number of pulses, $M = 18$

of $\Delta\theta = 10°$, an MSE deviation of $\epsilon = .01$, a penalty function order of $p = 5.5$, and a CMT widening factor of $\gamma = 0.01$ in both azimuth angle and Doppler frequency directions.

First, the two-dimensional (2-D) STAP weight response for the MCARM radar data is examined using $1N_{dof}$ sample support. Figure 8.3, 8.4, and 8.5 display the normalized weight response for the full-rank, sc, and cmtq implementations respectively. A rank of 55 is used, which is best for this interference environment as will be shown later. In these responses, the angle-Doppler location defined by the target steering vector receives a distortionless gain, and the two-dimensional clutter ridge is also simultaneously nulled as expected. As compared to the sc response, the der2 method is clearly identified with poorer performance and a much wider beamwidth in the azimuth direction due to the constraints imposed in the azimuth direction. In addition, poor angle-Doppler sidelobes are also observed in the der2 response. These artifacts are due to the reduced degrees of freedom and the mismatch of antenna geometry when forming the steering vector derivatives (5.22). This may be caused by the fact that the actual element spacing in the MCARM radar could be slightly different due to real-world conditions. The response also exhibits a very narrow clutter null which may result in undernulled clutter due to any slight deviations in the angle-Doppler clutter distribution (from that in the training data). On the other hand, the cmtq response is observed to have a moderate beamwidth with a more robust clutter notch and desirable sidelobe levels in both azimuth and Doppler frequency dimensions. A spatial snapshot comparison of these responses at the normalized target Doppler frequency ($-0.25$) is shown in Figure 8.6. As compared to the sc method, the der2 method again has a poorer response. The best performance is clearly observed in the cmtq method, which demonstrates a moderate beamwidth with remarkable sidelobe reduction.

Next, the rank performance of these approaches is compared in Figure 8.7 using the same $1N_{dof}$ sample support with no steering vector errors. Additionally, the full-rank MVDR is also considered as a benchmark, which results in a loss of 18 dB due to sample estimation errors and the use of $1N_{dof}$ sample support. All reduced rank MWF approaches showed a robustness over the full-rank approach, especially for all ranks greater than 20. The cmtq method has a slight improvement as compared to the standard MWF (sc) method for all ranks between 30 to 90, while the

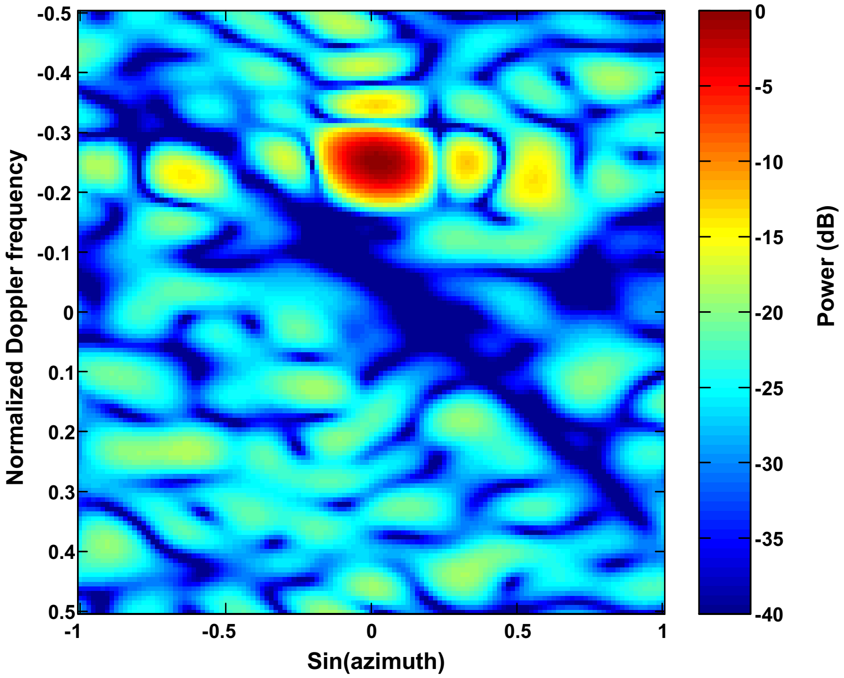

Figure 8.3: Weight Response for MWF-sc using MCARM Data: Receiver output power (dB) vs. sin (azimuth angle) and Doppler frequency; Doppler frequency is normalized to PRF; sc = standard MWF; Number of elements, $N = 11$; Number of pulses, $M = 18$; Samples = $MN$; Rank = 55; Target is at boresight with normalized Doppler frequency = -0.25 and SNR = 25 dB

derivative constraints (der2) method has a much larger loss. Figure 8.8 examines the same example when a steering vector error of 10° is introduced into the environment. Due to the mismatch error and the presence of the target in the data, the full-rank solution suffers an additional 30 dB SINR loss. The sc method again converges to the full-rank solution, which hinders its performance. The der2 method is a slight improvement over the standard sc approach. The cmtq, on the other hand, is a significant improvement and provides a much more robust region of rank with which to implement the processor.

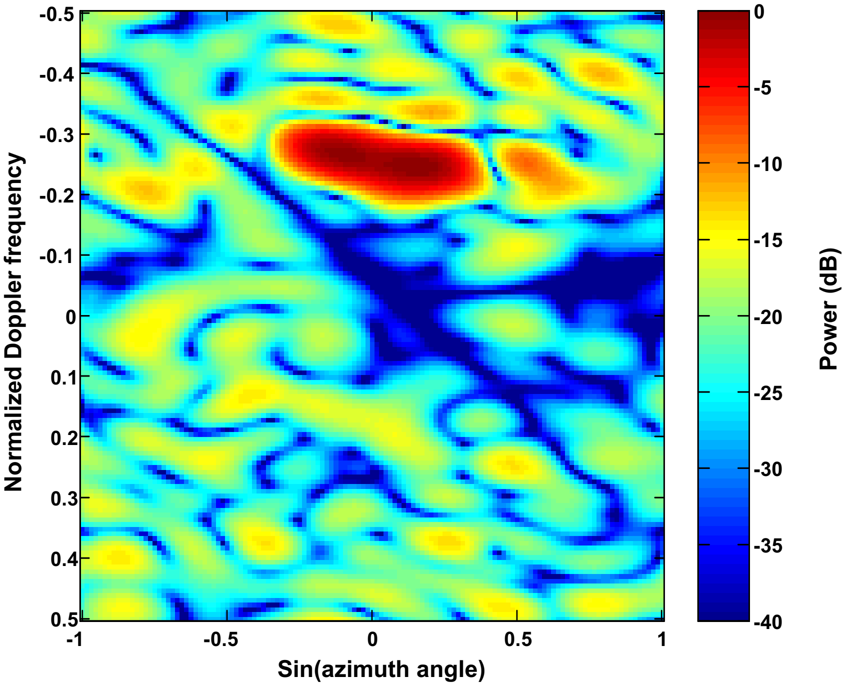

Figure 8.4: Weight Response for MWF-der2 using MCARM Data: Receiver output power (dB) vs. sin (azimuth angle) and Doppler frequency; Doppler frequency is normalized to PRF; der2 = 0-plus1st-plus2nd derivatives constraints; Number of elements, $N = 11$; Number of pulses, $M = 18$; Samples = $MN$; Rank = 55; Target is at boresight with normalized Doppler frequency = -0.25 and SNR = 25 dB

Next, the SINR loss as a function of sample support is examined as shown in Figure 8.9. All MWF approaches are now implemented with a rank of 55, which is the best rank observed in Figure 8.7. As expected, the full-rank approach has a 3 dB loss when the sample size reaches $2N_{dof}$ (396) The der2 technique again has poor performance. Both the standard MWF (sc) and cmtq approaches exceed the full-rank performance and have similar performance as the sample size is less than $2N_{dof}$. As compared to the sc method, the cmtq has a slight improvement at $1N_{dof}$ sample support and a slight loss at $2N_{dof}$ sample support. The effect of steering vector errors

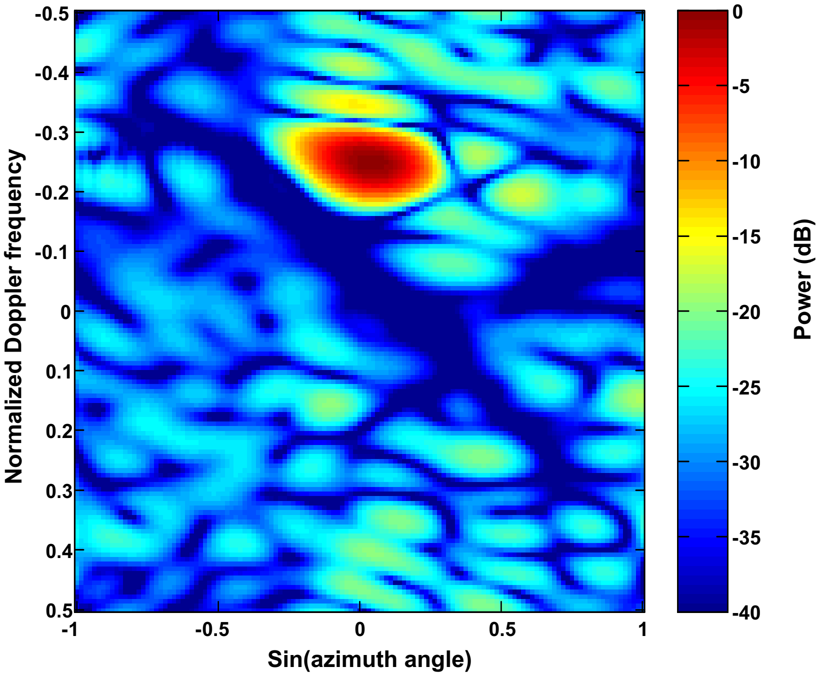

Figure 8.5: Weight Response for MWF-cmtq using MCARM Data: Receiver output power (dB) vs. sin (azimuth angle) and normalized Doppler frequency; Doppler frequency is normalized to PRF; cmtq = combination of CMT and QPC constraints; Number of elements, $N = 11$; Number of pulses, $M = 18$; Samples = $MN$; Rank = 55; Target is at boresight with normalized Doppler frequency = -0.25 and SNR = 25 dB

is displayed in Figure 8.10, using the same rank of 55. Due to target presence in a snapshot of the training data, both the sc and full-rank methods suffer a large SINR loss for sample support less than $1N_{dof}$ (198). The same trend is essentially observed for the der2 method. The cmtq method is clearly the most robust technique for all levels of sample support.

Finally, for completeness in Figure 8.11, we examine the SINR loss as the steering mismatch error is varied, using a $1N_{dof}$ sample and the same rank of 55. The mismatch error is normalized to half of the array null-to-null beamwidth ($BW_{nn}$),

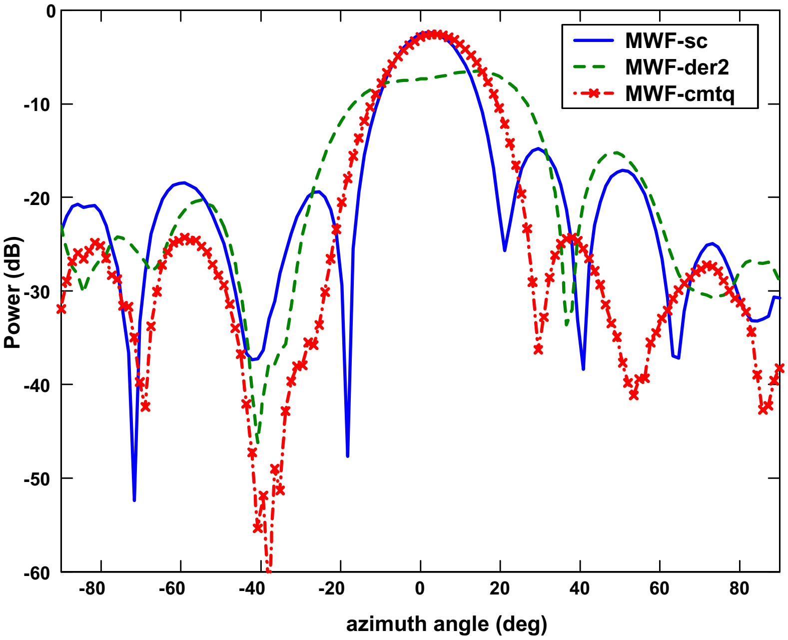

Figure 8.6: MWF Sample Beampatterns for MCARM Data: Receiver output power (dB) vs. azimuth angle (deg); Number of elements, $N = 11$; Number of pulses, $M = 18$; Samples = $MN$; Rank = 55; Target is at boresight with normalized Doppler frequency = -0.25 and SNR = 25 dB

where $BW_{nn} = \sin^{-1}(4/N)$. The der2 method again has a poor performance. The full-rank performance degrades sharply while both the sc and der2 methods result in similar loss as the mismatch increases. The cmtq method remains the best performer as the mismatch angle is varied.

## 8.3 CFAR Results

In this section, AMF CFAR test statistics for radar detection under steering vector errors will be evaluated using $1N_{dof}$ sample support. A target-present or target-absent decision can be made for each Doppler-angle range cell (range sample) by

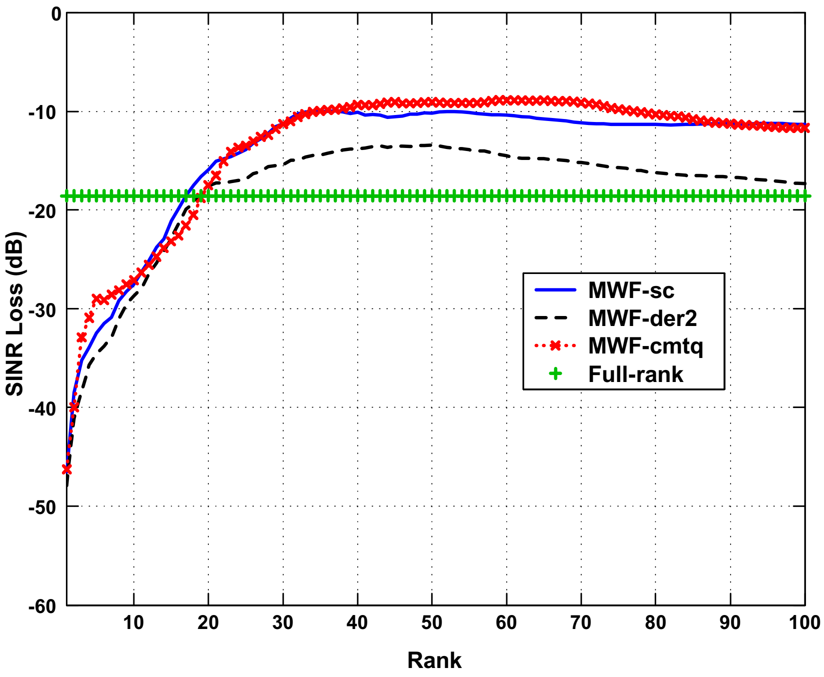

Figure 8.7: Rank Performance for MCARM Radar Data: SINR loss (dB) vs. rank of Wiener filter; Number of elements, $N = 11$; Number of pulses, $M = 18$; Samples $= MN$

comparing the CFAR test statistic to a threshold precomputed for some acceptable false alarm probability. For each range cell under observation, the training data is updated to select samples that are local to the range cell under test. This is required to obtain the best training data due the nonstationary nature of the interference environment. In practice, the range cell under test and a minimum number of guard cells are also excluded from the data set in order to form a signal-free training data set. This process requires more samples to be utilized for the guard cells and also adds considerable computational complexity. Furthermore, the training data may still be contaminated due to the presence of nonhomogeneous discrete clutter and other undesirable discrete targets. In the following results, the performance of the

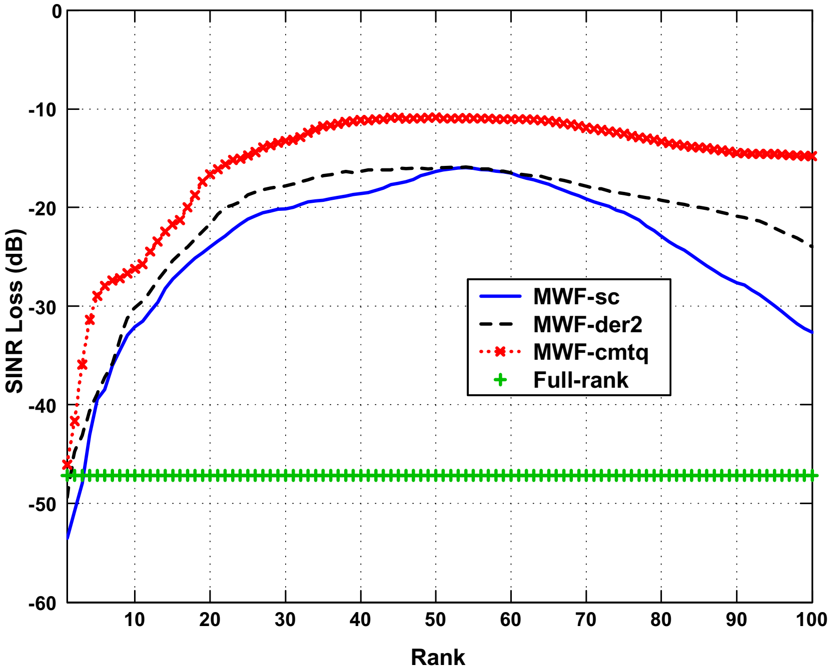

Figure 8.8: Rank Performance for MCARM Radar Data with 10° Steering Vector Error: SINR loss (dB) vs. rank of Wiener filter; Number of elements, $N = 11$; Number of pulses, $M = 18$; Samples $= MN$

new approach will be evaluated as the target is assumed present in a snapshot of the training data. The MCARM radar example again consists of 11 elements and 18 pulses (after pulse compression) and the total degrees of freedom is $N_{dof} = 198$. When implemented, the cmtq approach is assumed to employ a QPC beam with a beamwidth $\Delta\theta = 10°$, an MSE deviation $\epsilon = .01$, a penalty function order $p = 5.5$, and a CMT widening factor $\gamma = 0.01$ in both azimuth angle and Doppler frequency directions.

In the first simulation, the target is assumed present at range sample 145. The SNR level is 25 dB with azimuth angle at 0° and normalized Doppler frequency at

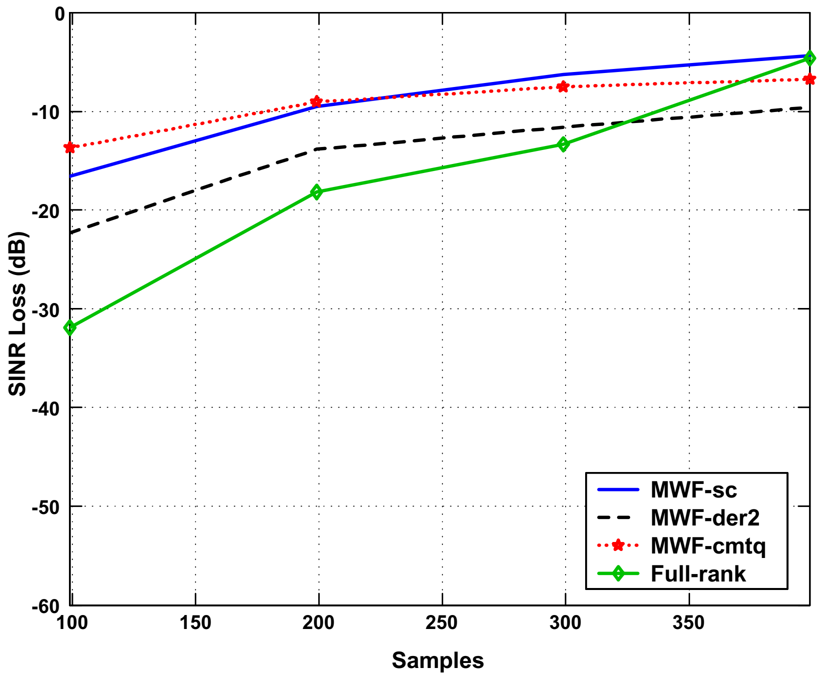

Figure 8.9: Sample Performance for MCARM Radar Data: SINR loss (dB) vs. number of samples; Number of elements, $N = 11$; Number of pulses, $M = 18$; Rank = 55

$-0.25$. Figures 8.12, 8.13, and 8.14 display the AMF CFAR test statistics for the full-rank, sc, and cmtq approaches respectively with 10° steering vector error. All reduced rank approaches are again implemented with a rank of 55. For the Wiener filter, the AMF CFAR test statistic $\eta(k)$ at a range sample $k$ is defined as the ratio of the Wiener beamformer output power with respect to the output noise power (8.4). The target-over-RMS metric is the ratio of the target AMF value to the root mean square of the other values (8.5). Note that the target AMF value corresponds to the AMF CFAR test statistic at the target range sample. For the full-rank method, the target-over-RMS metric has a value of 7.5 dB. It is 10.5 dB using the sc method and it achieves 13.5 dB using the cmtq approach.

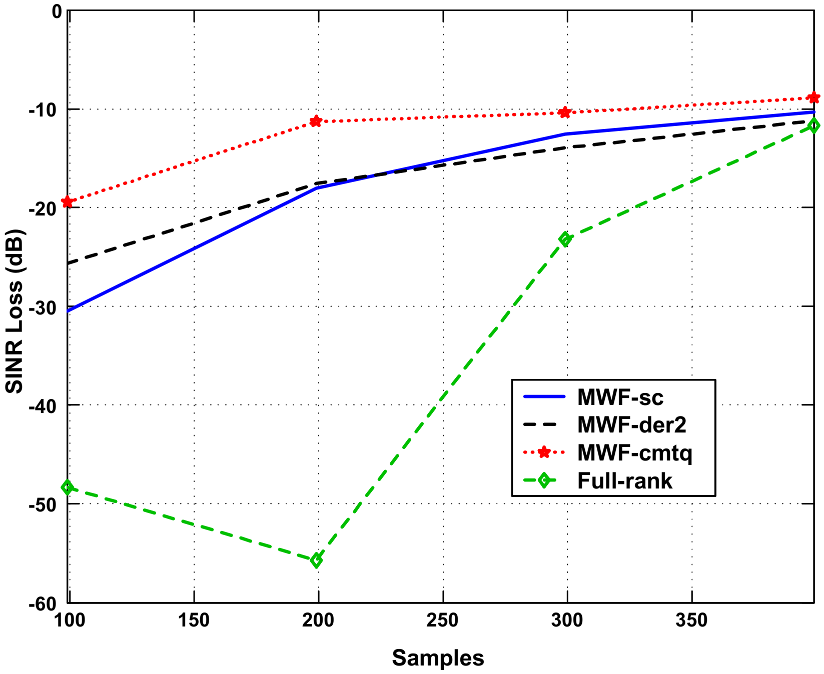

Figure 8.10: Sample Performance for MCARM Radar Data with 10° Steering Vector Error: SINR loss (dB) vs. number of samples; Number of elements, $N = 11$; Number of pulses, $M = 18$; Rank = 55

The ratio of target AMF value over the next highest peak is also important for radar target detection, because a larger value likely indicates a higher probability of detection and a lower probability of false alarm. These values are also shown in the same displays and the trend is similar as before. The full-rank method suffers 3.2 dB loss. The result is 1 dB for the sc approach and increases to 4.6 dB for the cmtq method. Note that these results are relatively low due to the use of low sample support. The poor performance for the full-rank method is expected due to estimation errors and numerical issues associated with inverting the nearly rank-deficiency covariance matrix. The improvement of the cmtq method as compared to

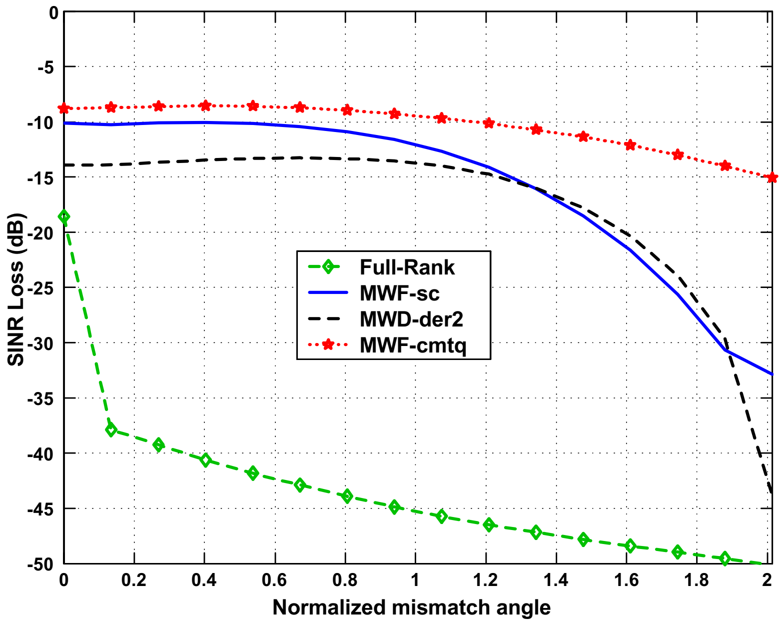

Figure 8.11: Mismatch Loss for MCARM Radar Data: SINR loss (dB) vs. mismatch angle normalized to $\frac{1}{2}BW_{nn}$; $BW_{nn}$(beamwidth null-to-null) $= \sin^{-1}(4/N)$; Number of elements, $N = 11$; Number of pulses, $M = 18$; Samples $= MN$; Rank $= 55$

the sc approach again demonstrates its robustness in the presence of steering vector errors in limited sample support.

In the next simulation, the effect of varying the target location in the MCARM data is examined in Figure 8.15 using $1N_{dof}$ sample support with no steering vector errors. The same target is injected into the MCARM data with its location varied from range sample 0 to 440. For each target insertion, a new CFAR test statistic is generated as described before, and a measure of target-over-RMS ratio is computed. Note that the first 150 range samples in the original MCARM data set were not used, and sample 0 in this display corresponds to sample 151 in the original MCARM data (Figure 8.1). The degradation of the full-rank method is again due to sample

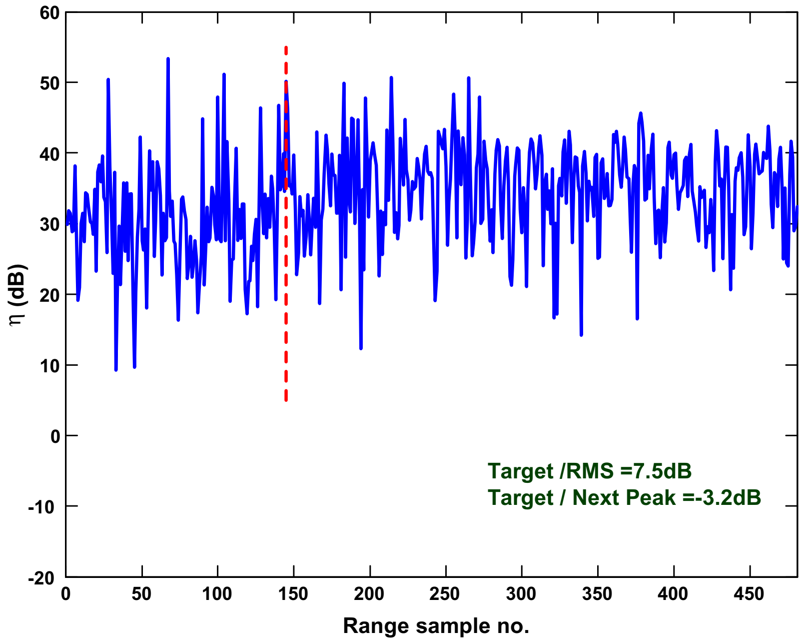

Figure 8.12: CFAR Test statistic for Full-rank using MCARM Data with 10° steering vector error: $\eta$ (dB) vs range sample no.; $\eta$ denotes ratio of beamformer output power over output noise power; Number of elements, $N = 11$; Number of pulses, $M = 18$; Samples $= MN$; Rank $= 55$; Target is at range sample 145 with azimuth angle $= 0°$, normalized Doppler frequency $= -0.25$, and SNR $= 25$ dB; The vertical line indicates target location

estimation errors. As compared to the sc method, the cmtq method has a slight improvement as the target location is varied. When the target sample is greater than 250, which correspond to sample 400 in the original MCARM data, all methods have better results. This is due to the reduction in clutter returns from the Delaware River, which is displayed as a dip between sample 400 to 490 in Figure 8.1. The robustness of the cmtq method is illustrated in Figure 8.16 with the presence of 10° steering vector error. Due to this mismatch, the full-rank method suffers a greater loss, as we expected. The cmtq is clearly the most robust technique for all target

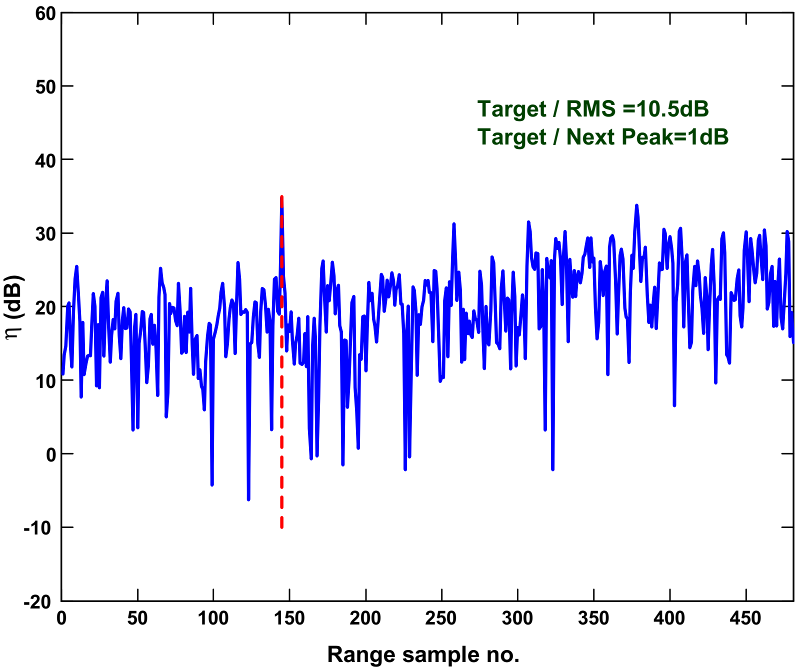

Figure 8.13: CFAR Test statistic for MWF-sc using MCARM Data with 10° steering vector error: $\eta$ (dB) vs range sample no.; $\eta$ denotes ratio of beamformer output power over output noise power; Number of elements, $N = 11$; Number of pulses, $M = 18$; Samples $= MN$; Rank $= 55$; Target is at range sample 145 with azimuth angle $= 0°$, normalized Doppler frequency $= -0.25$, and SNR $= 25$ dB; The vertical line indicates target location

locations and provides great improvement under steering vector errors.\

## 8.4 Summary

The performance of the MWF with CMTQ implementation was evaluated with the standard MWF, derivative constraint MWF and full rank approaches using experimental MCARM data. The new approach was examined employing $1N_{dof}$ sample support and has provided similar SINR performance as compared with the standard

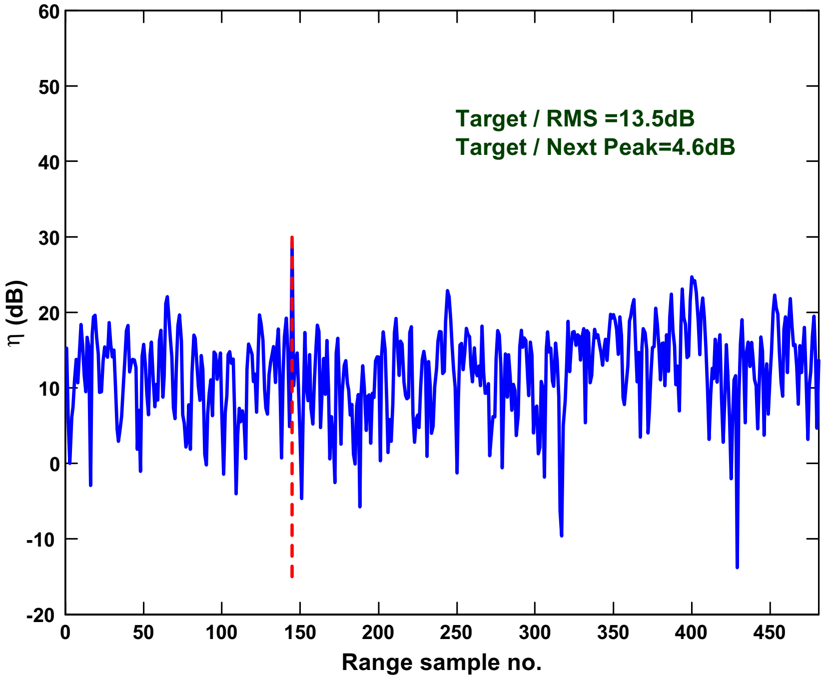

Figure 8.14: CFAR Test statistic for MWF-cmtq using MCARM Data with 10° steering vector error: $\eta$ (dB) vs range sample no.; $\eta$ denotes ratio of beamformer output power over output noise power; Number of elements, $N = 11$; Number of pulses, $M = 18$; Samples $= MN$; Rank $= 55$; Target is at range sample 145 with azimuth angle $= 0°$, normalized Doppler frequency $= -0.25$, and SNR $= 25$ dB; The vertical line indicates target location

MWF without the presence of steering vector mismatch. The robustness and improvement of the new approach was, however, clearly demonstrated both in terms of rank and sample performance under steering vector errors. In addition, CFAR test statistics were examined for radar target detection in which the ratio of the beamformer output power over the noise power is estimated for each range cell. In practice, the STAP processor is restrained for each range cell such that the range cell under observation and some guard cells are excluded from the data set in order to form a signal free training data set. This process requires more samples to be utilized for the

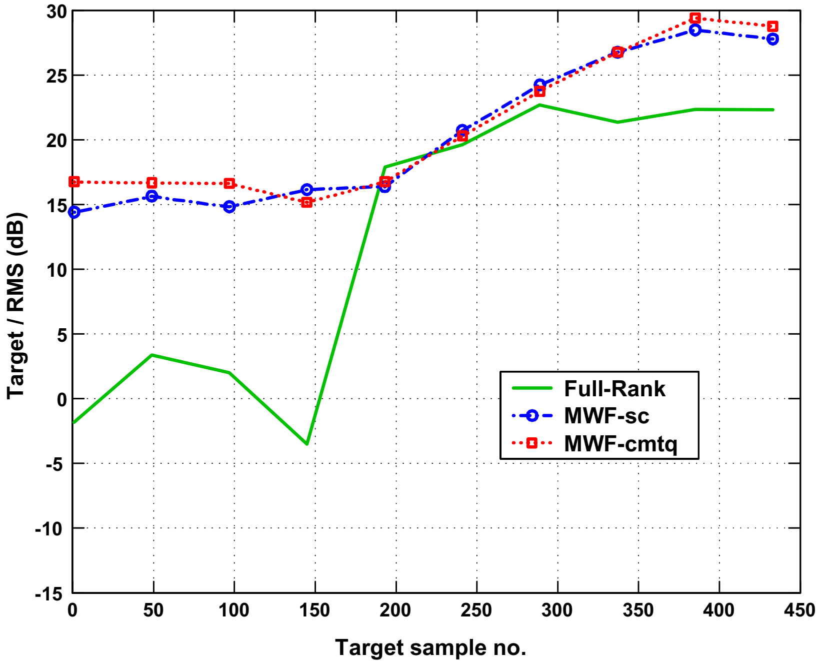

Figure 8.15: Target-over-RMS Comparison of CFAR test statistics with target sample varied: Target / RMS (dB) vs. target sample no.; It is the ratio of CFAR test statistic at target range sample over the RMS of other values; Number of elements, $N = 11$; Number of pulses, $M = 18$; Samples $= MN$; Rank $= 55$; Target azimuth angle $= 0°$ with normalized Doppler frequency $= -0.25$, and SNR $= 25$ dB

guard cells and also adds considerable computational complexity. The new approach has demonstrated superior CFAR performance even when the target is present in the training data, providing robustness for real-world STAP applications.

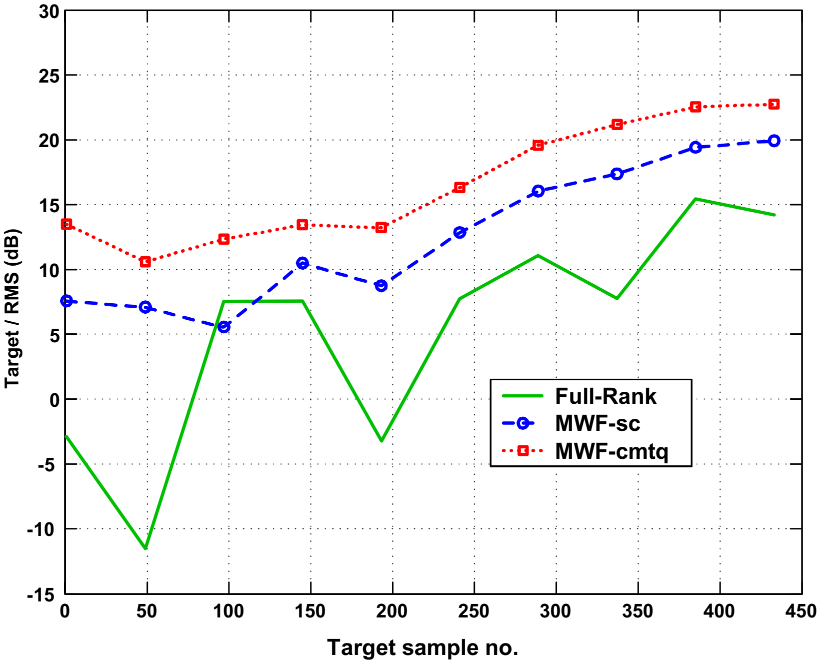

Figure 8.16: Target-over-RMS Comparison of CFAR test statistics with target sample varied and 10° steering vector error: Target / RMS (dB) vs target sample no.; It is the ratio of CFAR test statistic at target range sample over the RMS of other values; Number of elements, $N = 11$; Number of pulses, $M = 18$; Samples $= MN$; Rank $= 55$; Target azimuth angle $= 0°$ with normalized Doppler frequency $= -0.25$ and SNR $= 25$ dB

# Chapter 9

# Effects of Mainbeam Jamming and Computational Requirements

The proposed CMTQ implementation modifies the MWF beamformer constraints to widen the desired signal protection region and lessen the effects of steering vector mismatch. This robustness may however cause the radar to be more susceptible to main beam jamming and increase the off-axis angle minimum where jammers can be effectively nulled out. In this chapter, the effect of main beam jamming and trade-offs to steering vector mismatch will be examined. Specifically, an approximate formula for the off-axis angle minimum is presented and validated using Monte Carlo numerical results. In addition, approximate formulas for the computational savings and memory requirements for the new approach are compared with the standard MWF and full rank approaches.

## 9.1 Mainbeam Jamming

This section examines the effect of main beam jamming and presents an approximate formula to estimate the off-axis angle minimum where jammers can be effectively nulled out. The formulation is first analyzed for the case with a single jammer and white noise only, and the result will be shown proportional to the 3 dB beamwidth obtained from a conventional (fixed) array. Since the use of covariance matrix tapers (CMT) is equivalent to a sinc tapering distribution on the antenna aperture, the result can be extended to approximate the off-axis angle minimum for the new approach.

### 9.1.1 Minimum Off-axis Angle for Effective Jammer Cancellation

For an environment with a jamming source and uncorrelated white noise, the output SINR can be examined as the power and direction of the jammer are varied. The interference covariance matrix can be expressed as

$$\mathbf{R} = \sigma^2 \mathbf{I} + \alpha_j \mathbf{s}_j \mathbf{s}_j^H, \tag{9.1}$$

where $\alpha_j$ and $\mathbf{s}_j$ are the power and steering vector of the jammer respectively, and $\sigma^2$ is the noise variance. Applying the matrix inversion formula [33] to $\mathbf{R}$, and setting $\sigma^2$ to unity for convenience yields

$$\mathbf{R}^{-1} = \mathbf{I} - \frac{\alpha_j \mathbf{s}_j \mathbf{s}_j^H}{1 + \alpha_j \mathbf{s}_j \mathbf{s}_j^H}. \tag{9.2}$$

The optimum adaptive weight (2.8) can then be expressed

$$\mathbf{w} = \mathbf{R}^{-1}\mathbf{s} = (\mathbf{I} - \frac{\alpha_j \mathbf{s}_j \mathbf{s}_j^H}{1 + N\alpha_j})\mathbf{s}, \tag{9.3}$$

where $\mathbf{s}$ is the target steering vector, $N$ is the number of elements, and $\mathbf{s}_j^H \mathbf{s}_j = N$.

The desired signal output power, jamming output power, and uncorrelated noise output power can be found based on this optimum weight. The signal output power is denoted

$$p_s = \alpha_s \left|\mathbf{s}^H\mathbf{w}\right|^2 = \alpha_s \left|1 - \frac{N\alpha_j \left|\rho\right|^2}{1+N\alpha_j}\right|^2 = \frac{N^2\alpha_s\{1+N\alpha_j(1-\left|\rho\right|^2\}^2}{(1+N\alpha_j)^2}, \tag{9.4}$$

where $\alpha_s$ is the signal input power and $\rho = \mathbf{s}_j^H\mathbf{s}$. Note that $\left|\rho\right|^2$ represents the normalized jamming amplitude gain. Similarly, the jamming output power can be found

$$p_j = \alpha_j \left|\mathbf{s}_j^H\mathbf{w}\right|^2 = \frac{N^2\alpha_j \left|\rho\right|^2}{(1+N\alpha_j)^2}. \tag{9.5}$$

Likewise, the uncorrelated noise output power can be determined

$$p_n = \mathbf{w}^H\mathbf{w} = \frac{N[1+(1-\left|\rho\right|^2)(2N\alpha_j + N^2\alpha_j^2)]}{(1+N\alpha_j)^2}. \tag{9.6}$$

The combined jamming and noise power is the sum of (9.5) and (9.6)

$$p_{j+n} = \frac{N(1+N\alpha_j)[(1+N\alpha_j(1-\left|\rho\right|^2)]}{(1+N\alpha_j)^2}. \tag{9.7}$$

The output signal to noise ratio (SINR) is the ratio of (9.4) to (9.7)

$$SINR_q = \frac{p_s}{p_{j+n}} = \frac{N\alpha_s[(1+N\alpha_j(1-\left|\rho\right|^2)]}{1+N\alpha_j} = N\alpha_s\left(1 - \frac{N\alpha_j\left|\rho\right|^2}{1+N\alpha_j}\right). \tag{9.8}$$

When the jamming power ($\alpha_j$) is large, this ratio approaches

$$SINR_q \approx N\alpha_s(1-\left|\rho\right|^2). \tag{9.9}$$

This is equivalent to the output SNR for a conventional beamformer with white noise only ($N\alpha_s$) being reduced by the factor $(1-\left|\rho\right|^2)$. This factor accounts for the loss due to pattern distortion in mainlobe jamming. In this condition, as the interference gets close to the pointing direction it is observed that $\left|\rho\right| \approx 1$.

For a uniform linear antenna array, it is a standard problem in array theory to show that [33]

$$\rho = \frac{sin\frac{1}{2}Nkd\theta}{Nsin\frac{1}{2}kd\theta} \simeq 1 - \frac{1}{24}(N^2-1)k^2d^2\theta^2, \tag{9.10}$$

in which the angle $\theta$ is the sine of interference direction relative to broadside, $d$ is the element spacing, and $k = 2\pi/\lambda$ is the wave number. Substituting approximation (9.10) into (9.9) yields [33]

$$SINR_q \simeq \frac{1}{12}N^3\alpha_s k^2d^2\theta^2. \tag{9.11}$$

This expression demonstrates that in the region close to the main beam, the output SINR increases as the square of the angle difference between the interference and the desired signal.

The ideal output SINR obtained in the absence of interference is

$$SINR_{ideal} = N\alpha_s. \tag{9.12}$$

Thus a minimum off-axis angle ($\theta$) for effective interference cancellation can be approximated by setting $SINR_q = SINR_{ideal}$

$$\frac{1}{12}N^3\alpha_s k^2d^2\theta^2 = N\alpha_s, \tag{9.13}$$

and using $k = 2\pi/\lambda$, we can express

$$\theta = \frac{3^{1/2}}{\pi} * \theta_0, \tag{9.14}$$

where it is assumed that $\theta \ll \theta_0$ and $\theta_0 = \frac{\lambda}{Nd}$ is the approximate 3 dB beamwidth of the conventional antenna array, in radians, for $N \gg d$. Note that in this derivation, the jammer power is assumed to be much larger than the signal power. The result approximates the off-axis angle minimum for an untapered beamformer, and the extension to the CMTQ implementation is considered next.

The CMTQ approach was implemented using covariance matrix tapers (CMT) and quiescent pattern control (QPC), and its 3 dB beamwidth is wider than the beamwidth in an untapered beamformer. This beamwidth depends on the amount of tapering in the CMT operation and parameters used in the QPC computation. Recall that the CMT operation requires a *Hadamard* product of the data covariance matrix and a tapering sinc function. Assume that the mainbeam widening effect is due mostly to CMT, we can then approximate this beamwidth by assuming a sinc distribution on the antenna aperture. From [46], the relation between the antenna half-power, untapered beamwidth ($\theta_0$) and the beamwidth obtained with a sinc distribution ($\theta_{0q}$) can be expressed as

$$\theta_{0q} \simeq 1.6\theta_0. \tag{9.15}$$

Therefore, the off-axis angle minimum using the CMTQ approach can be expressed based on (9.14)

$$\theta \simeq \frac{1.6 \times 3^{1/2}}{\pi}\theta_0, \tag{9.16}$$

where $\theta_0 = \frac{\lambda}{Nd}$ (radians) is again the 3 dB beamwidth for a conventional beamformer. This demonstrates a close relationship between the conventional antenna beamwidth and adaptive antenna mainlobe cancellation performance.

### 9.1.2 Numerical Results

Results of Monte Carlo simulations are now presented for both 1-D and 2-D arrays to examine the off-axis angle minimum for effective jamming cancellation. The performance of the new approach is evaluated with the standard MWF (sc) and derivative constraint MWF (der2) approaches. Three simple examples will be considered in which the output SINR loss is computed as a strong jammer is swept through the direction of the desired signal. A simple 1-D array example having 10 elements with a single jammer moving close to the boresight will be examined first. In the second example, the array dimension is expanded to 18 elements. The third example examines a 2-D array with $N = 10$ elements and $M = 10$ pulses in the presence of three jammers.

Figure 9.1 displays the output SINR loss for a simple linear array as a strong jammer is swept through the boresight direction. The example consists of an $N = 10$ element uniform linear array with half-wavelength element spacing. The results compare the sc, der2 and cmtq implementations using a rank of 1 and $2N$ sample support. The desired signal is assumed at the boresight and the signal-to-noise ratio (SNR) is 0 dB. The jammer-to-noise ratio (JNR) is set to 50 dB (element level) above receiver noise. The cmtq method employs a QPC beam with a desired beamwidth of $\Delta\theta = 10°$, a MSE deviation of $\epsilon = .01$, and a penalty function order of $p = 5.5$. It also utilizes a CMT widening factor of $\gamma = 0.01$. As observed, all approaches greatly degrade as the angular distance between the jammer and the target approaches zero. Since the signal steering vector is normalized, the expected SINR loss at the boresight should be approximately equal the value of $[\text{JNR(dB)} + N(\text{dB})]$, which is about 60 dB for this example. It is also observed that away from the boresight, the der2 method has the worst degradation due to its wider mainbeam and the reduced degrees of freedom. The sc performance is slightly better as compared to the cmtq. The off-axis angle minimum ($\theta$) for the cmtq method can be estimated using (9.16) giving $\theta \approx 10°$. This also corresponds to the result shown in Figure 9.1, at which the SINR

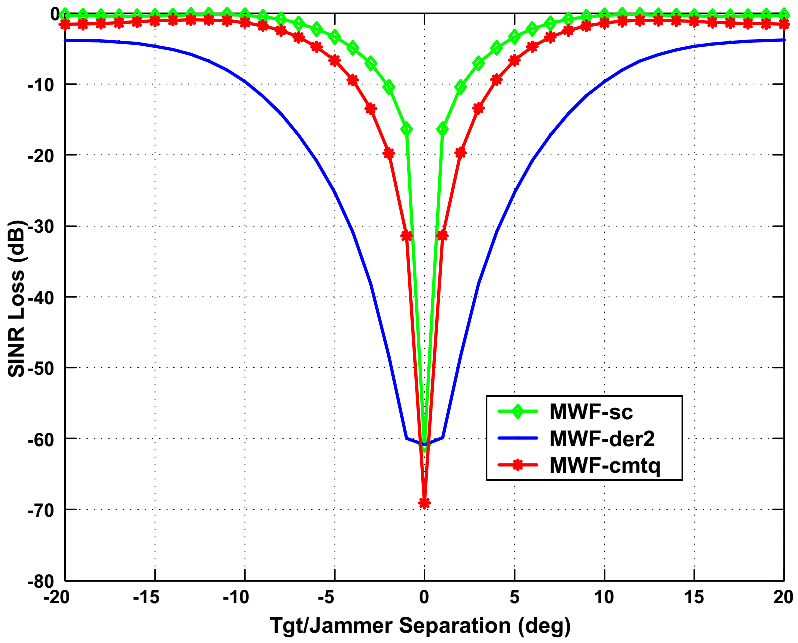

Figure 9.1: Mainbeam Jamming Loss for 1-D Array: SINR loss (dB) vs. separation of target and jammer (degrees); Number of elements, $N = 10$; Samples $= 2N$; Rank $= 1$; Power of jammer/power of target, $\Delta P = 50$ dB

loss becomes negligible.

Next, the same example is examined using a larger linear array having $N = 18$ elements and the results are shown in Figure 9.2. The expected loss at 0° is now equal to [JNR(dB) + $N$(dB)], which is about 62.5 dB for this example. The der2 method again has a poorer performance away from the boresight due to its wider mainbeam and reduced degrees of freedom. For this example, the angle minimum for the cmtq method can be estimated using (9.16) giving $\theta \approx 6°$. This also agrees with the result displayed in Figure 9.1, at which the SINR loss for the cmtq method becomes minimum.

Finally, for completeness in Figure 9.3, a 2-D array is examined with $N = 10$

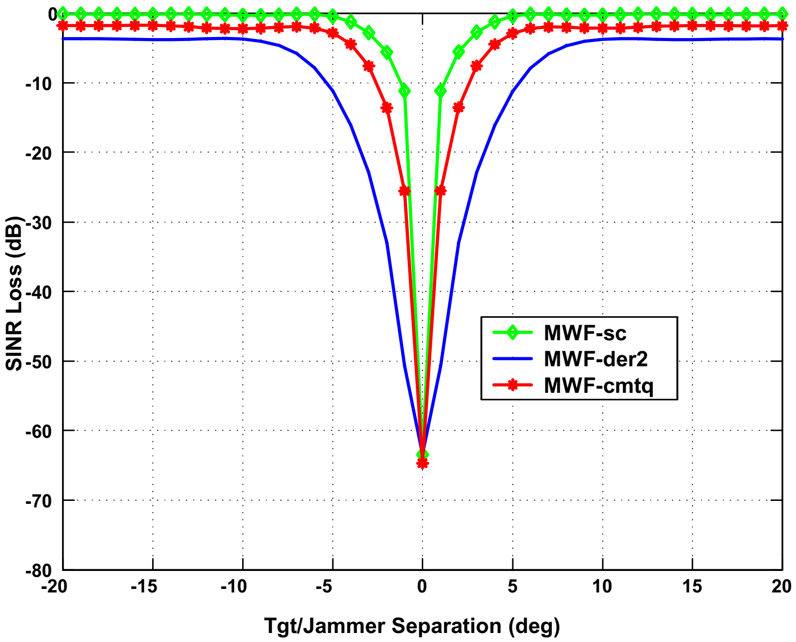

Figure 9.2: Mainbeam Jamming Loss for 1-D Array: SINR loss (dB) vs. separation of target and jammer (degrees); Number of elements, $N = 18$; Samples $= 2N$; Rank $= 1$; Power of jammer/power of target, $\Delta P = 50$ dB

elements and $M = 10$ pulses in the presence of three jammers, using a sample of $2MN$ and a rank of 60. There are two jammers fixed at $-30°$ and $50°$ respectively, while the third jammer is swept from $-20°$ to $20°$. The desired signal is located at the boresight with a normalized Doppler frequency of 0.25 and a signal-to-noise ratio (SNR) is 0 dB. The jammer-to-noise ratio (JNR) is set to 50 dB for each jammer respectively. The expected main beam jamming loss at 0° is equal to [JNR(dB) + $N$(dB)], which is about 60 dB for this example. Both of the sc and der2 methods are shown reducing to this value, while the cmtq method experiences a larger loss of 80 dB. The use of CMT can form a deeper null at jamming directions and therefore results in greater loss when the jammer is right at the boresight. The der2 method

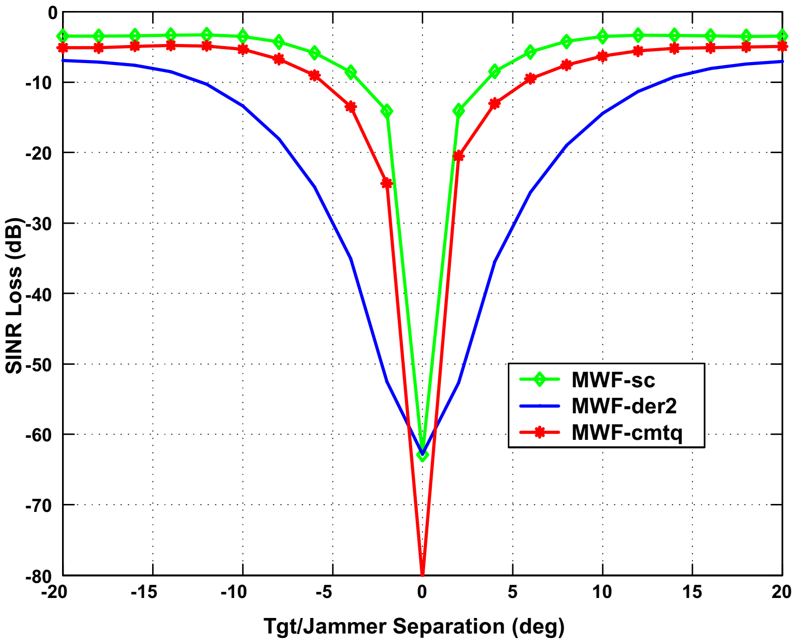

Figure 9.3: Mainbeam Jamming Loss for 2-D Array: SINR loss (dB) vs. separation of target and jammer (degrees); Number of elements, $N = 10$; Number of pulses $M = 10$; Samples $= 2MN$; Rank $= 60$; Power of each jammer/power of target, $\Delta P = 50$ dB; Two jammers are fixed at $-30$ and $50$ degrees while a third jammer is swept from $-20$ to $20$ degrees

again has a poor performance away from the boresight due to its wider mainbeam and reduced degrees of freedom. The off-axis angle minimum for the CMTQ method again can be estimated using (9.16) giving $\theta \approx 10°$, which is also close to the observed value shown in the display.

## 9.2 Computational Requirements

In this section, approximate formulas for the computational savings and memory requirements for the full-rank, MWF single constraint (sc) and MWF CMTQ (cmtq) are compared. These are important criteria to determine the actual complexity of hardware/software implementation and the expected performance of the cmtq approach over the sc and full-rank implementations for real-time operation. Recall for this discussion that $N$ is the number of antenna elements, $M$ is the number of coherent pulses for STAP operation, $L$ is the number of samples, and $K$ is the number of stages in the MWF. The total degrees of freedom $(N_{dof})$ for the 1-D array case is $N$. For the 2-D array used in STAP, $N_{dof}$ is equal to $M * N$.

### 9.2.1 Computational Cost

For the full-rank MVDR, the optimum weight can be found using (2.10) which requires a covariance matrix inverse calculation

$$\mathbf{w}_{mvdr} = \frac{\mathbf{R}^{-1}\mathbf{s}}{\mathbf{s}^H\mathbf{R}^{-1}\mathbf{s}}. \tag{9.17}$$

The beamformer output power at each sample $k$ is expressed as

$$P_{mvdr}(k) = \left|\mathbf{w}_{mvdr}^H \mathbf{x}(k)\right|^2, \tag{9.18}$$

where $\mathbf{x}$ is the array data matrix. To calculate $\mathbf{R}$ for one block of $L$ data would cost $O\left(N_{dof}^2 L\right)$ floating point operations (flop), where $O$ denotes 'on the order of', and each flop is equivalent to a multiplication and an addition. The dominant term in (9.18) is the $N_{dof} \times N_{dof}$ matrix inversion. Note that matrix inversion is typically accomplished by decomposing the covariance matrix into components that are easily invertible. Typically Choleski, LU, or QR decompositions are used and the weights are generally computed by back substitution. Gram-Schmidt (GS), modified GS (MGS), and Householder transformations belong to the well-known class of QR decomposition procedures. Most of these matrix decomposition procedures unfortunately require $O\left(N_{dof}^3\right)$ operations per block or a total of $O\left(N_{dof}^3 L\right)$ operations.

When implementing the standard MWF (sc), the beamformer power output can be efficiently determined from its filter output $e_0(k)$ (4.25)

$$P_{mfw}(k) = \left|e_0(k)\right|^2 . \tag{9.19}$$

The initial stage of the MWF is essentially the conventional beamformer, requiring $N_{dof}$ operations per block of data. Next, the new observed data is computed by multiplying this output with the steering vector and subtracted from the received data, requiring another $N_{dof}$ flops. This is the dominant term in the computation, and for $K$ stages and $L$ snapshots, the cost is $O(2N_{dof}\, KL)$ flops.

The MWF with CMTQ implementations (cmtq) requires an additional constrained quiescent steering vector which does not depend on the data and can be precomputed using a Taylor series approximation as described before. Its computing cost is therefore not directly required for real time operation. In addition, the cmtq approach employs covariance matrix tapers (CMT) which involves a data-domain tapering operation and requires an additional $O\left(N_{dof}\right)$ flops. The total cost for the cmtq method is then $O\left(2N_{dof}LK + N_{dof}L\right)$ flops for real-time operation.

As an example, a typical 2-D STAP system consists of $N = 16$ elements, $M = 14$ pulses and $L = 448$ samples. The environment is assumed homogeneous and the expected rank is $K = 29$ by using Brennan's rule (3.26). The total degrees of freedom is 224. The computational costs associated with the full-rank, sc and cmtq are $503e7$, $5.8e6$ and $5.9e6$ flops respectively. Note that the computation rate of the full-rank is half a teraflop. The cmtq has a reduction in complexity of a factor of 850 over the full-rank and increases in complexity only 1.05 over the sc approach.

In real-world environments, the presence of jamming and eigenvalue spreading requires a rank much larger than 29. If we use a rank of $K = 60$, the computational costs associated with the full-rank, sc and cmtq are $503e7$, $1.20e7$ and $1.21e7$ flops respectively. Thus, the cmtq has a reduction in complexity by a factor of 400 over the full-rank and increases in complexity only 1.008 over the sc method. Now, if we assume at least 3 powerful jammers are present and a rank of $K = 100$ is implemented, the cost associated with the full-rank, sc and cmtq are then $503e7$, $20.1e7$ and $20.2e7$ flops respectively. The cmtq method still has a reduction in complexity by a factor of 25 over the full-rank and increases in complexity only 1.005 over the sc method. This negligible complexity increase of the cmtq approach over the standard MWF approach is certainly outweighed by the performance increase.

### 9.2.2 Performance Gain and Processing Time Trade-offs

This section compares the processing time between the MWF single constraint (sc) and the MWF CMTQ (cmtq) implementations, using a variety of examples for both 1-D and 2-D environments. The performance improvement and computational demands of the cmtq approach will be evaluated with the sc method. The results were evaluated over 100 Monte Carlo trials, which were obtained for various combinations of interference distributions and power levels. Note that the simulations were done in MATLAB, using a Pentium-I processor. These results will generally vary when a different processor is used; however, the relative time delay between the two methods should be consistent. The cmtq method employs a QPC beam with a desired beamwidth of $\Delta\theta = 10^\circ$, a MSE deviation of $\epsilon = .01$, and a penalty function order of $p = 5.5$. It also utilizes a CMT widening factor of $\gamma = 0.01$.

First, Figure 9.4 displays the MWF sample beampatterns for a simple 1-D array in the presence of one strong jammer. The example simulates an $N = 10$ element uniform linear array with half-wavelength element spacing. The results compare the sc and cmtq implementations using a rank of 1 and $2N$ sample support. The desired signal is assumed at the boresight and the jammer is located at $-50°$. The ratio of jammer power to signal power is set to 70 dB. The robustness of the new method is remarkably observed in preserving the mainbeam and reducing sidelobe levels. Its simulation time is just a fraction slower as compared to the standard MWF implementation.

Next, Figures 9.5, 9.6 and 9.7 evaluate the same experiment as the distribution of the jammers was varied. The dotted vertical lines indicate the location of jammers. The robustness of the cmtq response is observed consistently in these results, in which the sidelobe levels are generally much lower as compared to the sc method. Information and parameters employed in each experiment are described in Table 9.1, which also lists the processing time for a more complete variety of jammer distributions. Note that in these simulations, a sample support of $2N$ was employed and the MWF rank was equal to the number of jammers. As the number of jammers or the number of elements ($N$) is larger, the simulation time also increases as we expected. The relative delay time between the two methods is very consistent in which the additional processing time due to the cmtq approach for these different examples is approximately less than 10% of the time required by the sc method. This negligible delay increase is certainly outweighed by its performance improvement.

A 2-D array example is now employed in which $N = 10$ elements and $M = 10$

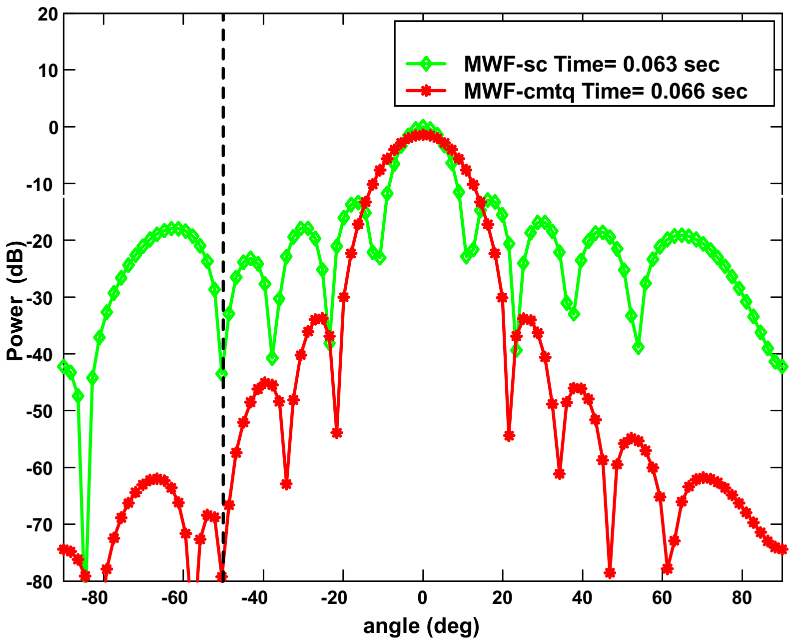

Figure 9.4: MWF Sample Beampatterns: Received power (dB) vs. azimuth angle (deg); Number of elements, $N = 10$; Number of samples, $N_s = 2N$; Rank of MWF, $k = 1$; Jammer is at $-50°$; Jammer over signal power ratio, $\Delta P = 70$ dB

| **Jammer Distribution (N = 10 elements)** | **sc** | **cmtq** |
|---|---|---|
| 1 jammer $(-50°, 70\text{ dB})$ | .063 | .066 |
| 2 jammers $(-30°, 30°)$ (50 dB each) | .087 | .096 |
| 2 jammers $(-30°, 30\text{dB}), (30°, 60\text{ dB})$ | .084 | .088 |
| 3 jammers $(-30°, 30°, 50°)$ (50 dB each) | .092 | .092 |
| 3 jammers $(-30°, 30\text{ dB}), (30°, 40\text{ dB}), (50°, 60\text{ dB})$ | .093 | .096 |
| 6 jammers $(-40°, -30°, -20°, 30°, 50°, 60°)$ (40 dB each) | .095 | .101 |
| | | |
| **Jammer Distribution (N = 100 elements)** | | |
| 6 jammers $(-40°, -30°, -20°, 30°, 50°, 60°)$ (40 dB each) | 4.5 | 4.6 |

Table 9.1: Time Processing for 1-D Array Examples (Different jammer distributions were used; Rank = number of jammers; Number of samples = 2N; sc = MWF - single constraint; cmtq = MWF - cmtq; Processing time is displayed in seconds )

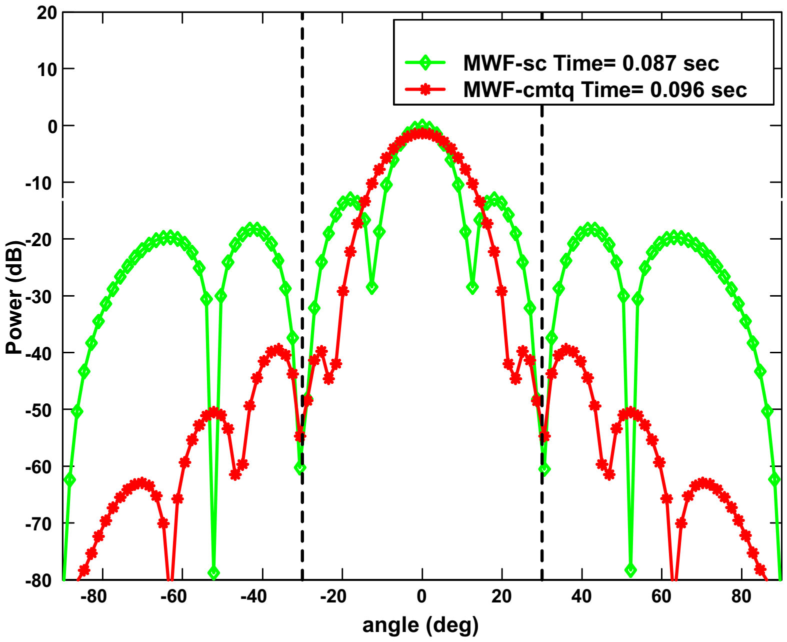

Figure 9.5: MWF Sample Beampatterns: Received power (dB) vs. azimuth angle (deg); Number of elements, $N = 10$; Number of samples, $N_s = 2N$; Rank of MWF, $k = 2$; Two jammer are at $-30°$ and $30°$; Jammer over signal power ratio, $\Delta P = 50$ dB

pulses, and the MWF spatial beampatterns are shown in Figure 9.8. The clutter-to-noise (CNR) ratio is 40 dB per element per pulse with the clutter foldover factor of $\beta = 1$. The desired signal is located at the boresight with a normalized Doppler frequency of 0.25 and a signal-to-noise ratio (SNR) of 0 dB. The number of samples is $N_s = 2MN$ and the rank of the MWF is $K = 19$. The robustness of the cmtq beamformer is well observed with much lower sidelobe levels while its processing time is delayed just within a fraction from the sc method.

Next, the same environment is evaluated in Figure 9.9 with the presence of three additional jammers. These jammers are located at $-35°$, $30°$ and $50°$ and their respective jammer-to-noise ratios ($JNR$) are 40 dB, 30 dB and 50 dB respectively.

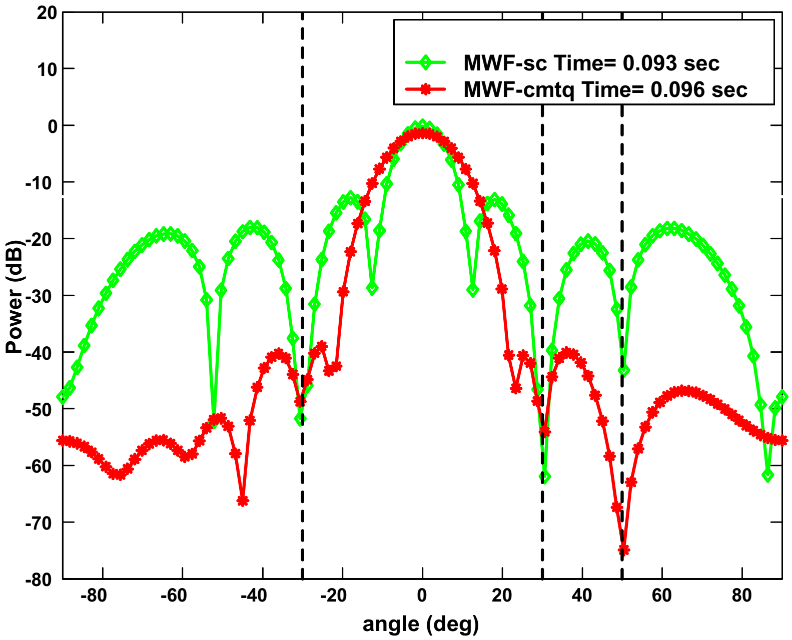

Figure 9.6: MWF Sample Beampatterns: Received power (dB) vs. azimuth angle (deg); Number of elements, $N = 10$; Number of samples, $N_s = 2N$; Rank of MWF, $k = 3$; Three jammers are at $-30°$, $30°$ and $50°$; Jammer over signal power ratios, $\Delta P = 30$, 40, and 60 dB

Note that a higher rank of 50 is now required since the presence of the jammers increases the effective rank of the data. As a result, the processing time is also seen much longer as compared to the case with no jammers. The cmtq method is evidently more robust with reduced sidelobe levels and markedly widened nulls at all jamming directions. The relative time delay required by the cmtq method is still less than 10% of the time needed by the sc method.

The effects of both jamming and eigenvalue spreading are now considered in Figure 9.10. The jammers are located at $-35°$ and $30°$ with the jammer-to-noise ratios ($JNR$) are 40 dB and 30 dB respectively. The eigenvalue spreading is simulated

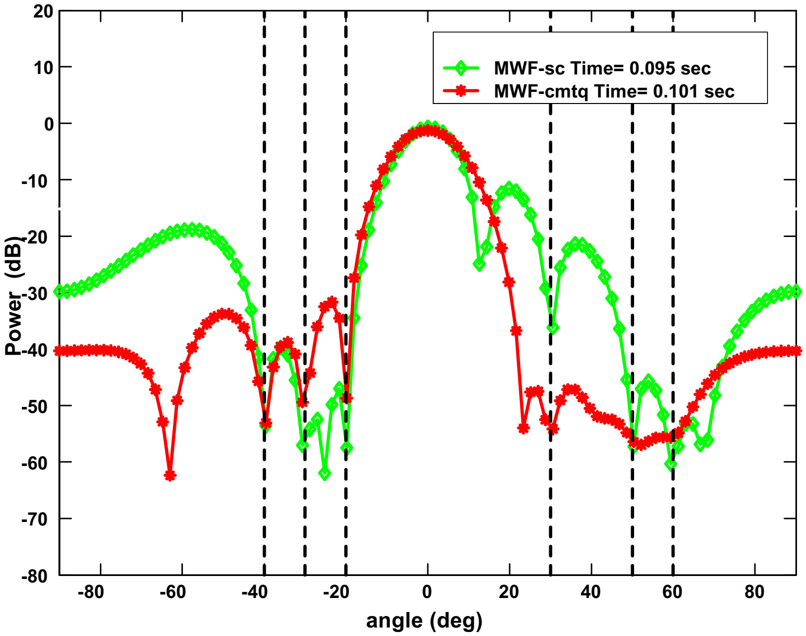

Figure 9.7: MWF Sample Beampatterns: Received power (dB) vs. azimuth angle (deg); Number of elements, $N = 10$; Number of samples, $N_s = 2N$; Rank of MWF, $k = 6$; Six jammers are at $-40°$, $-30°$, $-20°$, $30°$, $50°$ and $60°$; Jammer over signal power ratio, $\Delta P = 40$ dB

with an intrinsic clutter motion (ICM) of $\sigma_v = 1$ m/s. The cmtq response is again more robust with reduced sidelobe levels and widened nulls at all jamming directions. The same trend is also observed as before in which the additional delay time of the cmtq method is very insignificant as compared to the sc method.

Table 9.2 lists the processing time for the sc and cmtq methods in which a more complete variety of jammer and ICM distribution was evaluated. In these simulations, a sample support of $2MN$ was implemented. As the number of jammers is increased and the ICM is added, a higher rank is required and the simulation time also increases as we expected. The relative delay between the two methods is also

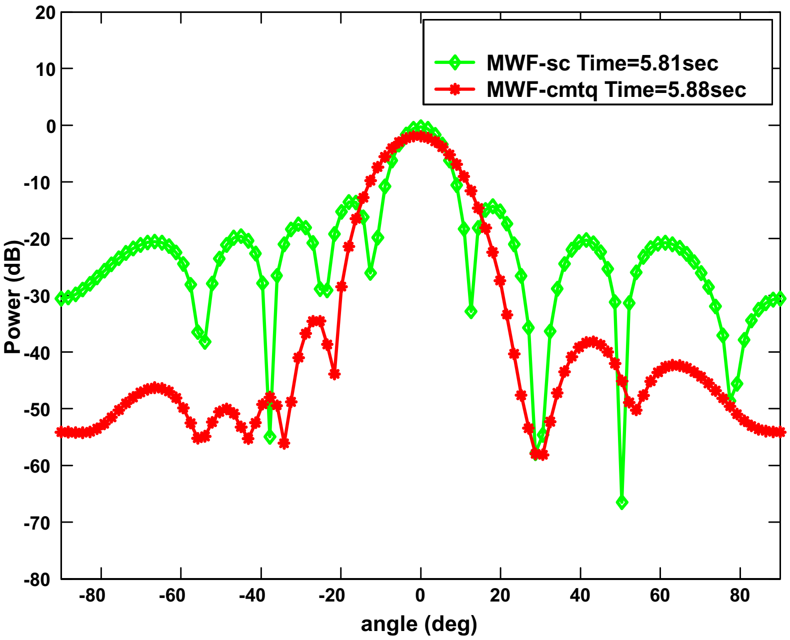

Figure 9.8: MWF Sample Beampatterns: Received power (dB) vs. azimuth angle (deg); Number of elements, $N = 10$; Number of pulses, $M = 10$ pulses; Number of samples, $N_s = 2MN$; Rank of MWF, $k = 19$

very consistent in which the additional delay required by the cmtq approach for these different cases is approximately within 10% of the time due to the sc method.

### 9.2.3 Memory Requirements

The memory requirement for the MWF approach in the initial stage is simply a buffer of size $N_{dof}$ needed to store the steering vector. Each additional stage requires storage space for the cross-correlation vector $\mathbf{h}_i$ for $i = 1..K$. Each of these vectors has a length of $N_{dof}$ and a total of $(K+1)N_{dof}$ storage elements are needed. This requirement does not depend on the sample size since the storage space can be overwritten for each block of data. The cmtq approach requires an additional storage space of

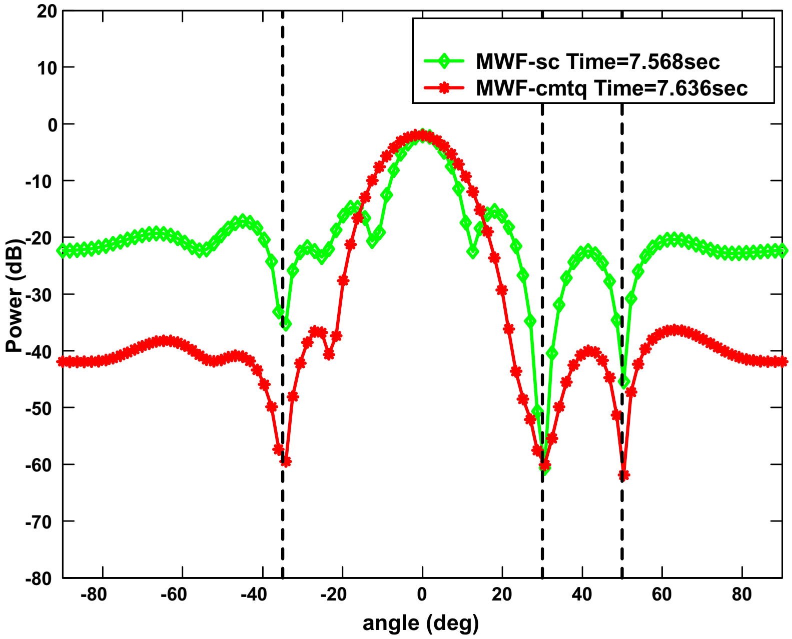

Figure 9.9: MWF Sample Beampatterns: Received power (dB) vs. azimuth angle (deg); Number of elements, $N = 10$; Number of pulses, $M = 10$ pulses; Number of samples, $N_s = 2MN$; Rank of MWF, $k = 50$; Three jammers are at $-35°, 30°$,and $50°$; Jammer over signal power ratios are at $40, 30$,and 50 dB

$N_{dof}^2$ for the $N_{dof}\times N_{dof}$ CMT taper matrix, which increases the memory requirement to $(K+1)N_{dof} + N_{dof}^2$ storage elements. Next, for the full-rank technique, a total of $2N_{dof}^2 + N_{dof}$ storage elements are required to store the $N_{dof} \times N_{dof}$ covariance matrix, its inverse, and the dimensional $N_{dof}$ steering vector.

Using the same example as above with $N = 16$ elements, $M = 14$ pulses, a rank of $K = 60$ and $L = 448$ snapshots, the memory requirement associated with the full-rank, sc method, and cmtq methods are $10.1e4$, $1.4e4$ and $6.4e4$ respectively. The storage requirement of the cmtq approach is 4 times greater than the sc method; however, it is still 40% less than the full-rank approach. The storage space for

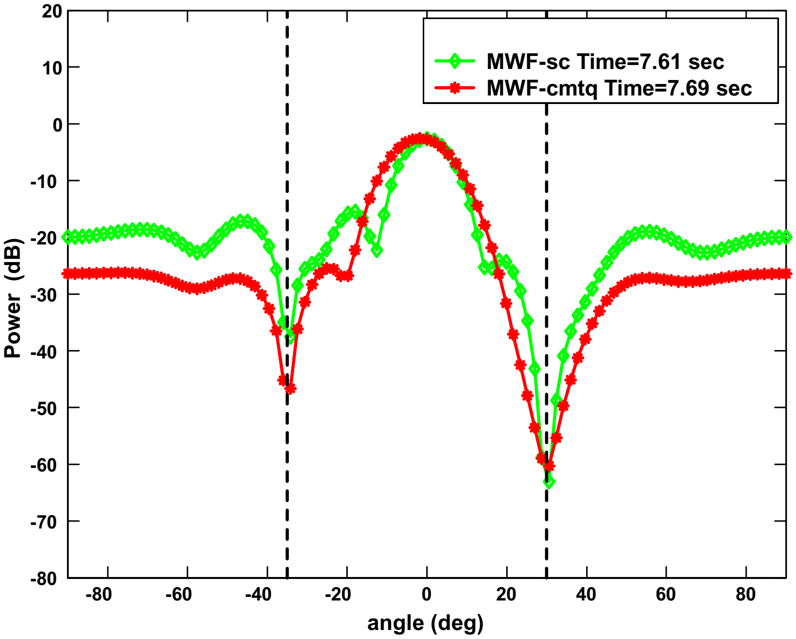

Figure 9.10: MWF Sample Beampatterns: Received power (dB) vs. azimuth angle (deg); Number of elements, $N = 10$; Number of pulses, $M = 10$ pulses; Number of samples, $N_s = 2MN$; Rank of MWF, $k = 50$; Two jammers are at $-35°$ and $30°$; Jammer over signal power ratios are at 40 and 30 dB; ICM, $\sigma_v = 1$ m/s

the cmtq method can be more likely accommodated on the desired implementation hardware as compared to full-rank approaches. These equations on the computational cost and memory requirements are summarized in Table 9.3.

| **Jammer Distributions** | $\sigma$ | **k** | **sc** | **cmtq** |
|---|---|---|---|---|
| 0 jammer | 0 | 19 | 5.81 | 5.88 |
| 0 jammer | 1 | 50 | 7.52 | 7.58 |
| 1 jammer ($-50°$,50 dB) | 0 | 42 | 6.99 | 7.05 |
| 1 jammer ($-50°$,50 dB) | 1 | 50 | 7.29 | 7.34 |
| 2 jammers ($-35°, 40$ dB), ($30°$,30 dB) | 0 | 50 | 7.61 | 7.68 |
| 2 jammers($-35°, 40$ dB), ($30°$,30 dB) | 1 | 50 | 7.61 | 7.69 |
| 3 jammers ($-35°, 40$ dB), ($30°, 30$ dB), ($50°$,50 dB) | 0 | 50 | 7.57 | 7.64 |
| 3 jammers ($-35°, 40$ dB), ($30°, 30$ dB), ($50°$,50 dB) | 1 | 63 | 7.63 | 7.70 |

Table 9.2: Time Processing for 2-D Array Examples (Different jammer distributions were used; sc = MWF - single constraint; cmtq = MWF - cmtq; Processing time is displayed in seconds; Sigma = Intrinsic clutter velocity (m/s); k = number of ranks; N = 10 elements; M = 10 pulses; Number of samples = 2MN )

| | **Computational Cost** | **Memory Requirements** |
|---|---|---|
| **Full-rank** | $N_{dof}^3 L$ | $2N_{dof}^2 + N_{dof}$ |
| **MWF single constraint (sc)** | $2N_{dof}LK$ | $(K+1)N_{dof}$ |
| **MWF-CMTQ (cmtq)** | $N_{dof}L(2K+1)$ | $(K+1)N_{dof} + N_{dof}^2$ |

Table 9.3: Computational Cost and Memory Requirements (Compare full-rank, MWF-single constraint, and MWF-cmtq implementations)

# Chapter 10

# Conclusions

In this dissertation, a robust steering vector mismatch technique for the reduced-rank multistage Wiener filter (MWF) was presented for the application of airborne radar space-time adaptive processing (STAP). Reduced rank signal processing is motivated by future requirements of target detection in the presence of intense ground clutter and interference in nonhomogeneous environments with limited sample support. In these environments, calibration errors and steering vector mismatch can further degrade adaptive array performance and result in signal cancellation. Since the MWF centrally employs the steering vector in its formulation, it is important to assess the impact of steering vector mismatch. The new approach exploits a combination of covariance matrix tapers (CMT) and quiescent pattern control (QPC) in the MWF structure, denoted CMTQ, which is very effective at mitigating steering vector mismatch errors. The goal is to broaden the acceptance angle while preserving the MWF's ability to adapt to finite sample support and reject interference from directions outside this acceptance angle. Use of CMTQ augmentation provides the steering vector mismatch robustness that we desire while improving reduced rank and sample support characteristics of the MWF. This is critical for adaptation in nonhomogeneous environments where sample support is limited and steering vector mismatch may be a problem.

The MWF is a reduced-rank minimum variance technique that offers the possibility of achieving or surpassing the same high performance as the full-rank MVDR, while minimizing the sample support and computational burden. The MWF was shown in this dissertation to provide many advantages to previously developed reduced rank algorithms such as principal components (PC) and the cross spectral metric (CSP). One major benefit is due to its significant subspace suppression, thereby greatly reducing sample support and computational complexity. It also does not depend on eigen-based decomposition, which is computational intensive and does not require calculation and inversion of the traditional data covariance matrix, as required by existing beamforming approaches. The convergence region of the MWF as a function of both rank and sample support was demonstrated to be more robust with significant SINR improvement as compared to the results obtained using principal components (PC) methods, particularly in the presence of eigenvalue spreading. Nevertheless, the impact of steering vector mismatch can still seriously degrade the MWF performance especially when the signal is included in the training data.

The proposed CMTQ implementation exploits CMT [30] and QPC [56], both of which are robust for adaptive pattern control in limited sample support. CMT can be realized by the application of a conformal matrix taper to the original sample data. An efficient application of CMT in the MWF data structure was presented and it is based on the subspace spanned by the principal eigenvectors of the CMT matrix. This tapering process naturally widens the mainbeam, but it also adds robustness by broadening the null in the direction of clutter and interference. The use of CMT may increase the effective rank of the covariance matrix it is modifying, therefore requiring a higher rank in the MWF structure. These shortcomings can be improved with quiescent pattern control. QPC employs a constrained quiescent pattern in the MWF structure and is based on a mean square error between the array response and a desired response over a given angular region. This helps preserve a desired mainlobe width while producing a highly adaptive pattern in white noise environments, and therefore the beamformer also adapts well even before its response has adapted to a colored noise environment. An efficient QPC implementation was also presented exploiting the Taylor series approximation to estimate the solution at a significant reduction in computed operations. While minimizing additional complexity for real-time processing, QPC helps preserve and improve the beamformer response at a reduced rank in a nonhomogeneous environment with limited sample support.

Results using Monte Carlo realizations were examined to evaluate the robustness of the new approach with the standard MWF and full rank approaches. Additionally, a new MWF implementation using the well-known derivative constraints was introduced as a baseline comparison to the proposed approach. Derivative constraints methods suffer many major drawbacks and limit the adaptive degrees of freedom available. Numerical results in both 1-D spatial-only and 2-D STAP applications have demonstrated that the new approach outperforms the standard MWF, derivative-constrained MWF, and full-rank methods under steering vector errors. The 1-D example was realized with the target contaminated in all samples of the training data. The STAP example was modeled with the target confined to a data snapshot and with the presence of intrinsic clutter motion (ICM), which are typical for severely nonhomogeneous radar environments. The vast improvement of the new approach in terms of SINR loss as a function of both rank and sample performance were observed under steering vector errors, and this could add significant robustness to reduced rank approaches and STAP applications.

Finally, the new approach was evaluated using experimental MCARM data. The performance was first examined using $1N_{dof}$ sample support and provided similar SINR performance as compared with the standard MWF without steering vector errors. As steering vector mismatch is present, the improvement in performance was clearly demonstrated both in terms of rank and sample performance as compared to the standard MWF, derivative constraint MWF and full rank methods. In addition, the robustness of the new approach was demonstrated using CFAR test statistics for radar target detection in which the STAP output power for each range sample is normalized with respect to the noise power. In practice, the STAP processor is restrained for each range cell such that the range cell under observation and some guard cells are excluded from the data set in order to form a signal free training data set. This process requires more samples to be utilized for the guard cells and also adds considerable computational complexity. The new approach has demonstrated a superior CFAR performance even when the target is present in the training data, providing robustness for real-world STAP applications

A future research topic related to the work presented here is application of the cmtq approach to sonar environments where steering vector mismatch is the dominant cause for signal suppression and can arise from beam steering angle errors, phase errors in the beamformer and multipath propagation. The performance improvement of the MWF was published for sonar applications [53]. In this dissertation, the robustness of the new approach was demonstrated using Monte Carlo simulations in 1-D passive array applications in which the signal is present in all snapshots of the data and is typical for sonar environments. The new approach can therefore be extended to sonar environments and applied to the large number of sonar data bases presently available.

The use of CMTQ constraints can also be applied to a nonlinear array geometry. STAP has been traditionally applied to uniform linear arrays (ULA), which do not provide 360° azimuth coverage unless they are mechanically steered and controlled by a complex, expensive, rotary joint. The Navy's UHF Electronically Scanned Array (UESA) is under development as an upgrade to current mechanically scanned system of the linear arrays. STAP employed in a UESA architecture however creates the so-called "angle-Doppler mismatch" that gives rise to both an increase in clutter rank and a greater degree of statistical nonstationarities. with range, relative to a uniform linear array (ULA) [68]. The first problem is due to the presence of eigenvalue spreading in a UESA, which requires more adaptive degrees of freedom (DOF) to cancel the clutter. The second problem exists because the clutter Doppler frequency with an azimuth and elevation angle observed in a circular array varies with range, and the performance is expected to degrade under steering vector errors. The MWF has been shown to provide a robust reduced-rank solution in a ULA in the presence of eigenvalue spreading and limited sample support. The use of CMTQ constraints in the MWF structure offers potential advantages and robustness to these problems.

Finally, the new approach has been demonstrated to provide robust adaptive patterns with low sidelobe levels. The performance achieved however could not be controlled by some prescribed parameters. Future areas for investigation can be focused on the design of new CMT's and QPC's that minimize the SINR loss for given prescribed adapted pattern constraint parameters such as sidelobe levels and desired beamwidth.

# Bibliography

[1] Applebaum, S. P. and Chapman, D.J., “An adaptive array with mainbeam constraints”, *IEEE Transactions on Antennas and Propagation,* Vol. 24, pp. 650-662, 1976.

[2] Andrews, G. A., “A detection philosophy for AMTI radar”, *IEEE International Radar Conference,* pp. 111-116, 1975.

[3] Babu, B.N.S.; Torres, J.A.; and Melvin, W.L., “Processing and evaluation of multichannel airborne radar measurements (MCARM) measured data ”, *IEEE International Symposium on Phased Array Systems and Technology*, pp. 395-399, 1996.

[4] Barile, E.; Fante, R. and Torres, J., “Some limitations on the effectiveness of airborne adaptive radar”, *IEEE Transaction on Aerospace and Electronic Systems*, Vol. 28, No. 4, pp. 1015-1032, 1992.

[5] Buckley, K.M. and Griffiths, L.J., “An adaptive generalized sidelobe canceller with derivative constraints”, *IEEE Transactions on Antennas and Propagation,* Vol. 34, pp. 311–319, 1986.

[6] Bell, K.L. and Van Trees, H.L., “Adaptive and non-adaptive beampattern control using quadratic beampattern constraints”, *Proceedings of the 33rd Asilomar Conference on Signals, Systems, and Computers,* Vol. 1, pp. 486-490, 1999.

[7] Brennan, L E. and Reed, I. S., "Theory of adaptive radar", *IEEE Transactions on Aerospace and Electronic Systems,* Vol. 9, pp. 237-251, 1973.

[8] Brennan, L E. and Staudaher, F. M., "Subclutter visibility demonstration", *Technical Report RL-TR-92-21,* Adaptive Sensors Incorporated 1992.

[9] Carlson, R.T. Jr., "Covariance matrix estimation errors and diagonal loading in adaptive arrays", *IEEE Transactions on Aerospace and Electronic Systems*, Vol. 24, pp. 397-401, 1988.

[10] Compton, R. T. Jr., *Concepts and Performance,* Englewood Cliffs, Prentice Hall, 1980.

[11] Compton, R.T. Jr., "The effect of random steering vector errors in the Applebaum adaptive array", *IEEE Transactions on Aerospace and Electronic Systems*, Vol. 18, pp. 392-400, 1982.

[12] Chen, W. and Reed, I. S., "A new CFAR detection test for radar", *Digital Signal Processing 1*, pp. 198-214, 1991.

[13] Cox, H., "Resolving power and sensitivity to mismatch of optimum array processors", *Journal Acoustics Soc. Amer.*, Vol. 54, No. 3, pp. 771-785, 1973.

[14] Cox, H.; Zeskind, R. and Owen, M., "Robust adaptive beamforming," *Transactions in Acoustics, Speech, and Signal Processing*, Vol. 35, No. 10, pp. 1365-1376, 1987.

[15] Er, M.H. and Catoni, A., "Derivative constraints for broad-band element space antenna array processor", *IEEE Transactions on acoustics, speech, and signal processing*, Vol. 31, pp. 1378-1393, 1983.

[16] Er, M. H. and Cantoni, A., "A new approach to the design of robust narrowband array processors", *Proceedings of the IEEE International Conference on Acoustics Speech and Signal Processing,* pp. 2527-2530, 1986.

[17] Er, M.H. and Cantoni, A., "An alternative formulation for an optimum beamformer with robustness capability", *IEE Proceedings*, Vol. 132, Pt. F, No. 6, pp. 447-460, 1985.

[18] Er, M.H., "Adaptive antenna array under directional and spatial derivative constraints", *IEE Proceedings*, Vol. 135, Pt. H, No. 6, pp. 414-419.

[19] Er, M.H. and Ng, B.C., "On derivative constrained broad-band beamforming", *IEEE Transactions on Aerospace and Electronic Systems*, Vol. 38, pp. 551-552, 1990.

[20] Er, M.H. and Ng, B.C., "A new approach to robust beamforming in the presence of steering vector errors", *IEEE Transactions on Signal Processing*, Vol. 42, No. 7, pp. 1826-1829, 1994.

[21] Fieldman, D.D. and Griffiths, L.J., "A projection approach for robust adaptive beamforming", *IEEE Transactions on Signal Processing*, Vol. 42, No. 4, pp. 853–863, 1994.

[22] Gabriel, W. F., "Spectral analysis and adaptive array superresolution techniques", *Proceedings IEEE*, Vol. 68, No. 6, pp. 654–666, 1980.

[23] Goldstein, J.S.; Guerci, J.R. and Reed, I.S., *Intelligent Signal Processing,* Chapter 12: Reduced-Rank Intelligent Signal Processing with Application to Radar, S. Haykin and B. Kosko, New York, 2001.

[24] Goldstein, J. S.; Reed, I.S. and Zulch, P.A., "Multistage partially adaptive STAP CFAR detection algorithm", *IEEE Transactions on Aerospace and Electronic Systems*, Vol. 35, No. 2, pp. 645-662, 1999.

[25] Goldstein, J.S.; Reed, I.S. and Scharf, L.L., "A multistage representation of the Wiener filter based on orthogonal projections", *IEEE Transactions on Information Theory*, Vol. 44, No. 7, pp. 2943-2959, 1998.

[26] Goldstein, J.S. and Reed, I.S., “Reduced rank adaptive filtering”, *IEEE Transactions on Signal Processing*, Vol. 45, No. 2, pp. 492–496, 1997.

[27] Goldstein, J.S.; Reed, I.S. and Tague, J., “A low complexity implementation of adaptive Wiener filters”, *Proceedings of the 31st Asilomar Conference on Signals, Systems, and Computers*, Vol. 1, pp. 770-774, 1997.

[28] Guerci, J. R. and Bergin, J. S., “Principal components, covariance matrix tapers, and the subspace leakage problem”, *IEEE Transactions on Aerospace and Electronic Systems*, Vol. 38, No. 1, pp. 152-162, 2002.

[29] Guerci, J.R. and S. U. Pillai, “Application of the Khatri-Rao Product to Statistical Signal Processing”, *Proceedings of the International Conference in Honor of Professor C. R. Rao on the Occasion of his 80th Birthday*, San Antonia, TX, Mar. 2000.

[30] Guerci, J.R., “Theory and application of covariance matrix tapers for robust adaptive beamforming”, *IEEE Transactions on Signal Processing*, Vol. 47, No. 4, pp. 977–985, 1999.

[31] Guerci, J.R.; Goldstein, J.S; Reed, I.S.; Nguyen, H., and Bergin, J.S., “Optimal reduced rank STAP for circular adaptive arrays”, *Proceedings of the Space-Time Processing Methods for Circular Ring Arrays with Application to Navy Airborne Surveillance Radar*, George Mason University, Fairfax, VA, Feb. 1999.

[32] Haystead, J., “JSTARS-real-time warning and control for surface warfare”, *Defense Electronics*, pp. 31-39, 1990.

[33] Hudson, J. E., *Adaptive Array Principles*, IEE Press, London, UK, 1981.

[34] Haimovich, A.M.; Pugh, M.L and Berin, M.O., “Training and signal cancellation in adaptive radar”, *Proceedings of IEEE National Radar Conference*, pp. 124–128, 1996.

[35] Haimovich, A.M., “The eigencanceller: adaptive radar by eigen-analysis methods”, *IEEE Transactions on Aerospace and Electronic Systems*, Vol. 32, pp. 532-542, 1996.

[36] Hiemstra, J.; Wiepert, M.; Nguyen, H. and Goldstein, J.S., “Injection of diagonal loading into the multistage Wiener filter”, *IEEE Sensor Array and Multichannel Signal Processing Workshop,* Arlington, Va, August 2002.

[37] Horn, R. A., *Topics in Matrix Analysis*, Cambride University Press, Newyork, 1991.

[38] Huang, K.C. and Yeh, C.C., “Performance analysis of derivative constraint adaptive arrays with pointing errors”, *IEEE Transactions on Antennas and Propagation*, Vol. 40, No. 8, pp. 975-981, 1992.

[39] Hughes, D.T., “Penalty function method for sidelobe control in least squares adaptive beamforming”, *Proceedings of SPIE*, pp. 170–181, 1995.

[40] Jablon, N.K., “Adaptive beamforming with the generalized sidelobe canceller in the presence of array imperfections”, *IEEE Transactions on Antennas and Propagation*, Vol. 34, pp. 996-1012, 1986.

[41] Jablon, N.K., “Effect of element errors on half-power beamwidth of the Capon adaptive beamformer”, *IEEE Transactions on Circuits and Systems*, Vol. 34, No 7, pp. 743-752, 1987.

[42] Mahafza, B. R., *Radar Systems Analysis and Design Using Matlab,* Chapman & Hall/CRC, 2000.

[43] Klemm, R., *Space-Time Adaptive Processing: Principles and Applications*, IEE Press, London, UK, 1998.

[44] Lee, F. W., and Staudaher, F., "NRL adaptive array flight test data base", *Proceedings IEEE Adaptive Antenna Systems Symposium,* pp. 101-104, 1992.

[45] Mailloux, R.J., "Covariance matrix augmentation to produce adaptive array pattern troughs", *Electronic Letters,* Vol. 31, No. 10, pp. 771-772, 1995.

[46] Mailloux, R.J., *Phase Array Antenna Handbook*, Artech House, Table 1.1, Norwood, MA, 1994.

[47] Monzingo, R. A. and Miller, T.W., *Introduction to Adaptive Arrays, John Wiley and Sons,* 1980.

[48] Nguyen, H.; Hiemstra, J.; Goldstein, J.S.; Pratt, T. and Allnutt, J., "A robust steering vector mismatch technique for the multistage Wiener filter", *IEEE Sensor Array and Multichannel Signal Processing Workshop*, Arlington, Va, August 2002.

[49] Ogle, W.; Nguyen, H.; Goldstein, J.S.; Zulch, P.A.; and Wicks, M., "Nonhomogenity detection and the multistage Wiener filter", *Proceedings of IEEE Radar Conference*, Long Beach, CA, Apr. 2002.

[50] Picciolo, M. ; Nguyen, H. and Andrew, G. A., "An investigation of space-time adaptive processing with regard to minimum detectable velocity", *Naval Research Laboratory Technical Report*, NRL/MR/5315–99-8383, pp. 1-23, June 1999.

[51] Rao, C.R. and Rao, M.S., *Matrix Algebra and Its Applications to Statistics and Econometrics,* World Scientific Publishing, Section 6, 216, Aug., 2000.

[52] Reed, I.S; Mallet, J.D., and Brennan, L.E., "Rapid convergence rates in adaptive arrays", *IEEE Transactions on Aerospace and Electronic Systems*, Vol. 10, No. 6, pp. 853–863, 1994.

[53] Ricks, D.C, "Efficient architectures for implementing adaptive algorithms", *Proceedings of the 2000 Antenna Applications Symposium,* pp. 29–41, 2000.

[54] Robey, F.C; Fuhrman, D. R.; Kelly, E.J. and Nitzberg, R., "A CFAR adaptive matched filter detector", *IEEE Tran. Aerosp. Electron. Syst.,* Vol. 28, No. 1, pp. 208–216, 1992.

[55] Steele, A.K, "Comparison of directional and derivative constraints for beamformer subject to multiple linear constraint", *Proceedings F, Communications, Radar Signal Processing,* Vol. 34, pp. 1378–1393, 1983.

[56] Sim, S.L. and Er., M.H., "An effective quiescent pattern control strategy for GSC structure", *IEEE Signal Processing Letters,* Vol. 3, No. 8, pp. 236-238, 1996.

[57] Sim, S.L. and Er., M.H., "Constrained optimization technique for general pattern synthesis", *Electronics Letters,* Vol. 32, No. 10, pp. 861-862, 1996.

[58] Skolnik, M., *Radar Handbook,* McGraw-Hill, 1990.

[59] Sloper, D.; Fenner, D.; Arntz, J.; and Fogle, F., "Multi-channel airborne radar measurement (MCARM), MCARM flight test", *Tech. Rep. RL-TR-96-49,* USAF Rome Laboratory, April. 1996.

[60] Tian, Z.; Bell, K.L. and Van Trees, H.L., "A recursive least squares implementation for adaptive beamforming under quadratic constraint", *Proceedings 9th IEEE Workshop Stat. Signal Array Process.,* pp. 9-12, Sept. 1998.

[61] Titi, G. W. and Marshall, D.F., "The ARPA/NAVY Mountaintop Program: adaptive signal processing for airborne early warning radar", *Proceedings of the IEEE International Conference on Acoustics Speech and Signal Processing,* Vol. 2, pp. 1165-1168, 1996.

[62] Tseng, C.Y., "Minimum variance beamforming with phase-independent derivative constraints", *IEEE Transactions on Antennas and Propagation*, Vol. 40, No. 3, pp. 285-294, 1992.

[63] Veen, B.V., "Eigenstructure based partially adaptive array design", *IEEE Transaction on Antennas and Propagation*, Vol. 36, pp. 357-362, 1988.

[64] Veen, B. V., "Minimum variance beamforming with soft response control constraints", *IEEE Transactions on Signal Processing*, Vol. 39, No. 9, pp. 1964-1972, 1991.

[65] Tufts, D.; Kirsteins, I. and Kumaresan, R., "Data-adaptive signal estimation by singular value decomposition of a data matrix", *Proceedings IEEE*, Vol. 70, No. 6, pp. 684-685, 1982.

[66] Zatman, M., "Production of adaptive array troughs by dispersion synthesis", *Electronics Letters*, Vol. 31, No. 25, pp. 2141-2142, 1995.

[67] Zatman, M. and Guerci., J.R., Comments and Reply to " Theory and Application of Covariance Matrix Tapers for Robust Adaptive Beamforming", *IEEE Transactions on Signal Processing,* Vol. 48, No. 6, pp. 1796-1800, 2000.

[68] Zatman, M., " Circular Array STAP", *Proceedings of IEEE Radar Conference* , pp. 108-113, 1999.

[69] Ward, J., "Space-Time Adaptive Processing for Airborne Radar", *Lincoln Laboratory Technical Report 1015*, 1994.

[70] Wu, R., "Array pattern distortion and remedies in space-time adaptive adaptive processing for airborne radar", *IEEE Transaction on Antennas and Propagation*, Vol. 46, pp. 963-970, 1998.

# Vita

Hien Nguyen was born in Saigon, Vietnam, on November 6, 1964. He has been a senior staff member of the Adaptive Signal Exploitation Branch of Science Applications International Corporation (SAIC) since August 1998. His work has focused on the research of adaptive signal processing algorithms for airborne radar and synthetic aperture radar. Prior to working at SAIC, he worked at the Naval Research Laboratory as an electronics engineer for two years in the development of space-time adaptive signal processing algorithms for airborne radar systems. He also worked at the Naval Undersea Warfare Center (NUWC) for nearly ten years in the development of test software for Automatic Test Equipment. He received the B.S. degree in electrical engineering from Old Dominion University at Norfolk, Virginia in 1987 and the M.S. degree in electrical engineering from Virginia Tech in 1992, graduating from both with high honors. He is a member of the Tau Beta Pi and Eta Kappa Nu honor societies. His research interests include antenna array signal processing, synthetic aperture radar, radar system design and communications.